Novel pulsed optical parametric sources in the mid-infrared and the application towards high-resolution molecular spectroscopy

Hanyu Ye

Universitat Politècnica de Catalunya

Barcelona, March 2019

Doctorate Program: **Photonics**

Duration: **2016-2019**

Thesis Advisor: **Prof. Majid Ebrahim-Zadeh**
Thesis Co-Advisor: **Dr. Suddapalli Chaitanya Kumar**

Thesis submitted in partial fulfillment of the requirements
for the degree of Doctor of Philosophy of the
Universitat Politècnica de Catalunya

March 2019

Dedicated to my loving parents

Declaration

I hereby declare that the matter embodied and presented in the thesis entitled **"Novel pulsed optical parametric sources in the mid-infrared and the application towards high-resolution molecular spectroscopy"** is the result of investigations carried out by me at the ICFO – The Institute of Photonic Sciences, Castelldefels, Barcelona, Spain, under the supervision of Prof. Majid Ebrahim-Zadeh and Dr. Suddapalli Chaitanya Kumar, and that it has not been submitted elsewhere for the award of any degree or diploma. In keeping with the general practice in reporting scientific observations, due acknowledgment has been made whenever the work described is based on the findings of other investigators.

_____

Hanyu Ye

Certificate

I hereby certify that the matter embodied and presented in this thesis entitled **"Novel pulsed optical parametric sources in the mid-infrared and the application towards high-resolution molecular spectroscopy"** has been carried out by Mr. Hanyu Ye at the ICFO – The Institute of Photonic Sciences, Castelldefels, Barcelona, Spain, under my supervision, and that it has not been submitted elsewhere for the award of any degree or diploma.

_____

Prof. Dr. Majid Ebrahim-Zadeh

(ICFO, Research supervisor)

_____

Dr. Suddapalli Chaitanya Kumar

(ICFO, Research co-supervisor)

Acknowledgements

On the day of my first arrival in Barcelona three years back, I definitely couldn't imagine my PhD life would be such a wonderful journey. It has been my honor to work in Optical Parametric Oscillators group and ICFO as a PhD student. I have gained lots of knowledge and lab skills over the last three years. More importantly, the very international environment of ICFO for scientific research has greatly broadened my horizons. Here, I was taught to think in a more scientific and interdisciplinary way. All of these I obtained here are absolutely big treasures of my life and will keep me going on in my future career. However, I couldn't have completed the momentous task of this thesis without so many people's help and efforts.

First and foremost, I would like to express my deep gratitude to my supervisor, Professor Majid Ebrahim-Zadeh, for giving me the opportunity to pursue a PhD degree in his group. I feel very fortunate that I not only have the chance to work and explore in such a well-equipped lab, but also have been involved in the *Mid-TECH* project supported by EU's Horizon 2020 programme. Professor Ebrahim-Zadeh has also been encouraging me to attend various conferences and summer schools, where I greatly expanded my knowledge and improved my English skills. His deep understandings in the field of nonlinear optics, persistence in scientific research over years, and the pursuit of high-quality research outcomes, have deeply influenced and inspired me. I feel proud of being one of his students.

I am also grateful to my co-advisor, Dr. Suddapalli Chaitanya Kumar, for his guidance on my PhD work. Chaitanya is an outstanding young researcher full of knowledge and experience. He provided valuable ideas, prepared lots of equipment

and components for my experiments, and also took responsibility for my journal paper submissions and publications. I couldn't have completed my PhD work so smoothly without his efforts. I really enjoyed the time I spent with him in the lab and office.

Next, I wish to send my gratitude to Dr. Zhongshan Li at the division of combustion physics of Lund University, who supervised my collaborative experiment with his research team. Li trusted me and gave me the opportunity to work in his lab. During my stay in Lund University, I visited various labs for combustion research and laser spectroscopy, and started the work of combining our laser technology with spectroscopy applications. Although my stay was not very long, the memory there is always fresh and unforgettable to me.

I am also thankful to Professor Christian Pedersen, Peter Tidemand-Lichtenberg, and Dr. Peter John Rodrigo of DTU. They and their research group have played an important and irreplaceable role in the wonderful *Mid-TECH* project. Their respectable attitude to work and attractive achievements greatly impressed me.

My special thanks should go to my colleagues as well as friends, Anuja and Callum. We joined PhD study around the same time and have been encouraging and supporting each other all the time. The *Mid-TECH* project brought us even closer. We travelled for summer schools and conferences together and left lots of precious memories in different cities. My sincere thanks also go to many labmates as well as friends in our group, Pep, Biplob, Jun, Sukeert, Shahrzad and Kavita. I had a great time working with them and helping each other in such a friendly environment. Those coffee times when we shared experience and stories were also very enjoyable. I would like to thank Rasmus Lyngbye Pedersen of Lund University for contributing so much

to our collaborative experiments. He arranged components and instruments well before I went to Lund and spent time on explaining lots of spectroscopy basics to me.

I would also like to acknowledge the director of ICFO, Professor Lluis Torner, and the administrative staff in human resource office, front desk, purchasing department, IT department, mechanical and electronics workshop. I really appreciate their efforts to create such a convenient, diverse and well-organized environment.

To all the other PhD students in the *Mid-TECH* project, Michael Hermes, Pascaline Bouzy, Lichun Meng, Mahmoud Tawfieq, Laurent Huot, Ashik Abdul Rahim Sajeela Beevi, Morgan Mathez, Yu-Pei Tseng, Saher Junaid, Sylvain Mathonnière, Yohei Matsuoka and Ján Tomko, I offer many thanks. It was a pleasure meeting and networking with these excellent young researchers.

Finally, I would like to thank my parents, for their support and unconditional love. They brought me into this beautiful world, raised and educated me with their best, and then give me the freedom of pursuing my own dreams. I deeply appreciate what they have done for me all these year.

Abstract

The mid-infrared (mid-IR) spectral region coincides with fundamental rotational-vibrational transitions of a large number of molecules in the gas phase. The strong interaction between mid-IR light sources and these gaseous molecules has enabled experimental investigations of energy-level structures of various molecules and also led to a series of spectroscopic applications in, for example, biomedicine, environmental monitoring, and combustion diagnostics. Nanosecond pulsed optical parametric sources tunable in the mid-IR are versatile tools offering the potential to access different molecular transitions. Their compact size and relatively high pulse energy allow convenient and sensitive detection in various types of spectroscopy. Achievable narrow linewidths close to Fourier transform limit also make it possible to resolve Doppler-limited fine absorption lines and distinguish different species with high selectivity. As such, this thesis aims at the further development of pulsed optical parametric sources in the mid-IR region, employing different nonlinear materials and down-conversion configurations, as well as their application towards high-resolution molecular spectroscopy.

We have demonstrated optical parametric generation (OPG) in the newly invented nonlinear crystal, orientation-patterned gallium phosphide (OP-GaP). Pumped by a Q-switched Nd:YAG laser, the OPG source at 25 kHz repetition rate generates tunable radiation across 1721-1850 nm and 2504-2787 nm. Detailed characterization including temperature tuning, pump transmission, and OPG threshold validated the performance of OP-GaP as the next-generation quasi-phase-matched nonlinear material.

Following the development of the OPG, we further successfully demonstrated and characterized a singly-resonant optical parametric oscillator (OPO) based on OP-GaP. Driven by the same Nd:YAG laser at 50 kHz repetition rate, the OPO delivers mid-IR idler in the spectral range of 2.8-3.1 μm. Absorption-induced thermal effects in the OP-GaP sample were revealed and studied using different pump power levels.

We also demonstrated a stable, pulsed degenerate OPO at 2.1 μm based on MgO:PPLN and pumped by the same Nd:YAG laser with variable repetition rates from 65 kHz to 90 kHz. The OPO, in a Littrow-grating-cavity configuration, can provide up to 2.7 W of degenerate output with good pulse-to-pulse and long-term power stability. The spectral narrowing effect of the grating-cavity was also examined and compared to a plane-mirror linear cavity.

Finally, we developed a high-resolution difference-frequency spectrometer in the spectral range of 3308.5-3317.3 nm. The mid-IR source for the spectrometer was based on single-frequency, mode-hop-free tunable, pulsed difference-frequency-generation (DFG) in MgO:PPLN. A part of the methane spectrum in the Q-branch of v_3-band was resolved and compared to HITRAN simulation in both atmospheric pressure and reduced pressure. This conceptual technique can be extended to broader mid-IR regions for detecting various other molecules or to higher energy level for nonlinear spectroscopy with high resolution.

Resumen

La región espectral del infrarrojo-medio (mid-IR) coincide con las transiciones rotacional-vibracionales fundamentales de un elevado número de moléculas en la fase gaseosa. La intensa interacción de fuentes de luz del mid-IR con estas moléculas gaseosas ha posibilitado la ejecución de investigaciones experimentales sobre las estructuras de nivel energético de varias moléculas y ha conducido asimismo a una serie de aplicaciones espectroscópicas en ámbitos tales como la biomedicina, la vigilancia ambiental y los diagnósticos de combustión. Las fuentes ópticas paramétricas de pulsos de nanosegundos sintonizables en el mid-IR constituyen herramientas versátiles que brindan el potencial de acceder a diversas transiciones moleculares. Su tamaño compacto y la energía del pulso relativamente alta permiten una detección práctica y de alta sensibilidad en varios tipos de espectroscopia. Las anchuras de línea espectral estrechas alcanzables próximas al límite de la transformada de Fourier también posibilitan la precisión de las delgadas líneas de absorción limitadas por el efecto Doppler y la distinción de diferentes especies con una alta selectividad. De este modo, la presente tesis se centra en el mayor desarrollo de las fuentes ópticas paramétricas de pulsos en la región del mid-IR, mediante la utilización de materiales no lineales y configuraciones de conversión descendente, así como en su aplicación en la espectroscopia molecular de alta resolución.

Hemos demostrado la generación óptica paramétrica (OPG) en el cristal no lineal recientemente inventado OP-GaP. Bombeada por un láser Nd:YAG por conmutación Q, la fuente de OPG a una frecuencia de repetición de 25 kHz genera radiación sintonizable a 1721-1850 nm y 2504-2787 nm. Una detallada caracterización mediante ajuste de la temperatura, transparencia de la bomba y umbral de la OPG validó el rendimiento del OP-GaP como material no lineal de cuasi ajuste de fase.

Asimismo, tras el desarrollo de la OPG, demostramos y caracterizamos con éxito un Oscilador Paramétrico Óptico (OPO) simplemente resonante basado en el cristal OP-GaP. Bombeado por el mismo láser Nd:YAG con una frecuencia de repetición de 50 kHz, el OPO genera un campo pivote en el mid-IR en el rango espectral de 2,8-3,1 μm. Se revelaron y estudiaron los efectos térmicos inducidos por la absorción en la muestra de OP-GaP usando diferentes niveles de potencia de la bomba.

También hemos demostrado un OPO degenerado pulsado estable a 2,1 μm basado en un cristal de MgO:PPLN y bombeado por el mismo láser Nd:YAG con frecuencias de repetición variables entre 65 kHz y 90 kHz. El OPO, con la cavidad en configuración Littrow, puede proporcionar hasta 2,7 W de salida degenerada con una estabilidad de pulso y de potencia a largo plazo. También se examinó y comparó el efecto de estrechamiento espectral de la cavidad de rejilla de difracción en relación con una cavidad lineal de espejo plano.

Por último, desarrollamos un espectrómetro de diferencia de frecuencias de alta resolución en el rango espectral de 3308,5-3317,3 nm. La fuente de mid-IR para el espectrómetro se basó en una generación diferencia de frecuencias (DFG) sintonizable sin saltos de modo monofrecuencia en el cristal MgO:PPLN. Una parte del espectro de metano en la banda v_3 se resolvió y se comparó con la simulación HITRAN tanto a presión atmosférica como presión reducida. Esta técnica conceptual puede extenderse a regiones más amplias del mid-IR para detectar otras moléculas o se puede extender a un nivel energético superior para una espectroscopia no lineal de alta resolución.

Publications

Journal publications

1. **H. Ye**, S. C. Kumar, J. Wei, P. G. Schunemann, and M. Ebrahim-Zadeh, "Singly-resonant pulsed optical parametric oscillator based on orientation-patterned gallium phosphide," Opt. Lett. 43, 2454-2457 (2018).

2. B. Nandy, S. C. Kumar, J. C. Casals, **H. Ye**, and M. Ebrahim-Zadeh, "Tunable high-average-power optical parametric oscillators near 2 μm," J. Opt. Soc. Am. B 35, C57-C67 (2018).

3. J. Wei, S. C. Kumar, **H. Ye**, P. G. Schunemann, and M. Ebrahim-Zadeh, "Performance characterization of mid-infrared difference-frequency-generation in orientation-patterned gallium phosphide," Opt. Mater. Express 8, 555-567 (2018).

4. **H. Ye**, S. C. Kumar, J. Wei, P. G. Schunemann, and M. Ebrahim-Zadeh, "Optical parametric generation in orientation-patterned gallium phosphide," Opt. Lett. 42, 3694-3697 (2017).

5. J. Wei, S. C. Kumar, **H. Ye**, K. Devi, P. G. Schunemann, and M. Ebrahim-Zadeh, "Nanosecond difference-frequency generation in orientation-patterned gallium phosphide," Opt. Lett. 42, 2193-2196 (2017).

Conference and proceeding publications

1. **H. Ye**, S. C. Kumar, J. Wei, P. G. Schunemann, and M. Ebrahim-Zadeh, "Pulsed optical parametric generation and oscillation in orientation-patterned gallium phosphide," Conference on Lasers and Electro-Optics (CLEO), San Jose, California, USA, paper STh4F.6 (May 2018).

2. B. Nandy, **H. Ye**, S. C. Kumar, and M. Ebrahim-Zadeh, "Stable, high-average-power, narrow-linewidth source at 2.1 μm pumped at 1.064 μm," Conference on Lasers and Electro-Optics (CLEO), San Jose, California, USA, paper JTu2A.60 (May 2018).

3. V. Sharma, S. C. Kumar, A. Aadhi, **H. Ye**, G. K. Samanta, and M. Ebrahim-Zadeh, "Generation of vector vortex beam from doubly-resonant nanosecond optical parametric oscillator," Conference on Lasers and Electro-Optics (CLEO), San Jose, California, USA, paper FTh3E.8 (May 2018).

4. **H. Ye**, S. C. Kumar, J. Wei, P. G. Schunemann, and M. Ebrahim-Zadeh, "1 μm-pumped optical parametric generator and oscillator based on orientation-patterned gallium phosphide," Proc. SPIE 10684, 106841W (May 2018).

5. **H. Ye**, B. Nandy, S. C. Kumar, and M. Ebrahim-Zadeh, "Stable, high-average-power, degenerate optical parametric oscillator at 2.1 μm," Mid-infrared Coherent Sources (MICS), Strasbourg, France, paper JT5A.17 (March 2018).

6. **H. Ye**, S. C. Kumar, J. Wei, P. G. Schunemann, and M. Ebrahim-Zadeh, "Singly-resonant optical parametric oscillator based on orientation-patterned

gallium phosphide," Mid-infrared Coherent Sources (MICS), Strasbourg, France, paper MW2C.5 (March 2018).

7. **H. Ye**, S. C. Kumar, J. Wei, P. G. Schunemann, and M. Ebrahim-Zadeh, "Optical parametric generator based on orientation-patterned gallium phosphide," CLEO/Europe-EQEC, Munich, Germany, paper CD_10_3 (June 2017).

Contents

List of Tables

List of figures

Chapter 1

Introduction

1.1 Background

Laser science and technology have greatly changed our life and been continuously growing fast since the demonstration of the first working laser in 1960 [1]. Lasers not only offer valuable tools for many different scientific research fields which further enhance our understanding of nature, but also leading to various new applications in our life including optical communication, laser surgery, processing material, remote sensing in the atmosphere, and so on. The laser radiation originates from spontaneous emission between different energy levels in a suitable gain medium and undergoes amplification by stimulated emission in the same medium with the assistance of a cavity to provide optical feedback. The laser radiation differs from other kinds of light beams in terms of monochromaticity, coherence, directionality, brightness and short time duration [2]. These properties of laser make it possible to generate a light beam with high spectral density and low spatial divergence. Besides, cavity modulation techniques such as Q-switching and mode-locking can be used to generate short and ultra-short light pulses typically from nanosecond to femtosecond duration.

To date, matter of different states including solid, liquid and gas has been used as

effective laser media. Different media containing unique atomic or molecular energy level structures can emit different laser wavelengths. However, conventional lasers based on available gain media are still far away from full coverage of optical spectrum, especially the mid-infrared (mid-IR) region, where fundamental rotational-vibrational bands with strong absorption of a large number of gaseous molecules are located. The invention and development of semiconductor lasers have made it possible to create flexible laser wavelengths in the visible, infrared and even terahertz region. The compact on-chip design of such lasers is also greatly attractive for many real-world applications. The output beam quality, however, limited by the semiconductor structures is not comparable to conventional lasers. Besides, high-pulse-energy operation and ultra-short pulses containing instantaneous broadband spectral coverage are difficult to achieve in laser diodes.

Nonlinear optics, on the other hand, provides a feasible solution to extend laser wavelength coverage by mixing input optical frequencies in dielectric materials. The nature of instantaneous nonlinear interaction allows newly generated coherent beams at expected wavelengths to follow the temporal characteristics of the input pumps in various time-scales. In fact, as early as one year after the first laser was demonstrated, the first nonlinear optical phenomenon, *second-harmonic-generation* (*SHG*), was observed in crystalline quartz illuminated by a pulsed ruby laser at 694.3 nm [3]. Soon after the first *sum-frequency-generation* (*SFG*) experiment was reported in 1962 [4]. Using two ruby lasers operating at different wavelengths separated by 1 nm as pumps, the up-converted light was generated and observed in a triglycine sulfate crystal. In the same year, the complete nonlinear optics theory was formulated to mathematically reveal the law of nonlinear interactions between different optical waves in nonlinear gain media [5]. This fundamental and pioneering work has enabled prediction and manipulation of nonlinear optical phenomena precisely and efficiently. Subsequently,

in 1963, a parametric down-conversion process, optical *difference-frequency-generation* (*DFG*) satisfying the momentum condition, was experimentally achieved by frequency mixing a ruby laser with a mercury lamp in a KH_2PO_4 crystal [6]. About the same time, theoretical postulations of *optical parametric generation* (*OPG*) and *optical parametric oscillator* (*OPO*) were also proposed [7,8]. Following these theoretical and experimental progresses in nonlinear frequency conversion field, the first OPO prototype, which was pumped by a pulsed frequency-doubled Nd:$CaWO_4$ laser at 529 nm and based on a $LiNbO_3$ crystal as the nonlinear medium, was demonstrated in 1965 [9]. An OPO is an oscillator containing a nonlinear gain medium, which can convert energy from the *pump* photons into another two optical waves (called *signal* and *idler*) of lower frequency by means of parametric down-conversion process. OPOs, together with other frequency conversion sources, are nowadays commonly used as wavelength-tunable coherent sources for various scientific and industrial applications where arbitrary wavelengths are required.

Although the theoretical foundation for nonlinear optics was established in 1960s, the advancement of practical nonlinear frequency sources had been technologically limited for many years. In the 1980s, the invention of a new class of nonlinear crystals including $KTiOPO_4$ (KTP), β-BaB_2O_4 (β-BBO) and LiB_3O_5 (LBO) [10-13], and the gradual development and commercialization of solid-state lasers, greatly promoted the development of nonlinear frequency conversion sources. Nevertheless, the operating time-scale of such parametric sources was mainly limited to pulsed nanosecond regime at low repetition rate to overcome the low effective nonlinear coefficients of the nonlinear crystals. Later, in 1990s, further advancement of crystal fabrication technology enabled the realization of *quasi-phase-matching* (*QPM*) by periodically inverting the sign of second-order susceptibility of nonlinear crystals [14-17]. QPM technology can enable access to highest effective nonlinear coefficient of nonlinear

crystals for parametric processes, and can eliminate spatial walk-off effect, allowing the exploitation of a long crystal interaction length. Among all QPM crystals, periodically poled lithium niobate (PPLN) and lithium tantalite (PPLT) have bocome the most viable materials. They offer high nonlinear coefficients, wide transparency range from ultraviolet to ~4 μm, and relatively high damage threshold. Besides, high-quality PPLN and PPLT crystals with various QPM grating period designs, such as fan-out, cascaded and chirped gratings, have been well commercialized and thus widely available. As a result, OPOs and other frequency conversion sources ranging from *continuous-wave* (*cw*) to femtosecond regime, have been extensively investigated in recent years [18-20].

Optical parametric down-conversion sources for the mid-IR range of 2-10 μm are, nowadays, an important branch of laser frequency conversion field. Molecular vibrations involving stretching and bending motions of chemical bonds usually have resonant frequencies in this spectral range, which lead to strong light absorption at relevant wavelengths. For molecules in the gas phase, rotational motions may also introduce absorption in the microwave region. The superimposition between vibrational and rotational motions, in this case, will make the molecular absorption in the mid-IR a band comprising many lines. Thus, mid-IR parametric sources which can detect molecular absorption bands or resolve fine structures hold promises as powerful tools for rotational-vibrational spectroscopy, leading to both important fundamental research and many real-world applications, such as environmental monitoring, combustion diagnostics, and so on. Figure 1.1 shows some molecules with vibrational absorption bands in the mid-IR.

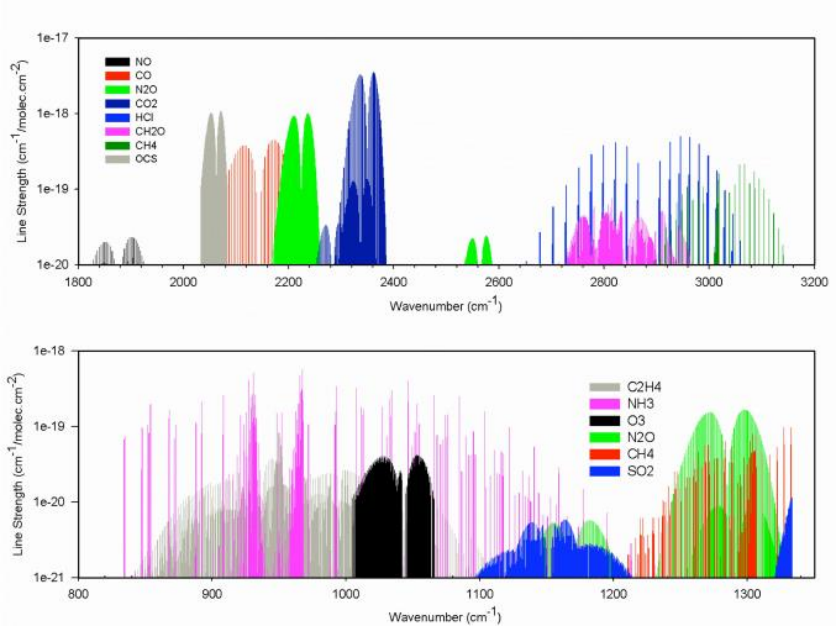

Figure 1.1. Molecules with absorption bands in the mid-IR [21].

Optical parametric sources in the nanosecond regime have been the most extensively studied and developed among all different time-scales. This is because the widely available nanosecond pulsed pump lasers can provide both high peak power and high pulse energy, making it easier to initiate parametric processes and increase conversion efficiencies. Besides, the relatively long nanosecond pulse duration allows the resonant wave of an OPO to have multiple round trips within the finite temporal window of each pump pulse without the need for synchronization between different pulses which is crucial in picosecond and femtosecond OPOs. Therefore, nanosecond OPOs can be usually much more compact and robust. For single-pass parametric processes such as *optical parametric amplification* (*OPA*) and DFG, the relatively long nanosecond pulses can eliminate the problem of group velocity mismatch, allowing long crystal interaction lengths to increase conversion efficiency. From the point of view of molecular spectroscopy, nanosecond parametric sources are also desirable. The high peak power and pulse energy is beneficial for increasing the

sensitivity of gas detection and have potential to be used in nonlinear spectroscopy such as degenerate four-wave mixing and polarization spectroscopy [22,23]. Moreover, the Fourier-transform-limited spectral widths of nanosecond pulses are usually around or below 100 MHz level, which is attractive for high-resolution, Doppler-limited molecular spectroscopy. Pulsed tunable optical parametric sources with such narrow linewidths will be able to resolve fine absorption lines of many molecules in gas, liquid and solid phases at room temperature.

In recent years, substantial efforts have been made in power scaling of pulsed mid-IR optical parametric sources. Output powers from multi-watt level to tens of watts have been obtained [24-32]. Among them, Y. Peng et al. reported a pulsed mid-IR OPA based on MgO:PPLN tunable from 2.68 to 3.07 μm with a highest average output power of 74.6 W, representing the highest record of any parametric down-conversion sources [31]. At longer mid-IR wavelength, B. Yao et al. reported a 41-W pulsed doubly-resonant OPO based on $ZnGeP_2$ (ZGP), delivering signal spectrum in 3.74-3.98 μm and idler spectrum in 4.38-4.76 μm [32].

There are also a large number of reports regarding the output pulse energy scaling of pulsed optical parametric sources. The traditional flash-pumped, high-energy solid-state lasers are commonly used for pumping high-energy down-conversion sources. In order to generate high pulse energy, the repetition rate of the pump lasers usually has to be decreased to the level of Hz to tens of Hz. Thus, the damage resistance of optical components against high pulse energy will become the main limit of further energy scaling, instead of the thermal effects which occur in high-average-power optical parametric sources. Fortunately, some birefringent nonlinear crystals, such as $KTiOPO_4$ (KTP), $KTiOAsO_4$ (KTA), BBO and ZGP, have relatively high laser energy damage threshold. Therefore, high-energy optical

parametric sources based on these crystals, especially OPOs, have become feasible in recent decades [33-42]. In the near-IR region, a signal pulse energy as high as 243 mJ at 1535.2 nm has been obtained from an injection-seeded KTA OPO [40]. In the mid-IR region of 3-5 μm, a similar pulse energy of 212 mJ containing signal and idler has also been generated from a Ho:YLF laser pumped $ZnGeP_2$ OPO followed by an OPA [41]. In the longer mid-IR region, a multi-stage OPA based on KTP, KTA and ZGP delivering as much as 8 mJ at 8 μm has also been reported [42].

With regard to the output wavelength of pulsed optical parametric sources, the most commonly used PPLN and PPLT crystals, as well as other oxide-based crystals, start to suffer from severe multi-phonon absorption at wavelengths beyond ~4 μm. Access to deeper mid-IR traditionally requires non-oxide nonlinear crystals with extended infrared transparency, such as $AgGaS_2$, $AgGaSe_2$, ZGP and orientation-patterned GaAs. These crystals, however, either have relatively low effective nonlinear coefficient or need to be pumped at or above ~2 μm to avoid two-photon pump absorption. Although idler wavelength emission beyond 10 μm or even 20 μm in optical frequency has been demonstrated [43-46], mid-IR pulsed parametric sources beyond ~4 μm are still technologically challenging and much less developed compared to those in the range of 2-4 μm.

1.2 Thesis outline

This thesis focuses on the development of novel pulsed optical parametric sources based on a newly emerging nonlinear crystal, orientation-patterned GaP (OP-GaP), and the mature MgO:PPLN, as well as the application of mid-IR pulsed parametric sources in high-resolution spectroscopy. The experimental work in the

thesis involves various configurations of parametric sources, including OPG, OPO and DFG. Two Q-switched Nd:YAG lasers were used as pumps to drive the above processes.

The thesis is organized as follows:

Chapter 2 introduces the basic theory of nonlinear optics and describes various parametric processes based on second-order nonlinearity. Coupled-wave equations are discussed to explain three-wave nonlinear interactions. Phase-matching condition, an important criterion for effective parametric processes, is introduced and different phase-matching techniques are later compared. Design issues and considerations for nanosecond pulsed OPOs are also discussed. Finally, the structure and basic properties of the newly developed nonlinear crystal, OP-GaP, are presented.

In chapter 3, we present the first demonstration of OPG based on OP-GaP. Pumped by a pulsed Nd:YAG laser 25 kHz repetition rate, the OPG can provide tuning across 1721-1850 nm and 2504-2787 nm with a highest total output power of 18 mW. The characteristics of temperature-dependent pump transmission of the OP-GaP sample have been investigated, indicating decreasing transmission of the OP-GaP crystal with increasing temperature. Other characteristics including power scaling, OPG threshold, pulse profile and power stability are also presented in this chapter.

In chapter 4, we describe the first singly-resonant nanosecond OPO based on OP-GaP. The OPO is designed in a compact plane-mirror cavity for optimizing the output power. Using a Nd:YAG laser as pump, the OPO is tunable across 2.8-3.1 μm and can deliver idler power up to 20 mW at 50 kHz repetition rate. In the temperature tuning measurement of the OP-GaP OPO, two different pump powers have been used in order to study and reveal the thermal effect of the OP-GaP sample. The results on

power scaling and stability, pump transmission, parasitic light, beam profile and pulse shape are also discussed in this chapter.

In chapter 5, a stable, high-average-power, degenerate MgO:PPLN OPO at 2.1 μm is demonstrated. A compact V-shape cavity in Littrow configuration comprising a blazed grating is used to restrict the broadband degenerate output spectrum. The OPO can provide multi-watt degenerate output power at three repetition rates of 65 kHz, 80 kHz and 90 kHz, in both linear cavity and grating-cavity configurations. Spectral width at degeneracy is examined in the grating-cavity OPO, showing a dramatic narrowing effect compared to the linear cavity OPO. The performance with regard to beam quality, power stability, pulse shape and pulse-to-pulse stability has also been characterized and presented in this chapter.

In chapter 6, we demonstrate a pulsed singly-frequency, mode-hop-free tunable, MgO:PPLN DFG source in the mid-IR. By frequency mixing the nanosecond single-frequency pump laser and the fiber-coupled, cw single-frequency diode laser, we can obtain DFG output tunable across 3308-3317 nm. Up to ~10 μJ of DFG output is generated at 10 Hz repetition rate. Using this DFG source, we further implemented methane absorption experiment at atmospheric pressure and reduced pressure. It is proven that the tunable DFG source with no mode hops is capable of achieving high-resolution molecular spectroscopy in the mid-IR.

Finally, in chapter 7, we present an overall summary of all experimental work and an outlook of this thesis.

Chapter 2

Basics of nonlinear optics

2.1 Nonlinear polarization

Nonlinear optics involves the interaction between light field of high intensity and matter. In the classical view, when a dielectric material is illuminated by an electromagnetic wave at optical frequency, the electrons and positive ions in each atom of the material will be driven to opposite directions, and dipoles will be formed in response to the applied electric field. These dipoles then start to follow the oscillation of the field and the material becomes polarized. When a weak electric field with a strength, $\boldsymbol{E}$, is applied to an isotropic material, the induced polarization $\boldsymbol{P}$ of the material linearly depends on $\boldsymbol{E}$, and can be described as [47]

$$\boldsymbol{P} = \varepsilon_0 \chi^{(1)} \boldsymbol{E} \tag{2.1}$$

where ε_0 is the permittivity of free space and $\chi^{(1)}$ is the linear susceptibility of the material. For anisotropic materials, $\chi^{(1)}$ becomes a second-order tensor, $\boldsymbol{\chi^{(1)}}$, comprising nine arguments and the relation between $\boldsymbol{P}$ and $\boldsymbol{E}$ can be expressed as

$$\begin{bmatrix} P_x \\ P_y \\ P_z \end{bmatrix} = \begin{bmatrix} \chi_{xx}^{(1)} & \chi_{xy}^{(1)} & \chi_{xz}^{(1)} \\ \chi_{yx}^{(1)} & \chi_{yy}^{(1)} & \chi_{yz}^{(1)} \\ \chi_{zx}^{(1)} & \chi_{zy}^{(1)} & \chi_{zz}^{(1)} \end{bmatrix} \begin{bmatrix} E_x \\ E_y \\ E_z \end{bmatrix} \tag{2.2}$$

As can be seen, the oscillation direction of the polarization, $\boldsymbol{P}$, doesn't have to

be parallel to the input electric field, $\boldsymbol{E}$, but still linearly depends on its strength. This is the regime of linear optics. However, as the strength of the input electric field increases, the polarization, $\boldsymbol{P}$, will start to show a nonlinear response with respect to $\boldsymbol{E}$. In this case, the relation between $\boldsymbol{P}$ and $\boldsymbol{E}$ can be further expressed with a power series in the electric field as [48,49]

$$\begin{aligned}\boldsymbol{P} &= \boldsymbol{P}^{(1)} + \boldsymbol{P}^{(2)} + \boldsymbol{P}^{(3)} + \cdots \\ &= \varepsilon_0 \boldsymbol{\chi}^{(1)} \boldsymbol{E} + \varepsilon_0 \boldsymbol{\chi}^{(2)} \boldsymbol{EE} + \varepsilon_0 \boldsymbol{\chi}^{(3)} \boldsymbol{EEE} + \cdots \end{aligned} \tag{2.3}$$

where $\boldsymbol{\chi}^{(\mathrm{i})}$ (i=2,3,…) represent high-order nonlinear susceptibilities, which enable the generation of nonlinear polarizations and further initiate frequency mixing of the input optical waves. If we consider second-order nonlinear polarization, $\boldsymbol{P}^{(2)} = \epsilon_0 \boldsymbol{\chi}^{(2)} \boldsymbol{EE}$, the quantity $\chi^{(2)}$ is estimated on the order of $\chi^{(1)}/E_{\mathrm{at}}$, where E_{at} is the characteristic atomic electric field strength. $\chi^{(2)}$ is, in fact, many orders of magnitude lower than $\chi^{(1)}$. Thus, only if we have strong interacting electric field, $\boldsymbol{E}$, for example laser radiation, $\boldsymbol{P}^{(2)}$ can reach a significant magnitude to result in nonlinear frequency mixing.

2.2 Expansion of second-order polarization

According to equation (2.3), we know that in second-order nonlinear optics two input optical waves can interact with each other in a nonlinear medium, and generate a third wave. This phenomenon can be described as three-wave mixing. Here, we express an optical wave of frequency of ω as

$$\boldsymbol{E}(t) = \boldsymbol{E}(\omega) e^{-j\omega t} + \boldsymbol{E}^{*}(\omega) e^{j\omega t} \tag{2.4}$$

Assuming that one input optical field comprises two waves of independent frequencies, ω_1 and ω_2, each of the two interacting electric fields, $\boldsymbol{E}$, can take ω_1

and ω_2, so the expression of second-order polarization, $\boldsymbol{P}^{(2)}$, can be unfolded as

$$\boldsymbol{P}^{(2)} = \varepsilon_0 \sum_{mn} \boldsymbol{\chi}^{(2)}(\omega_m, \omega_n) \cdot$$

$$\left[\boldsymbol{E}(\omega_m)e^{-j\omega_m t} + \boldsymbol{E}^*(\omega_m)e^{j\omega_m t}\right]\left[\boldsymbol{E}(\omega_n)e^{-j\omega_n t} + \boldsymbol{E}^*(\omega_n)e^{j\omega_n t}\right]$$

$$=\varepsilon_0\boldsymbol{\chi}^{(2)}(\omega_1,\omega_1)\boldsymbol{E}(\omega_1)\boldsymbol{E}(\omega_1)e^{-j2\omega_1 t}+\varepsilon_0\boldsymbol{\chi}^{(2)}(\omega_1,-\omega_1)\boldsymbol{E}(\omega_1)\boldsymbol{E}^*(\omega_1)+$$

$$\varepsilon_0\boldsymbol{\chi}^{(2)}(-\omega_1,\omega_1)\boldsymbol{E}^*(\omega_1)\boldsymbol{E}(\omega_1)+\varepsilon_0\boldsymbol{\chi}^{(2)}(-\omega_1,-\omega_1)\boldsymbol{E}^*(\omega_1)\boldsymbol{E}^*(\omega_1)e^{j2\omega_1 t}+$$

$$\varepsilon_0\boldsymbol{\chi}^{(2)}(\omega_1,\omega_2)\boldsymbol{E}(\omega_1)\boldsymbol{E}(\omega_2)e^{-j(\omega_1+\omega_2)t}+\varepsilon_0\boldsymbol{\chi}^{(2)}(\omega_1,-\omega_2)\boldsymbol{E}(\omega_1)\boldsymbol{E}^*(\omega_2)e^{-j(\omega_1-\omega_2)t}+$$

$$\varepsilon_0\boldsymbol{\chi}^{(2)}(-\omega_1,\omega_2)\boldsymbol{E}^*(\omega_1)\boldsymbol{E}(\omega_2)e^{j(\omega_1-\omega_2)t}+\varepsilon_0\boldsymbol{\chi}^{(2)}(-\omega_1,-\omega_2)\boldsymbol{E}^*(\omega_1)\boldsymbol{E}^*(\omega_2)e^{j(\omega_1+\omega_2)t}+$$

$$\varepsilon_0\boldsymbol{\chi}^{(2)}(\omega_2,\omega_1)\boldsymbol{E}(\omega_2)\boldsymbol{E}(\omega_1)e^{-j(\omega_1+\omega_2)t}+\varepsilon_0\boldsymbol{\chi}^{(2)}(\omega_2,-\omega_1)\boldsymbol{E}(\omega_2)\boldsymbol{E}^*(\omega_1)e^{j(\omega_1-\omega_2)t}+$$

$$\varepsilon_0\boldsymbol{\chi}^{(2)}(-\omega_2,\omega_1)\boldsymbol{E}^*(\omega_2)\boldsymbol{E}(\omega_1)e^{-j(\omega_1-\omega_2)t}+\epsilon_0\boldsymbol{\chi}^{(2)}(-\omega_2,-\omega_1)\boldsymbol{E}^*(\omega_2)\boldsymbol{E}^*(\omega_1)e^{j(\omega_1+\omega_2)t}+$$

$$\varepsilon_0\boldsymbol{\chi}^{(2)}(\omega_2,\omega_2)\boldsymbol{E}(\omega_2)\boldsymbol{E}(\omega_2)e^{-j2\omega_2 t}+\varepsilon_0\boldsymbol{\chi}^{(2)}(\omega_2,-\omega_2)\boldsymbol{E}(\omega_2)\boldsymbol{E}^*(\omega_2)+$$

$$\varepsilon_0\boldsymbol{\chi}^{(2)}(-\omega_2,\omega_2)\boldsymbol{E}^*(\omega_2)\boldsymbol{E}(\omega_2)+\varepsilon_0\boldsymbol{\chi}^{(2)}(-\omega_2,-\omega_2)\boldsymbol{E}^*(\omega_2)\boldsymbol{E}^*(\omega_2)e^{j2\omega_2 t} \tag{2.5}$$

As can be seen, the expansion contains sum-frequency terms $\pm(\omega_1+\omega_2)$, difference-frequency terms $\pm(\omega_1-\omega_2)$, second-harmonic terms $\pm2\omega_1$, $\pm2\omega_1$ and DC terms. These mutual interactions enable the generation of optical waves at new frequencies. If we extract the sum-frequency terms containing $e^{-j(\omega_1+\omega_2)t}$, the sum-frequency component of the induced polarization is

$$\boldsymbol{P}^{(2)}(\omega_1+\omega_2) = \varepsilon_0\boldsymbol{\chi}^{(2)}(\omega_1,\omega_2)\boldsymbol{E}(\omega_1)\boldsymbol{E}(\omega_2)e^{-j(\omega_1+\omega_2)t}+$$

$$\varepsilon_0\boldsymbol{\chi}^{(2)}(\omega_2,\omega_1)\boldsymbol{E}(\omega_2)\boldsymbol{E}(\omega_1)e^{-j(\omega_1+\omega_2)t} \tag{2.6}$$

$$=2\varepsilon_0[\boldsymbol{\chi}^{(2)}(\omega_1+\omega_2)\boldsymbol{E}(\omega_1)\boldsymbol{E}(\omega_2)e^{-j(\omega_1+\omega_2)t}]$$

where we can apply intrinsic permutation symmetry [48]

$$\boldsymbol{\chi}^{(2)}(\omega_1,\omega_2)=\boldsymbol{\chi}^{(2)}(\omega_2,\omega_1)=\boldsymbol{\chi}^{(2)}(\omega_1+\omega_2) \tag{2.7}$$

In the Cartesian coordinate system, $\boldsymbol{P}^{(2)}(\omega_1+\omega_2)$ can be projected to three different axes *x*,*y*, and *z*, so the projection on i direction (i=*x*, *y*, *z*) is

$$P_i^{(2)}(\omega_1+\omega_2)=2\varepsilon_0\sum_{jk}\chi_{ijk}^{(2)}(\omega_1+\omega_2)E_j(\omega_1)E_k(\omega_2) \tag{2.8}$$

Furthermore, if we take i on all values of *x*, *y*, and *z*, and fully expand $\boldsymbol{P}^{(2)}(\omega_1+\omega_2)$ to a matrix, it becomes

$$\begin{bmatrix}P_x^{(2)}(\omega_1+\omega_2)\\P_y^{(2)}(\omega_1+\omega_2)\\P_z^{(2)}(\omega_1+\omega_2)\end{bmatrix}=$$

$$2\varepsilon_0\begin{bmatrix}\chi_{xxx}^{(2)}&\chi_{xyy}^{(2)}&\chi_{xzz}^{(2)}&\chi_{xyz}^{(2)}&\chi_{xzy}^{(2)}&\chi_{xzx}^{(2)}&\chi_{xxz}^{(2)}&\chi_{xxy}^{(2)}&\chi_{xyx}^{(2)}\\\chi_{yxx}^{(2)}&\chi_{yyy}^{(2)}&\chi_{yzz}^{(2)}&\chi_{yyz}^{(2)}&\chi_{yzy}^{(2)}&\chi_{yzx}^{(2)}&\chi_{yxz}^{(2)}&\chi_{yxy}^{(2)}&\chi_{yyx}^{(2)}\\\chi_{zxx}^{(2)}&\chi_{zyy}^{(2)}&\chi_{zzz}^{(2)}&\chi_{zyz}^{(2)}&\chi_{zzy}^{(2)}&\chi_{zzx}^{(2)}&\chi_{zxz}^{(2)}&\chi_{zxy}^{(2)}&\chi_{zyx}^{(2)}\end{bmatrix}\begin{bmatrix}E_x(\omega_1)E_x(\omega_2)\\E_y(\omega_1)E_y(\omega_2)\\E_z(\omega_1)E_z(\omega_2)\\E_y(\omega_1)E_z(\omega_2)\\E_z(\omega_1)E_y(\omega_2)\\E_z(\omega_1)E_x(\omega_2)\\E_x(\omega_1)E_z(\omega_2)\\E_x(\omega_1)E_y(\omega_2)\\E_y(\omega_1)E_x(\omega_2)\end{bmatrix} \tag{2.9}$$

where the second-order susceptibility tensor consists of 27 Cartesian components. Likewise, based on equation (2.5), we can also obtain the polarization components of difference-frequency, second-harmonic and DC. Each of them will have the corresponding projection on all three axes in the Cartesian coordinate system. For example, for difference-frequency, $\omega_1-\omega_2$, it is

$$P_i^{(2)}(\omega_1-\omega_2)=2\varepsilon_0\sum_{jk}\chi_{ijk}^{(2)}(\omega_1-\omega_2)E_j(\omega_1)E_k^*(\omega_2) \tag{2.10}$$

and for second-harmonic, $2\omega_1$, it will be

$$P_i^{(2)}(2\omega_1)=\varepsilon_0\sum_{jk}\chi_{ijk}^{(2)}(2\omega_1)E_j(\omega_1)E_k(\omega_1) \tag{2.11}$$

Hence, from the above, we can see the origin of the second-order nonlinear interactions of optical waves in nonlinear media.

2.3 Nonlinear susceptibility

In equation (2.5), except the 4 DC terms, there are 12 remaining terms describing the generation of new frequencies. Each of these terms corresponds to a second-order susceptibility tensor with 27 Cartesian components. As a result, there are 324 different elements that we need to specify in order to describe second-order nonlinear interactions. However, these elements are fortunately not totally independent, so the number can be much reduced according to a series of restrictions. One of these restrictions is the intrinsic permutation symmetry we mentioned in equation (2.7). As the polarization induced by $E_j(\omega_m)E_k(\omega_n)$ is identical to the one induced by $E_k(\omega_n)E_j(\omega_m)$ in a nonlinear medium, their corresponding susceptibilities $\chi^{(2)}_{ijk}(\omega_m, \omega_n)$ and $\chi^{(2)}_{ikj}(\omega_n, \omega_m)$ must be equal. Using this principle, the numbers of independent tensor components of second-order susceptibility can be reduced from 324 to 162.

The second restriction we introduce below is the reality of the fields. If we consider the sum-frequency polarization in equation (2.5), it is

$$\boldsymbol{P_i} = P_i(\omega_1 + \omega_2)e^{-j(\omega_1+\omega_2)t} + P_i(-\omega_1 - \omega_2)e^{j(\omega_1+\omega_2)t} \tag{2.12}$$

As $\boldsymbol{P}$ is a physical quantity, which can be measured in reality, it must be a real number, so

$$P_i(\omega_1 + \omega_2) = P_i(-\omega_1 - \omega_2)^* \tag{2.13}$$

The susceptibilities of positive and negative frequency components must have the

following relation, due to $E_j(-\omega_1) = E_j(\omega_1)^*$ and $E_k(-\omega_2) = E_k(\omega_2)^*$,

$$\chi_{ijk}^{(2)}(\omega_1 + \omega_2) = \chi_{ijk}^{(2)}(-\omega_1 - \omega_2)^* \tag{2.14}$$

This property of nonlinear susceptibilities ensures the polarizations $\boldsymbol{P}^{(1)}$, $\boldsymbol{P}^{(2)}$, $\boldsymbol{P}^{(3)}$… to be real numbers, and also further reduces the number of independent tensor components from 162 to 81.

Except for intrinsic permutation symmetry, there is another important symmetry for the nonlinear susceptibility when the involved nonlinear medium is considered to be lossless. This symmetry is called full permutation symmetry, whose validity involves the quantum-mechanical expression for $\chi^{(2)}$ [48]. In this symmetry, all frequency arguments in the nonlinear susceptibility are freely swapped when the corresponding Cartesian indices are also swapped at the same time. An example is shown below in equation (2.15). Full permutation symmetry leads to a further reduction of the number of independent tensor components down to 27.

$$\chi_{ijk}^{(2)}(\omega_3 = \omega_1 + \omega_2) = \chi_{jki}^{(2)}(-\omega_1 = \omega_2 - \omega_3) = \chi_{jki}^{(2)}(\omega_1 = -\omega_2 + \omega_3) \tag{2.15}$$

When the mutually interacting optical waves have frequencies far from the resonance frequency of the nonlinear medium, the medium is necessarily lossless, which should be always the case if we design an optical frequency converter. Under this condition, we can apply the Kleinman's symmetry to the nonlinear susceptibility, which states [47,50,51]

$$\chi_{ijk}^{(2)} = \chi_{ikj}^{(2)} = \chi_{jik}^{(2)} = \chi_{jki}^{(2)} = \chi_{kij}^{(2)} = \chi_{kji}^{(2)} \tag{2.16}$$

As a result, we can divide the 27 tensor arguments of second-order nonlinear susceptibility into 10 independent groups. They are

$$\begin{gathered}
\chi^{(2)}_{111}, \quad \chi^{(2)}_{222}, \quad \chi^{(2)}_{333}, \\
\chi^{(2)}_{112} = \chi^{(2)}_{121} = \chi^{(2)}_{211}, \\
\chi^{(2)}_{113} = \chi^{(2)}_{131} = \chi^{(2)}_{311}, \\
\chi^{(2)}_{122} = \chi^{(2)}_{221} = \chi^{(2)}_{212}, \\
\chi^{(2)}_{322} = \chi^{(2)}_{223} = \chi^{(2)}_{232}, \\
\chi^{(2)}_{133} = \chi^{(2)}_{331} = \chi^{(2)}_{313}, \\
\chi^{(2)}_{233} = \chi^{(2)}_{332} = \chi^{(2)}_{323}, \\
\chi^{(2)}_{123} = \chi^{(2)}_{132} = \chi^{(2)}_{213} = \chi^{(2)}_{231} = \chi^{(2)}_{312} = \chi^{(2)}_{321}
\end{gathered} \tag{2.17}$$

Under the condition of Kleinman's symmetry, if we define d-tensor by [47]

$$d_{ijk} = \frac{1}{2}\chi^{(2)}_{ijk} \tag{2.18}$$

from equation (2.17) we know that $d^{(2)}_{i12} = d^{(2)}_{i21}$, $d^{(2)}_{i13} = d^{(2)}_{i31}$, $d^{(2)}_{i23} = d^{(2)}_{i32}$. Then we introduce a contracted notation d_{il} to simplify the 27-argument susceptibility. The correspondence between *jk* and *l* is

jk:	11	22	33	23,32	31,13	12,21
l:	1	2	3	4	5	6

(2.19)

The 27-argument tensor of second-order nonlinear susceptibility can be then replaced by one 18-argument matrix

$$\begin{bmatrix} d_{11} & d_{12} & d_{13} & d_{14} & d_{15} & d_{16} \\ d_{21} & d_{22} & d_{23} & d_{24} & d_{25} & d_{26} \\ d_{31} & d_{32} & d_{33} & d_{34} & d_{35} & d_{36} \end{bmatrix} \tag{2.20}$$

By applying the Kleinman symmetry here, we can further eliminate identical

elements and reduce the number of independent elements to 10, for example, $d_{12} = d_{12}$, $d_{15} = d_{31}$, and $d_{26} = d_{12}$. Using this simplified matrix, we can easily describe any second-order nonlinear polarization. The generated sum-frequency polarization, for instance, will be

$$\begin{bmatrix} P_x^{(2)}(\omega_1+\omega_2) \\ P_y^{(2)}(\omega_1+\omega_2) \\ P_z^{(2)}(\omega_1+\omega_2) \end{bmatrix} = 4\varepsilon_0 \begin{bmatrix} d_{11} & d_{12} & d_{13} & d_{14} & d_{15} & d_{16} \\ d_{21} & d_{22} & d_{23} & d_{24} & d_{25} & d_{26} \\ d_{31} & d_{32} & d_{33} & d_{34} & d_{35} & d_{36} \end{bmatrix} \begin{bmatrix} E_x(\omega_1)E_x(\omega_2) \\ E_y(\omega_1)E_y(\omega_2) \\ E_z(\omega_1)E_z(\omega_2) \\ E_y(\omega_1)E_z(\omega_2)+E_z(\omega_1)E_y(\omega_2) \\ E_x(\omega_1)E_z(\omega_2)+E_z(\omega_1)E_x(\omega_2) \\ E_x(\omega_1)E_y(\omega_2)+E_y(\omega_1)E_x(\omega_2) \end{bmatrix} \quad (2.21)$$

d-tensor here is a property of a nonlinear medium, so different materials have significantly different values of arguments in the matrix of *d*-tensor. These values are very important in nonlinear frequency conversion processes, as they and their distribution in the matrix can decide the strength of response of nonlinear polarization to a fixed input optical intensity. It's always desirable to achieve high efficiency when designing nonlinear frequency converters. For this purpose, we need to choose nonlinear materials with high d_{il} values and optimize the polarizations of the involved optical waves. For example, in lithium niobate ($LiNbO_3$), the highest nonlinear coefficient is d_{33}~25 pm/V, and d_{13}=d_{23}=0. If we want to use the largest coefficient, d_{33}, and avoid interferences from other coefficients in the matrix, we should set the input optical field is purely along *z*-axis of lithium niobate according to equation (2.21). Thus, we can generate nonlinear polarization, $\boldsymbol{P}$, most efficiently along the *z*-axis as well.

2.4 Second-order nonlinear processes

From the previous description in section 2.2, we now know that three-wave interactions based on second-order nonlinearity consist of different optical frequency mixing processes, including sum-frequency-generation (SFG), difference-frequency-generation (DFG) and second-harmonic-generation (SHG). In this section, we aim to provide a more detailed explanation of these second-order parametric processes. Figure 2.1 illustrates the practical realization of the corresponding processes. The SFG, shown in Figure 2.1(a), describes how two pump photons of low frequencies, ω_1 and ω_2, are combined in the nonlinear medium to create a new photon of high frequency, $\omega_3 = \omega_1 + \omega_2$. This also means that SFG process can convert two long optical wavelengths to one short wavelength. Based on this principle, much of the frequency up-conversion technology has been developed, enabling the generation of short-wave coherent light [52-56] and the detection of mid-IR optical information using low-noise and less-complex visible/near-IR detectors based on Si and InGaAs [57-62]. The SHG process, shown in Figure 2.1(b), is similar to SFG process, where two low-frequency photons combine to create a high-frequency photon. However, the two pump low-frequency photons in SHG have the same frequency, $\omega_1 = \omega_2$, so this process is also called frequency doubling. Here, the two input photons can come from the same input light beam, and there is no quantum loss during the conversion process, so it's usually easy to reach a high SHG conversion efficiency. SHG has already become a well-established technology for visible and ultraviolet laser light generation [63-65].

In DFG process, shown in Figure 2.1(c), two pump photons, ω_3 and ω_1, interact with each other and generate a new photon, $\omega_2 = \omega_3 - \omega_1$. Therefore, DFG is usually used to generate long-wavelength optical radiation, especially the important

mid-IR and even terahertz region. Figure 2.1 (d) shows another type of frequency conversion process, known as optical parametric generation (OPG), which is similar to DFG, but doesn't need a second input beam. In OPG, a high-frequency pump photon, ω_3, can spontaneously split into another two new photons, ω_1 and ω_2, where $\omega_3 = \omega_1 + \omega_2$. The OPG process is usually considered to initiate from the interaction between the pump source and quantum noise [66]. If we provide feedback for an OPG process, this results in a device known as an optical parametric oscillator (OPO), as shown in Figure 2.1(e). The feedback can be realized by introducing a cavity where at least one of the generated light beams is resonant. Compared to OPG, an OPO can significantly improve the conversion efficiency and lower the threshold, thus allowing low pump intensity operation, even in cw regime.

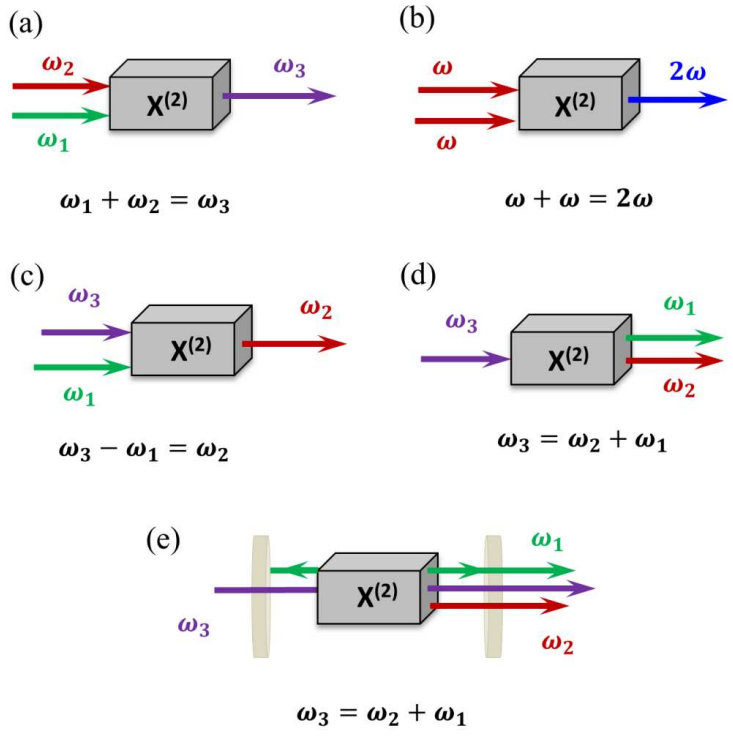

Figure 2.1. Schematic of second-order nonlinear processes.

(a) SFG, (b) SHG, (c) DFG, (d) OPG, and (e) OPO.

2.5 Coupled-wave equations for three-wave mixing processes

By now we have seen what second-order frequency mixing processes can occur in a nonlinear medium and how the induced nonlinear polarizations respond to the intense incident laser field. In this section, we further introduce nonlinear polarizations into Maxwell's wave equations to explain the generation of new frequency components of the field. This will give us a more general view of how the involved optical waves are coupled through nonlinear interactions.

In a non-magnetic medium containing no free charges and currents, the classical form of the wave equation is written as [48]

$$-\nabla^2 \boldsymbol{E} + \frac{1}{c^2}\frac{\partial^2 \boldsymbol{E}}{\partial t^2} = -\mu_0 \frac{\partial^2 \boldsymbol{P}}{\partial t^2} \tag{2.22}$$

where c is the velocity of light in vacuum, $c = 1/\sqrt{\varepsilon_0 \mu_0}$, and μ_0 is the permeability of free space. From this equation, we can see that when an electric field is propagating through a dielectric medium, it will induce polarization, and conversely, this polarization will also affect the propagation of the incident field in the medium. If we only consider the linear polarization, $\boldsymbol{P} = \boldsymbol{P}^{(1)}$, the electric field, $\boldsymbol{E}$, transmitted through the medium will remain the same as the input field. Equation (2.22) in this case can be simplified to

$$\nabla^2 \boldsymbol{E} - \frac{\boldsymbol{\varepsilon}_r^{(1)}}{c^2}\frac{\partial^2 \boldsymbol{E}}{\partial t^2} = 0 \tag{2.23}$$

where $\boldsymbol{\varepsilon}_r^{(1)} = \mathbf{1} + \boldsymbol{\chi}^{(1)}$. However, when we consider a polarization comprising both linear and second-order nonlinear components, $\boldsymbol{P} = \boldsymbol{P}^{(1)} + \boldsymbol{P}^{(2)}$, the wave equation becomes

$$\nabla^2 \boldsymbol{E} - \frac{\boldsymbol{\varepsilon}_r}{c^2}\frac{\partial^2 \boldsymbol{E}}{\partial t^2} = \mu_0 \frac{\partial^2 \boldsymbol{P}^{(2)}}{\partial t^2} \tag{2.24}$$

Compared to (2.23), one more term related to $\boldsymbol{P}^{(2)}$ occurs on the right-hand side of equation (2.24). Due to this nonlinear source term, the electric field won't be able to remain the same after propagating through the medium and new frequencies of electric field will be generated.

We assume that there are three plane waves interacting in a nonlinear medium at frequencies, ω_1, ω_2, ω_3, and $\omega_3 = \omega_1 + \omega_2$, and they all propagate along the z-direction. The solution to the classical wave equation can be written as

$$E_i(\mathrm{z},\mathrm{t}) = E(\mathrm{z},\omega_i)e^{j(k_i z-\omega_i t)} + c.c. \tag{2.25}$$

where, i takes 1, 2, 3, representing the involved three waves and $E(\mathrm{z},\omega_i)$ is the amplitude of the corresponding wave. The nonlinear source term in equation (2.24) is represented as

$$P_i(\mathrm{z},\mathrm{t}) = P(\mathrm{z},\omega_i)e^{j(k_i z-\omega_i t)} + c.c. \tag{2.26}$$

where k_i is the corresponding wavenumber described as

$$k_i = \frac{n_i(\omega_i)\omega_i}{c} \tag{2.27}$$

and the refractive index $n_i(\omega_i)$ is expressed as

$$n_i(\omega_i) = \sqrt{\frac{\varepsilon^{(1)}(\omega_i)}{\varepsilon_0}} = \sqrt{\varepsilon_r^{(1)}} \tag{2.28}$$

When we unfold the wave equation, ∇^2 can be replaced by d^2/dz^2, and it is usually reasonable to neglect the term, d^2E_i/dz^2, due to the slowly-varying amplitude approximation expressed as

$$\left|\frac{d^2E_i}{dz^2}\right| \ll \left|k_i\frac{dE_i}{dz}\right| \tag{2.29}$$

Using the equations and considerations above, the nonlinear wave equation (2.24) for the three fields in a lossless medium becomes

$$\frac{dE_3}{dz} = \frac{2jd_{eff}\omega_3^2}{k_3c^2}E_1E_2e^{j\Delta kz}$$

$$\frac{dE_2}{dz} = \frac{2jd_{eff}\omega_2^2}{k_2c^2}E_3E_1^*e^{-j\Delta kz} \tag{2.30}$$

$$\frac{dE_1}{dz} = \frac{2jd_{eff}\omega_1^2}{k_1c^2}E_3E_2^*e^{-j\Delta kz}$$

where d_{eff} is defined in terms of the effective nonlinear coefficient, $\chi_{eff}^{(2)}$, as

$$d_{eff} = \frac{\chi_{eff}^{(2)}}{2} \tag{2.31}$$

and the quantity, Δk, is called the momentum mismatch or phase-mismatch, expressed as

$$\Delta k = k_1 + k_2 - k_3 \tag{2.32}$$

Equations (2.30) are the coupled-wave equations, which describe how an optical wave is varying as a function of its coupling to the other two waves in a second-order nonlinear process.

Based on the coupled-wave equations, we further take an example of SHG to mathematically show how the frequency-doubled wave, ω_2, varies with the pump, ω_1, along a nonlinear medium. As there are only two waves interacting in SHG, the derived coupled-wave equations can be simplified as

$$\frac{dE_2}{dz} = \frac{jd_{eff}\omega_2^2}{k_2c^2}E_1^2e^{j\Delta kz}$$

$$\frac{dE_1}{dz} = \frac{2jd_{eff}\omega_1^2}{k_1c^2}E_2E_1^*e^{-j\Delta kz} \tag{2.33}$$

The phase-mismatch, Δk, has the expression of $\Delta k = 2k_1 - k_2$, where k_1 and k_2 are the wave vectors of the two beams at ω_1 and ω_2, respectively. When the SHG

conversion efficiency is low, the pump intensity can be treated as a constant value without depletion. Thus, we have $\mathrm{d}E_1/dz = 0$, and the SHG amplitude at the input to the nonlinear medium is zero, $E_2(0)$=0. Under this condition, equations (2.33) can be solved analytically with plane wave approximation. If the interaction length of the nonlinear medium is $z = L$, the SHG intensity, I_2, generated from the nonlinear medium can be obtained as

$$I_2 = \frac{2\omega_1^2 d_{eff}^2 L^2 I_1^2}{n_2 n_1^2 \varepsilon_0 c^3} sinc^2\left(\frac{\Delta kL}{2}\right) \tag{2.34}$$

where we have the definition of *sinc* function expressed as

$$sinc(x) = \frac{\sin(x)}{x} \tag{2.35}$$

In equation (2.34), the SHG intensity, I_2, can be maximized if Δk=0. This is called the *phase-matching* condition. In the next section, we will discuss this in more detail. Besides, we can see that I_2 also increases with the effective nonlinear coefficient, interaction length, and the square of pump intensity.

2.6 Phase-matching

As discussed in the previous section, in order to achieve efficient SHG, the phase-matching condition has to be fulfilled, which means $\Delta k = 2k_1 - k_2 = 0$. Indeed, the phase-matching condition is required for efficient conversion not only in SHG process, but also in other second-order nonlinear processes. In order to illustrate the dependence of normalized gain on the phase-mismatch, we plot the normalized gain as a $sinc^2$ function of the total phase-mismatch, $\Delta kL/2$, as shown in Figure 2.2. When the absolute value of $\Delta kL/2$ increases from zero to π, the normalized gain will drop to zero.

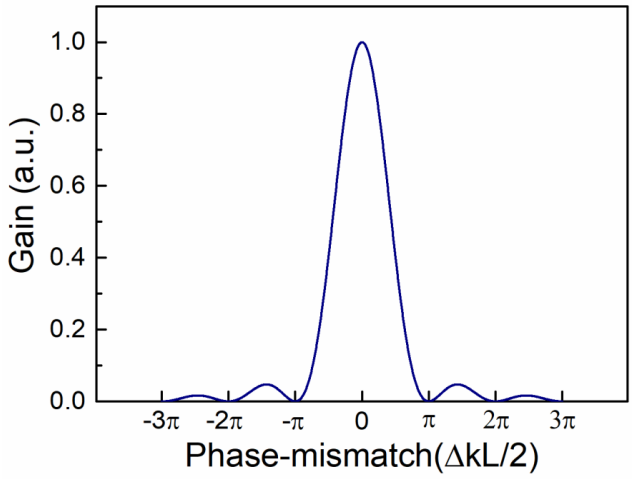

Figure 2.2. Effects of phase-mismatch on the normalized parametric gain.

When we have the condition of $\Delta k \neq 0$, the interacting waves in the nonlinear medium don't have a fixed phase difference, so that they won't be able to keep the maximized interference status along the propagation direction. In this case, the absolute phase difference will be changing between 0 and 2π, and the generated output power will be oscillating back and forth along the propagation direction. The longest interaction length over which power can still flow from the pump to the generated wave is $L_c = \pi/\Delta k$, which is called *coherence length*. Thus, the oscillating period of the generated power will be $2L_c$. The smaller Δk, the longer L_c. If $\Delta k = 0$, we will have an infinitely long L_c, which corresponds to the phase-matching condition. Figure 2.3 shows a comparison of the variation of the field amplitude of the generated wave under perfect phase-matching and phase-mismatched condition. As can be seen, the amplitude shows a linear increase with the interaction length under phase-matching and exhibits an oscillation under phase-mismatched condition. In order to achieve phase-matching for efficient wavelength conversion, two important techniques have been developed: birefringent phase-matching (BPM) and quasi-phase-matching (QPM).

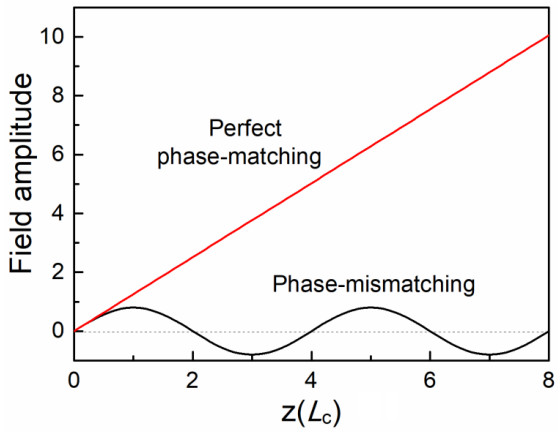

Figure 2.3. The spatial variation of the field amplitude of the generated wave along the propagation direction in the cases of perfect phase-matching and phase-mismatching.

2.6.1 Birefringent phase-matching

Birefringent phase-matching is the earliest practical method to achieve phase-matching by exploiting optical anisotropy of nonlinear crystals. If we consider the SHG process, the phase-matching condition is $2k_1 = k_2$, as discussed previously. Based on equation (2.27), we can further express this as

$$\frac{2n_1}{\lambda_1} = \frac{n_2}{\lambda_2} \tag{2.36}$$

where λ_1 and λ_2 are the wavelengths of the pump and SHG wave, respectively, so that $\lambda_1 = 2\lambda_2$. Thus, the phase-matching condition becomes $n_1 = n_2$. In the normal dispersion regime of a nonlinear medium, we always have the refractive index relation of $n_1 < n_2$, so the phase-matching condition seems not achievable here. However, in a birefringent crystal, beams in different polarizations have different refractive index distributions. We can assign the pump and SHG beams to different polarizations to make sure they have the same refractive index for phase-matching. For the most common uniaxial crystals, the refractive index distribution of the *ordinary* light is a sphere, which means the refractive index doesn't change with the

beam incident angle. However, for the *extraordinary* light, the refractive index distribution is an ellipsoid. Figure 2.4(a) and (b) show two types of uniaxial birefringent crystals, positive uniaxial crystals ($n_e > n_o$) and negative uniaxial crystals ($n_e < n_o$). The refractive index of the extraordinary light $n_e(\theta)$ at any direction in the crystal can be calculated according to the ellipse equation

$$\frac{\sin^2\theta}{n_e^2} + \frac{\cos^2\theta}{n_o^2} = \frac{1}{n_e(\theta)^2} \tag{2.37}$$

where θ is the angle between the optic axis and the propagation direction.

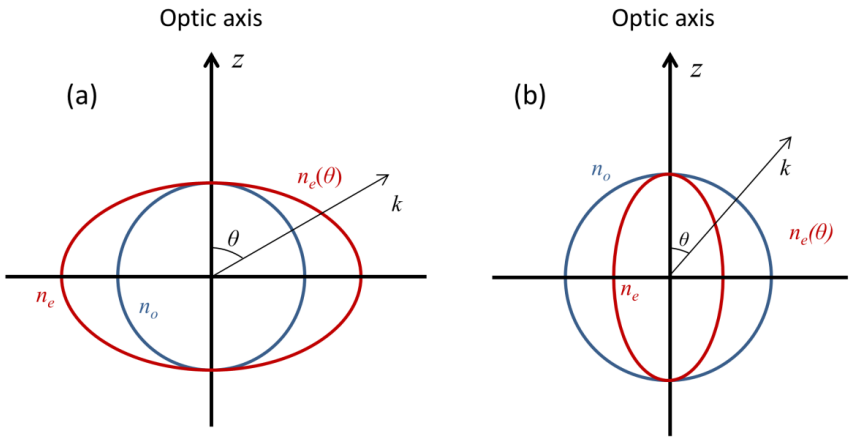

Figure 2.4. Refractive index distributions for (a) positive uniaxial crystal and (b) negative uniaxial crystal.

Considering the positive uniaxial crystal model, we can assign the pump beam to extraordinary beam and the SHG beam to ordinary beam. In this situation, we will be able to find a proper angle, θ, where the refractive index of the pump $n_e^p(\theta)$ equals to that of the SHG beam, n_o^s, as illustrated in Figure 2.5. In this way, we can fulfill the phase-matching condition $\Delta k = 0$ to maximize the SHG conversion efficiency. Here the two low-frequency pump photons have the same polarization, so we name it type I phase-matching. In the case of type II phase-matching, the two low-frequency

beams should have different polarizations.

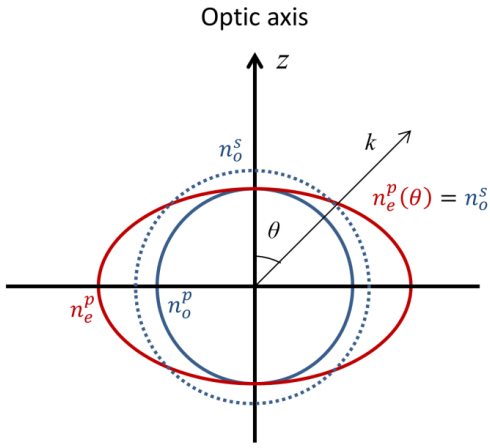

Figure 2.5. Type I phase-matching scheme for SHG in a positive uniaxial crystal.

Except for Δk, we know that the effective nonlinear coefficient, d_{eff}, of the crystal and the crystal interaction length are also crucial for improving the conversion efficiency. However, in birefringent phase-matching, the polarizations of the involved beams are restricted to be specific for phase-matching, so the corresponding d_{eff} usually can't be maximized and the effective interaction length is also limited by the spatial walk-off between the ordinary and extraordinary beams in birefringent crystals. These are some of the limitations of birefringent phase-matching.

2.6.2 Quasi-phase-matching

The principle of quasi-phase-matching was proposed in 1962, for the first time [5]. However, it was not realized and widely used until the 1990s due to the unavailability of material processes. The QPM technique can achieve similar results to birefringent phase-matching by allowing a monotonic flow of energy from the pump to the generated waves along the propagation direction. The idea of QPM is to periodically invert the sign of d_{eff} in the nonlinear crystal every coherence length so

that the phase-mismatch, Δk, can be compensated. An illustration of QPM structure is shown in Figure 2.6.

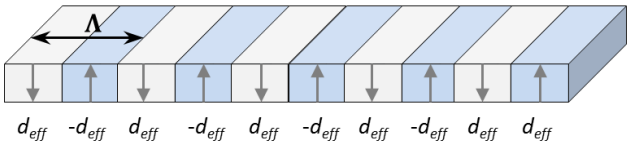

Figure 2.6. Illustration of QPM structure with periodically inverted sign of d_{eff}.

As we know, under phase-mismatched condition, energy flow between the pump and the generated waves changes its flowing direction by every coherence length, L_c. If we invert the sign of d_{eff} every L_c, and create a reversal period of $\Lambda = 2L_c$, the photon energy will keep the same flow direction and will grow monotonically, as shown in Figure 2.7.

The mathematical expression of the nonlinear coupling coefficient, $d(z)$, along z-axis can be given as

$$d(z) = \begin{cases} d_{eff}, z \in [2mL_c, (2m+1)L_c] \\ -d_{eff}, z \in [(2m-1)L_c, 2mL_c] \end{cases} \tag{2.38}$$

where m is an integer. We can further express equation (2.38) in terms of a Fourier series as

$$d(z) = d_{eff} \sum_{m=-\infty}^{\infty} a_m \exp(jm\frac{2\pi}{\Lambda}z) \tag{2.39}$$

where

$$a_m = \frac{1-\cos m\pi}{m\pi} \quad (m \neq 0) \tag{2.40}$$

If we substitute equations (2.39) and (2.40) into the coupled-wave equations (2.30), we can obtain the QPM condition as

$$k_1 + k_2 - k_3 = m\frac{2\pi}{\Lambda} \tag{2.41}$$

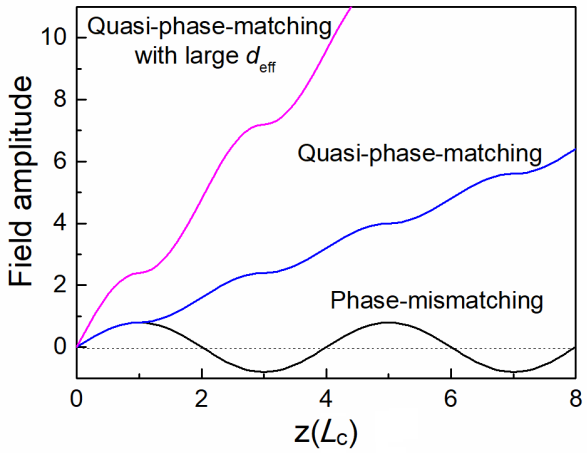

Figure 2.7. The spatial variation of the field amplitude of the generated wave along the propagation direction in the cases of quasi-phase-matching and phase-mismatching.

If the QPM term, $2m\pi/\Lambda$, on the right-hand side of equation (2.41) doesn't exist here, the generated waves won't be able to efficiently couple with the pump, due to phase mismatch, $\Delta k = k_1 + k_2 - k_3 \neq 0$. It is usually desirable to take the first-order (m=1) interaction. Thus, we have $a_m = 2/\pi$ and the final effective nonlinear coefficient in a QPM crystal is

$$d_e = \frac{2}{\pi} d_{eff} \tag{2.42}$$

In QPM process, the effective nonlinear coefficient that can be exploited always has an attenuation coefficient, $2\mathrm{m}/\pi$, compared to BPM, as it doesn't exactly fulfill the perfect phase-matching condition. However, in QPM process, the phase-mismatch can be compensated along any direction, so that one can choose the propagation axis and beam polarizations in a crystal corresponding to access the largest d_{eff} to achieve higher efficiency, as illustrated in Figure 2.7. In this case, even if we consider the attenuation coefficient, $2\mathrm{m}/\pi$, the final d_e can be still larger than that usable in

perfect BPM. Besides, by choosing an appropriate propagation axis in the crystal, the spatial walk-off can be also eliminated, which allows further increase of the effective interaction length of the nonlinear crystal for more efficient wavelength conversion. For instance, in the most widely used QPM crystal, periodically poled $LiNbO_3$ (PPLN), the beam propagation direction is set along the *x*-axis of the crystal without spatial walk-off issue and all beam polarizations are required to be extraordinary light (type 0: eee) in the crystal to access the largest d_{eff}. Besides, by scanning QPM crystal temperature or designing different inverted grating periods, one can easily find the QPM condition for a specific wavelength generation or conveniently tune the output wavelength over a wide range. Moreover, QPM technique allows the use of non-birefringent materials as nonlinear gain media, which opens up the possibility of exploiting cubic crystals such as GaAs with wide transparency window and large nonlinear coefficient for wavelength conversion.

2.7 Optical parametric gain and amplification

As this thesis focuses on the parametric generation of infrared coherent light, in this section, we discuss optical parametric gain in the down-conversion process. In single-pass down-conversion interaction, namely OPG, the pump will interact with the quantum noise and amplify the noise along the propagation axis. If the gain is strong enough, for example when we are using a high-peak-power pulsed pump laser, we will be able to obtain measurable output power at two new wavelengths. The generated shorter wavelength is named *signal* and the longer one is named *idler*. We define the net parametric gain of the signal obtained after passing through a nonlinear crystal as [49]

$$G_s = \frac{I_s(L) - I_s(0)}{I_s(0)} = \frac{I_s(L)}{I_s(0)} - 1 \tag{2.43}$$

where I_s is the signal intensity and L is the crystal length. Thus, G_s can be derived by solving the coupled-wave equations (2.30) under the condition of constant pump intensity, and expressed as

$$G_s = \Gamma^2 L^2 \frac{\sinh^2\left(\sqrt{\Gamma^2 L^2 - \left(\frac{\Delta k L}{2}\right)^2}\right)}{\Gamma^2 L^2 - \left(\frac{\Delta k L}{2}\right)^2} \tag{2.44}$$

where the gain factor, Γ, is defined as

$$\Gamma^2 = \frac{8\pi^2 d_{eff}^2}{c\varepsilon_0 n_p n_s n_i \lambda_s \lambda_i} I_p(0) \tag{2.45}$$

Here n represents refractive index, λ represents wavelength, and I_p is the pump intensity. If we further consider the case of small-signal gain, equation (2.44) can be simplified and have a familiar $sinc^2$ expression

$$G_s = \Gamma^2 L^2 sinc^2\left(\frac{\Delta k L}{2}\right) \tag{2.46}$$

In the case of strong signal gain and phase-matching, the term of $\left(\frac{\Delta k L}{2}\right)^2$ approaches zero, thus the parametric gain becomes

$$G_s = \sinh^2(\Gamma L) \tag{2.47}$$

If the gain is strong enough to ensure $\Gamma L \gg 1$, equation (2.47) approximates to

$$G_s \cong \frac{1}{4} e^{2\Gamma L} \tag{2.48}$$

So we can see that the strong signal parametric gain under phase-matching condition can be coarsely described and predicted using an exponential function.

2.8 Nanosecond optical parametric oscillator

From the preceding discussion, we know that in the OPG process, there will be spontaneously down-converted parametric waves generated at longer wavelengths. However, the single-pass parametric gain in OPG described by equation (2.43) in many cases is not sufficient enough to achieve macroscopic amplification, especially in cw and high-repetition-rate pulsed operation, where the pump peak power is relatively low. Therefore, it's necessary to introduce a cavity to the OPG process and form an OPO. Using an oscillator similar to a conventional laser, at least one of the generated parametric waves can be resonated in the OPO cavity to provide enhanced nonlinear interaction in successive passes through the nonlinear crystal. In this way, the efficiency of the down-conversion process can be much improved to a considerable level, operation threshold can be reduced, and coherent radiation can be extracted from the oscillator.

2.8.1 Oscillator configurations

In an operating OPO, the parametric gain of every single pass must overcome the cavity loss to attain operation threshold. This can be achieved by providing power feedback using different cavity configurations. Figure 2.8 shows an illustration of four common OPO configurations depending on the number of resonant waves in the cavity. If we only resonate one of the signal or idler waves, it is called a *singly-resonant oscillator* (*SRO*), as shown in Figure 2.8(a). In a *doubly-resonant oscillator* (*DRO*), Figure 2.8(b), both the signal and idler are resonant simultaneously in the cavity and the residual pump beam is extracted in a single pass. DRO operation can provide a lower threshold than SRO. When all the three waves are resonant simultaneously, the OPO becomes a *triply-resonant oscillator* (*TRO*), Figure 2.8(c),

which has an even lower threshold than DRO. DRO and TRO are particularly attractive for cw operation, as the cw pump intensity is relatively low. However, the wavelength stability and smooth wavelength tuning become a problem in DRO and TRO. When we have a fixed pump wavelength for a DRO, the exact wavelengths of the generated signal and idler will be confined by photon energy conservation. Thus, a fixed cavity length usually can't make sure both of the two generated waves are resonant simultaneously, unless we use specific technique to fine tune the cavity length. The same problem will also occur in TROs. The invention of *pump-enhanced SRO* (*PE-SRO*) can overcome some of the instability issue of DROs and TROs. In PE-SRO configuration, Figure 2.8(d), we resonate one of the generated waves together with the pump, so that the pump intensity is enhanced to reduce the threshold and the SRO operation of the generated waves is maintained more easily for wavelength stability and smooth tuning.

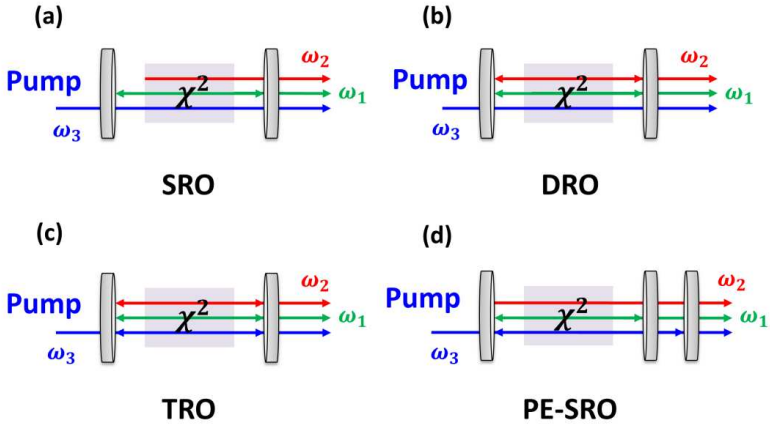

Figure 2.8. Cavity configurations for OPOs.

(a) singly-resonant, (b) doubly-resonant, (c) triply-resonant, (d) pump-enhanced.

In nanosecond OPOs, the simplest SRO is the most common choice, as nanosecond pulsed pump lasers usually have high pulse energy and high peak power to ensure high parametric gain and reach operation threshold. Nanosecond DROs are

more common in the degenerate case where the signal and idler output spectra are overlapped and indistinguishable.

In SRO configuration, it's also possible to design various cavity geometries, such as linear cavity, L-shape cavity, X-shape cavity and bow-tie ring cavity. However, in nanosecond OPOs with typical pump pulse durations of a few ns to tens of ns, the efficiency is strongly dependent on the cavity length, as the resonant wave only has limited numbers of round trips in the cavity over the pump pulse temporal window. In this case, a cavity with as short physical length as possible is always desirable. Thus, short linear cavity is usually the most efficient cavity choice for nanosecond OPOs. Other cavity designs can also be considered when more optical elements such as etalons or diffraction gratings are needed to be included in the cavity.

2.8.2 Cavity design considerations

An optimal OPO cavity design can provide efficient coupling between the pump and the resonant wave. The criterion of the design is that the interacting waves should have the same focusing parameter or confocal parameter, which is called mode-matching. The focusing parameter is defined as [67]

$$\xi = \frac{L}{b} \tag{2.49}$$

where L is the crystal length and b is confocal parameter expressed as

$$b = \frac{2\pi w^2}{\lambda} \tag{2.50}$$

Here w and λ are the beam waist radius and wavelength of the corresponding wave, respectively. For a given focusing parameter of the pump laser, we need to design an OPO cavity with the same focusing parameter in the resonant signal wave according to ABCD matrix analysis of Gaussian beams. The details of the relevant theory and

calculation have been described in [68-70]. Here, we show an example of a linear cavity design in Figure 2.9. We assume a pump wavelength of 1064 nm and a signal wavelength of 1550 nm for a linear cavity OPO. If the pump beam is focused at the center of a 30-mm-long MgO-doped PPLN (MgO:PPLN) crystal with a beam waist radius of w_p=180 μm, we need to obtain a signal beam waist radius of w_s=216 μm from the cavity design to achieve mode matching condition according to equation (2.50). By using a pair of curved mirrors with a radius of curvature of 200 mm, the desired signal beam waist radius can be achieved with a physical cavity length of 150 mm, as shown in Figure 2.9.

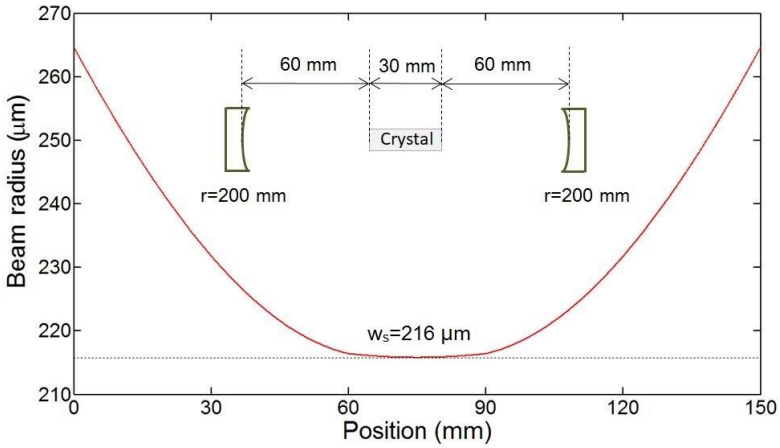

Figure 2.9. Example of variation of the signal beam radius along the cavity axis. Inset: The corresponding cavity configuration and parameters.

As nanosecond OPOs usually operate with relatively strong parametric gain, they can still work efficiently even away from perfect mode matching condition, as long as the resonant wave has sufficient number of round trips in the cavity. Therefore, plane-mirror cavities can be also adopted for nanosecond OPOs. Such cavities are not ideally stable for Gaussian beams. However, under a loose focusing condition, where the confocal parameter is large enough compared to the cavity length, a well-aligned

plane-mirror cavity can still provide enough collinear oscillation of the resonant wave in a nanosecond OPO. In this case, we will be able to use a compact cavity, as short as possible, without considering the mode-matching issue. We then pump the OPO with higher power for output scaling, as a loose focusing condition can reduce the pump to under the crystal damage threshold.

2.8.3 Nonlinear crystals

Nonlinear crystals are the core component in OPOs and other frequency conversion devices. The most basic requirement for a nonlinear crystal is its transparency at pump, signal and idler wavelengths. Low crystal transparency for the involved three waves in an OPO can lead to strong absorption and thermal effects, thus the OPO won't be able to operate efficiently. The damage threshold of nonlinear crystals determines the upper limit of the pump intensity. For birefringent phase-matched crystals, we also need to calculate the crystal cut angle corresponding to the desired phase-matching and the longest effective interaction crystal length limited by spatial walk-off. Besides, crystal quality, available crystal size, and thermal conductivity also need to be taken into consideration. Another important parameter of the crystal is the nonlinear *figure-of-merit* (*FOM*), defined as

$$FOM = \frac{d_{eff}}{\sqrt{n_p n_s n_i}} \tag{2.51}$$

This parameter appeared in the expression of the gain factor, Γ, in equation (2.45). It describes the total effectiveness of a nonlinear crystal for a frequency conversion process. Figure 2.10 shows a comparison of FOMs of various common nonlinear crystals across their transparency range.

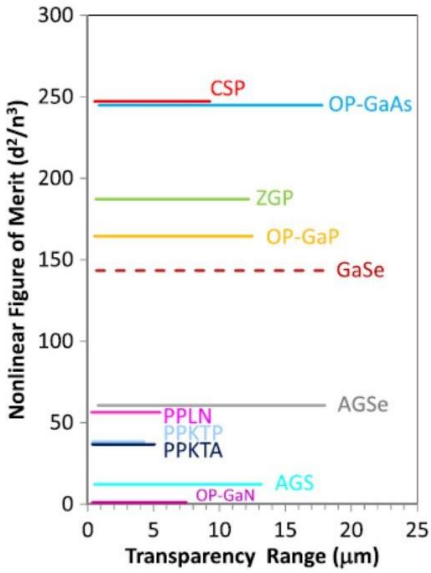

Figure 2.10. A comparison of FOMs of various common nonlinear crystals across their transparency range [71].

2.9 Orientation-patterned gallium phosphide

Orientation-patterned semiconductor materials are gradually becoming promising next-generation QPM nonlinear crystals. The first realization of QPM semiconductor crystals was orientation-patterned gallium arsenide (OP-GaAs), which has shown its capability for efficient long-wave infrared generation [72-77]. However, practical OP-GaAs parametric down-conversion devices usually necessitate pump wavelengths beyond ~1.9 μm to avoid severe two-photon absorption. Therefore, new semiconductor materials suitable for widely available 1 μm and 1.5 μm pump lasers are important to be discovered. Orientation-patterned gallium phosphide (OP-GaP), an analogue of OP-GaAs, but with extended short-wavelength transparency edge, was recently developed for this purpose.

OP-GaP crystals used in this thesis were grown at *BAE Systems*, USA. The

orientation-inverted layer of OP-GaP is first grown by polar-on-nonpolar molecular beam epitaxy (MBE) on the (100) plane of GaP where a non-polar Si layer is deposited. Then, periodically inverted structure with the desired grating period can be generated by photolithography and etching. This template is then regrown by MBE method and becomes an orientation-patterned film with a few μm thickness. Finally, the thin film is further grown to increase the thickness of the QPM layer using hydride vapor phase epitaxial (HVPE) process [78, 79].

A side view of a grown OP-GaP crystal is illustrated in Figure 2.11. The periodically inverted orientation is designed along $[01\bar{1}]$ axis of the crystal, and all the beams are designed to propagating along $[0\bar{1}\bar{1}]$ axis. Some basic properties of gallium phosphide are summarized in Table 2.1.

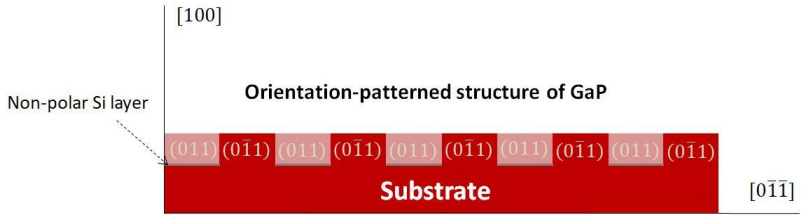

Figure 2.11. Illustration of the orientation-patterned structure in OP-GaP.

Table 2.1. Basic properties of gallium phosphide [80, 81].

Transparency range [μm]	~0.57-12
Crystal structure	Zinc Blende
Nonlinear coefficient [pm/V]	d_{14}=70.6 pm/V
Bandgap [eV]	2.26
Melting Point [°C]	1477
Thermal conductivity [W/mK]	110
Thermal Expansion Coefficient [$°C^{-1}$]	4.65×10^{-6}
Knoop hardness [kg/mm^2]	850

Apart from the above properties, the refractive index is also an important parameter. Refractive index is not only contributing to the nonlinear FOM based on equation (2.51), but also important in the calculation of QPM condition for OP-GaP. Temperature- and wavelength-dependent refractive index for a particular transparent medium can be usually calculated using empirical Sellmeier equations. Below, we show a new Sellmeier equation for OP-GaP. It comes from a recent experimental investigation and is given by [82]

$$n(T) = \sqrt{A + \frac{B}{\lambda^2 - C} + \frac{D}{\lambda^2 - E}} \tag{2.52}$$

where the coefficients from *A* to *E* are given in Table 2.2.

Table 2.2. Coefficients for OP-GaP Sellmeier equation.

A	$10.926 + 7.0787 \times 10^{-4}T + 1.8594 \times 10^{-7}T^2$
B	$0.53718 + 5.8035 \times 10^{-5}T + 1.9819 \times 10^{-7}T^2$
C	0.0911014
D	$1504 + 0.25935T - 0.00023326T^2$
E	758.048

Here the crystal temperature T is in Kelvin and wavelength λ is in μm. These coefficients in Table 2.2 are valid for a wavelength range of 0.7-12.5 μm and a temperature range of 78-450 K. Using this Sellmeier equation, we can determine the refractive index of OP-GaP at any particular wavelength and temperature, and further calculate the wavelength tuning curves.

The QPM condition of parametric down-conversion given by equation (2.41) can be further simplified to

$$\frac{n_s(T)}{\lambda_s}+\frac{n_i(T)}{\lambda_i}-\frac{n_p(T)}{\lambda_p}=\frac{1}{\Lambda} \tag{2.53}$$

where *s*, *i* and *p* represent signal, idler and pump, respectively. Besides, we know the photon energy conservation in down-conversion process can be expressed as

$$\frac{1}{\lambda_s}+\frac{1}{\lambda_i}=\frac{1}{\lambda_p} \tag{2.54}$$

Thus, we can eliminate the term $\frac{1}{\lambda_i}$ by substituting equation (2.54) to (2.53), and obtain

$$\frac{n_s(T)}{\lambda_s}+\frac{n_i(T)}{\lambda_p}-\frac{n_i(T)}{\lambda_s}-\frac{n_p(T)}{\lambda_p}=\frac{1}{\Lambda} \tag{2.55}$$

For a specific process, we know the pump wavelength, λ_p, and the grating period, Λ, of OP-GaP. Thus, equation (2.55) reveals the one-to-one correspondence between the crystal temperature and the signal wavelength. By writing a computer program based on equation (2.55), together with the Sellmeier equation of OP-GaP (2.52), we are able to calculate the temperature-dependent wavelength tuning curves for OP-GaP. This calculation can be further applied to other QPM crystals.

Since allowing 1-μm-laser pumping is the most important advantage of OP-GaP compared to other non-oxide infrared crystals, here we show an example of temperature-dependent wavelength tuning curves of OP-GaP when pumping at 1.064 μm. As can be seen in Figure 2.12, the longer grating period of OP-GaP enables longer mid-IR wavelength generation in the idler. By scanning the crystal temperature from room temperature to 200°C and using different grating periods between Λ=18 μm and Λ=28 μm, the idler generated from OP-GaP can be tuned across 4-8 μm, and can be extended even deeper into the mid-IR region.

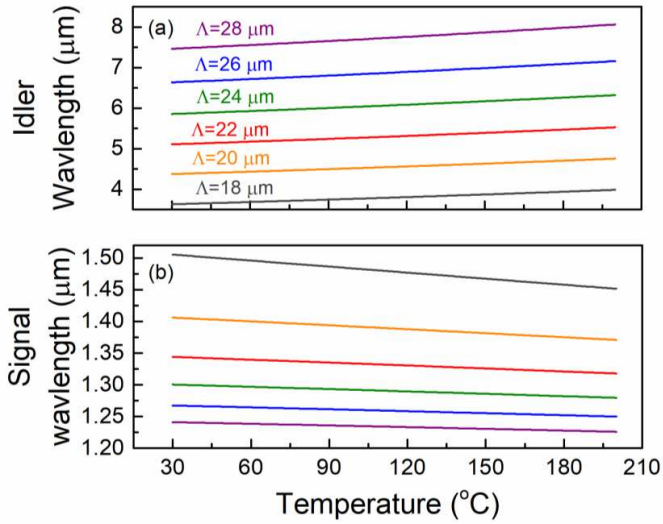

Figure 2.12. Simulation of wavelength tuning curves of OP-GaP for a pump wavelength of 1.064 μm.

Chapter 3

Optical parametric generator based on OP-GaP

3.1 Motivation

Mid-infrared (Mid-IR) coherent sources based on optical parametric down-conversion are of great significance for a variety of applications, such as molecular spectroscopy [83], up-conversion imaging [84], and as a pump source for other nonlinear processes [85]. Oxide-based nonlinear crystals, and especially their quasi-phase matched (QPM) counterparts, such as MgO-doped periodically-poled $LiNbO_3$ (MgO:PPLN), stoichiometric $LiTaO_3$ (MgO:sPPLT), and $KTiOPO_4$ (PPKTP), have enabled broadband mid-IR coverage up to ~4 μm, in all time scales from continuous-wave (cw) to femtosecond domain [86–89]. However, the onset of multiphonon absorption in these nonlinear crystals has been a fundamental barrier to reach spectral regions into the deep mid-IR. Non-oxide-based nonlinear materials with extended transparency in the mid-IR, such as $ZnGeP_2$ (ZGP) and orientation-patterned GaAs (OP-GaAs), offer potential for the development of parametric sources beyond 4 μm. However, their low bandgap requires pumping above 2 μm to avoid two-photon absorption. The more recently developed nonlinear crystal, $CdSiP_2$ (CSP), is an important new addition to the family of birefringent

materials for parametric down-conversion into the deep mid-IR. Its high optical nonlinearity, noncritical phase-matching (NCPM) capability, and a wide transparency range extending down to below ~1 μm enable the deployment of the widely available Nd-based solid-state or Yb-based fiber lasers as a pump source for deep mid-IR wavelength generation up to ~7 μm [90]. On the other hand, the new semiconductor nonlinear material, orientation-patterned GaP (OP-GaP), can be considered as the QPM analog of CSP, and a promising alternative for deep mid-IR generation. As a QPM material, OP-GaP offers unique flexibility for tunable wavelength generation into the deep mid-IR using grating engineering under NCPM with no spatial walk-off. Moreover, unlike ZGP and OP-GaAs, it has significantly lower two-photon absorption, allowing the direct use of well-established laser pump sources at ~1 μm for parametric down-conversion. Together with a wide transparency up to ~12 μm, large optical nonlinearity (d_{14}=70.6 pm/V), and high thermal conductivity (110 W/mK) [71], these characteristics make OP-GaP a highly attractive alternative for the development of practical parametric sources throughout the mid- to deep-IR.

Earlier reports on nanosecond optical parametric sources based on OP-GaP include a nanosecond doubly resonant optical parametric oscillator (DRO) pumped at 1064 nm, generating 4 mW of idler at 4624 nm and 15 mW of signal at 1324 nm at 10 kHz [91], as well as a nanosecond DRO pumped at 2090 nm, operating at an idler wavelength of 5100 nm and a signal wavelength of 3540 nm, with a total signal plus idler average output power of 350 mW at 20 kHz repetition rate [92]. We also recently demonstrated a tunable difference-frequency-generation (DFG) source based on OP-GaP by mixing the input pulses from a nanosecond Nd:YAG pump laser and the signal from an optical parametric oscillator (OPO) based on a 40-mm-long MgO:PPLN crystal, resulting in the generation of tunable mid-IR radiation over 2548-2781 nm with ~14 mW average output power at 2719 nm and 80 kHz repetition

rate [93]. In the cw regime, single-pass DFG based on 16.5-mm-long OP-GaP crystal was reported, providing up to 150 mW at 3400 nm for an input pump power of 47 W at 1064 nm together with 24W of signal power at 1550 nm [94]. Recently, using a 24.6 mm-long OP-GaP crystal, a cw DFG power of 65 μW was generated at 5850 nm for a pump power of 10 W at 1064 nm and a signal power of 40 mW at 1301 nm [95]. In this chapter, we report what we believe to be the first optical parametric generator (OPG) based on OP-GaP. The OPG, pumped by a Q-switched Nd:YAG laser at 1064 nm, can be temperature tuned across 1721-1850 nm in the signal and 2504-2787 nm in the idler, providing up to ~18 mW of the total average output power at 25 kHz repetition rate, with ~5 mW of the idler at 2670 nm. We have also performed systematic measurements of transmission at 1064 nm for polarization along the [100] axis in the OP-GaP sample, revealing a dramatic decrease in pump transmission with increase in crystal temperature.

3.2 Experimental setup

The schematic of the experimental setup for the OPG is shown in Figure 3.1. The pump laser is a linearly polarized, Q-switched Nd:YAG laser (*Bright Solutions, Sol*) delivering up to ~30 W of average power with a tunable repetition rate ranging from 20 kHz to 100 kHz. It operates at a central wavelength of 1064 nm with a full width at half-maximum (FWHM) bandwidth of <0.5 nm and exhibits spectral jitter of ~1 nm over 30 s. For pumping the OPG, we chose a fixed repetition rate of 25 kHz in order to obtain higher peak power for increased nonlinear conversion efficiency. The pump power is controlled by the combination of a half-wave plate and a polarizing beam-splitter (PBS). The polarization of the pump is initially set along [100] for OP-GaP, as described in [94], and further adjusted using a second half-wave plate to

achieve maximum efficiency for parametric generation in the crystal. The OP-GaP crystal is 40-mm-long, 6-mm-wide, and 1.7-mm-thick, with a single grating period of Λ=15.5 μm, and is mounted on an oven providing temperature control from room temperature to 200°C, with an accuracy of 0.1°C. The end-faces of the crystal are antireflection (AR)-coated (R<1%) for 1064 nm and 1500-1900 nm, with high transmission (R<20%) over 2500-2700 nm. The pump beam is focused to a waist radius of $w_0 \sim$ 89 μm in the QPM layer of the crystal, corresponding to a focusing parameter of $\xi \sim$ 0.28. A long-pass filter transmitting above 1.65 μm is used to separate the total output power (signal plus idler) from the pump. Another long-pass filter transmitting above 2.4 μm is used to extract only the idler power.

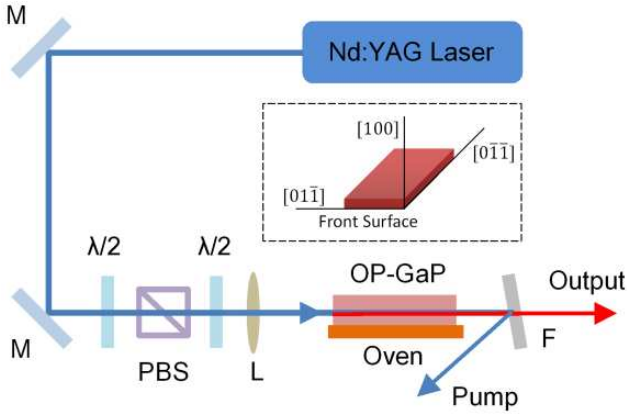

Figure 3.1. Schematic of the experimental setup for the OP-GaP OPG. λ/2, half-wave plate; PBS, polarizing beam-splitter; L, lens; F, filter.

3.3 Results and discussion

3.3.1 Temperature tuning characteristics

Initially, we investigated the temperature tuning characteristics of the OPG. By changing the temperature of the OP-GaP crystal over 50°C–180°C, we were able to

tune the generated signal across 1721-1850 nm, together with the corresponding idler across 2504–2787 nm, resulting in a total (signal plus idler) tuning over 412 nm. The results are shown in Figure 3.2, where the solid circles represent the experimentally measured signal wavelengths, while the hollow circles are the corresponding idler wavelengths estimated from energy conservation. The solid and dashed curves are the theoretical signal and idler wavelengths calculated using the relevant Sellmeier equations in [91] and [82]. The temperature tuning curves indicate a wavelength tuning rate of ~1 nm/°C for the signal and ~2.2 nm/°C for the idler. Also shown in the inset of Figure 3.2 are the signal spectra across the OPG tuning range, measured using a spectrometer with a low resolution of ~11 nm.

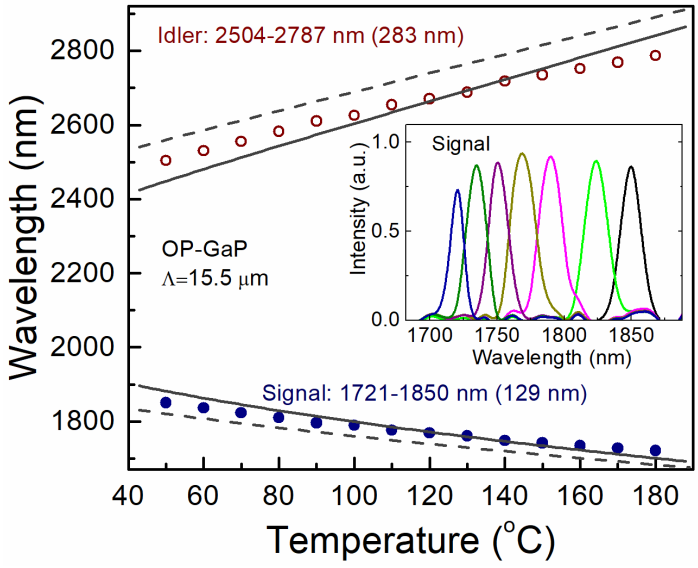

Figure 3.2. Wavelength tuning range of the OP-GaP OPG for a grating period of Λ=15.5 μm. Circles represent experimental measurements, and the solid and dashed lines represent theoretical calculation. Inset: spectrum of the signal across tuning range.

3.3.2 Power across tuning range and pump transmission

The signal, idler, and total output powers, and the corresponding pulse energies

across tuning range of the OPG as a function of crystal temperature are shown in Figure 3.3. As can be seen, the output power from the OPG follows a bell-shaped variation as a function of temperature. For a fixed pump power of 2 W (corresponding to a pulse energy of 80 μJ), the total OPG output power increases from 5.9 mW (0.24 μJ) to 18 mW (0.72 μJ) as the temperature of the OP-GaP crystal is increased from 50°C to 110°C. However, further increasing the temperature up to 160°C results in the decline in output power down to 8.1 mW (0.32 μJ). The recorded maximum total OPG output power of 18 mW (0.72 μJ) at 110°C corresponds to a measured idler power of 5 mW (0.2 μJ) at 2654 nm and an estimated signal power of 13 mW (0.52 μJ) at 1776 nm. The filtered idler power varies from 0.2 mW (8 nJ) to 2 mW (80 nJ) with a maximum of 5.1 mW (0.204 μJ) at 120°C, while the estimated signal power follows the idler, varying from 5.8 mW (0.23 μJ) to 6.1 mW (0.24 μJ), as the temperature of the OP-GaP crystal is increased from 50°C to 160°C. Considering the measured transmission of the pump at 110°C, the generated 18 mW of output power from OPG represents a single-pass conversion efficiency of 3.7% and photon conversion efficiency of 4.5% and 2.6% for the signal and idler, respectively. While varying the temperature of the OP-GaP crystal, we noticed that the position of the transmitted pump beam through the sample, monitored using a scanning beam profiler, significantly shifted vertically, leading to the deviation of the pump beam from the thin QPM region. We attribute the drop in output power on either side of the maximum to crystal absorption at the pump, signal, and/or idler wavelengths, as well as the observed deviation in the pump beam propagation direction out of the QPM grating. As such, we further studied the transmission characteristics of the crystal at the pump wavelength of 1064 nm for polarization set along the [100] direction.

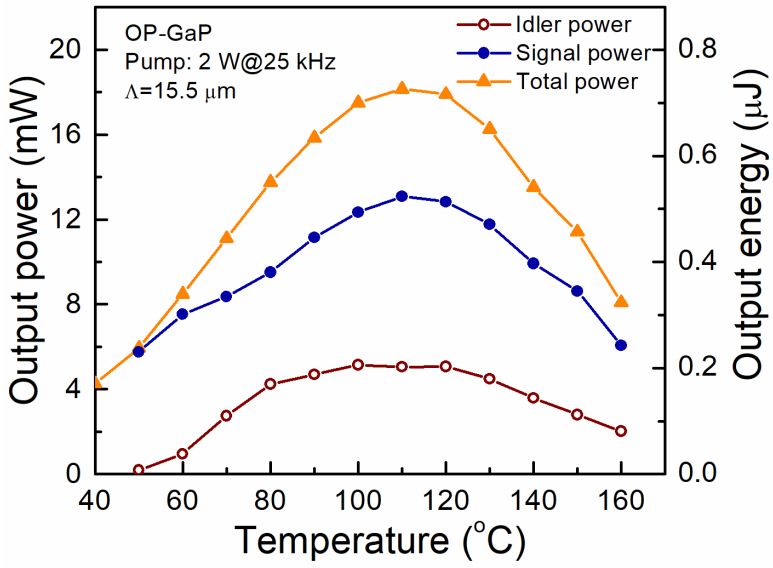

Figure 3.3. Power and energy across the OPG tuning range as a function of the OP-GaP crystal temperature.

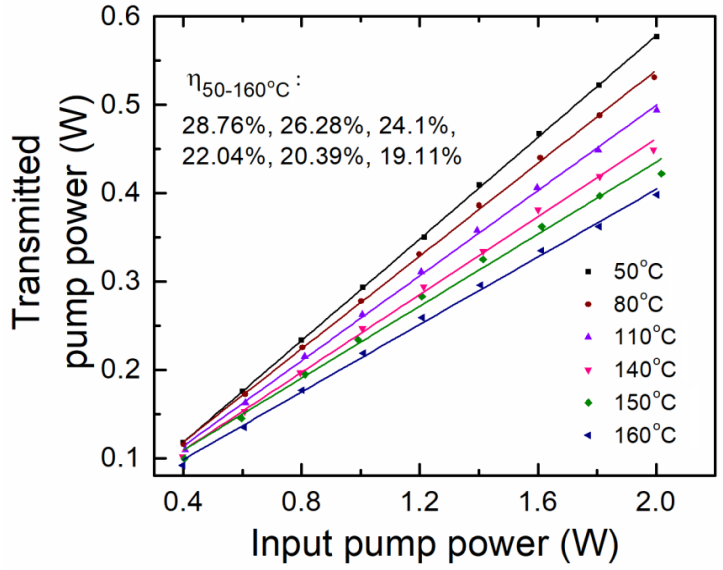

Figure 3.4. Transmitted pump power versus input pump power at different temperatures.

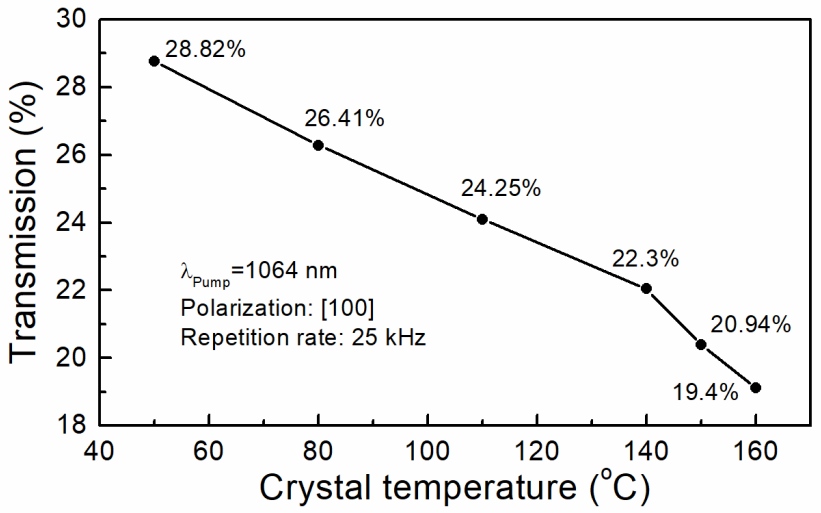

Figure 3.5. Variation of the averaged transmission of the OP-GaP crystal at 1064 nm as a function of temperature.

To obtain reliable data, we measured the transmitted pump power through the OP-GaP crystal as a function of the input pump power varying from 0.4 W (16 μJ) to 2 W (80 μJ), at six different temperatures, as shown in Figure 3.4. In a separate measurement, we also estimated the damage threshold of the OP-GaP crystal at 1064 nm to be ~0.8 J/cm^2 when operating close to room temperature. In order to avoid any damage to the crystal, we thus limited the average pump power in our experiment to 2 W at 25 kHz, corresponding to an energy fluence of 0.32 J/cm^2, well below the damage threshold of the OP-GaP sample. As the photon conversion efficiency in the OPG is very low (<5%), we consider the entire output power from the crystal measured without any filters as the transmitted pump power, and further treat the slope efficiency as averaged transmission at every temperature point. As can be seen in Figure 3.5, the pump transmission is unexpectedly low, amounting to only 28.8% at a crystal temperature of 50°C, and further decreasing down to 19.4% at 160°C. We also attempted to measure the transmission at 170°C. However, we observed the

sudden appearance of a damage spot on the surface of the crystal at an input pump power of 2 W (80 μJ) at 170°C, implying the OP-GaP crystal has a lower damage threshold at higher temperatures due to the stronger pump absorption. To the best of our knowledge, this is the first experimental investigation of temperature-dependent optical transmission in OP-GaP.

3.3.3 Power scaling and OPG threshold

The power scaling characteristics of the generated signal and idler from the OPG measured at a repetition rate of 25 kHz and an OP-GaP crystal temperature of 120°C are presented in Figure 3.6(a). For a maximum pump power of 2 W (80 μJ), corresponding to a pump energy fluence of 0.32 J/cm^2 in the OP-GaP crystal, we were able to generate 12.6 mW (0.5 μJ) of signal power at 1769 nm together with 5.2 mW (0.21 μJ) of idler power at 2670 nm. The slope efficiencies are estimated to be 1.23% and 0.51% for the signal and idler, respectively. It is to be noted that the data presented here are not corrected for the ~20% AR-coating loss of the OP-GaP crystal in the idler wavelength range. Further, we explored the OPG threshold at different repetition rates varying from 25 kHz to 90 kHz. The threshold values were measured at a fixed OP-GaP crystal temperature of 120°C using a high-sensitivity visible spectrometer (*Ocean Optics*, *HR4000*). The criterion for OPG threshold measurement was the visual observation of red light resulting from parasitic sum-frequency-generation of the pump and generated signal, which suddenly appeared as the pump power was gradually increased. The OPG threshold as a function of the pump pulse repetition rate is shown in Figure 3.6(b). As can be seen, the threshold increases from 0.57 W (23 μJ) at 25 kHz to 4.67 W (52 μJ) at 90 kHz, due to the drop in the peak pump power at higher repetition rates, as expected.

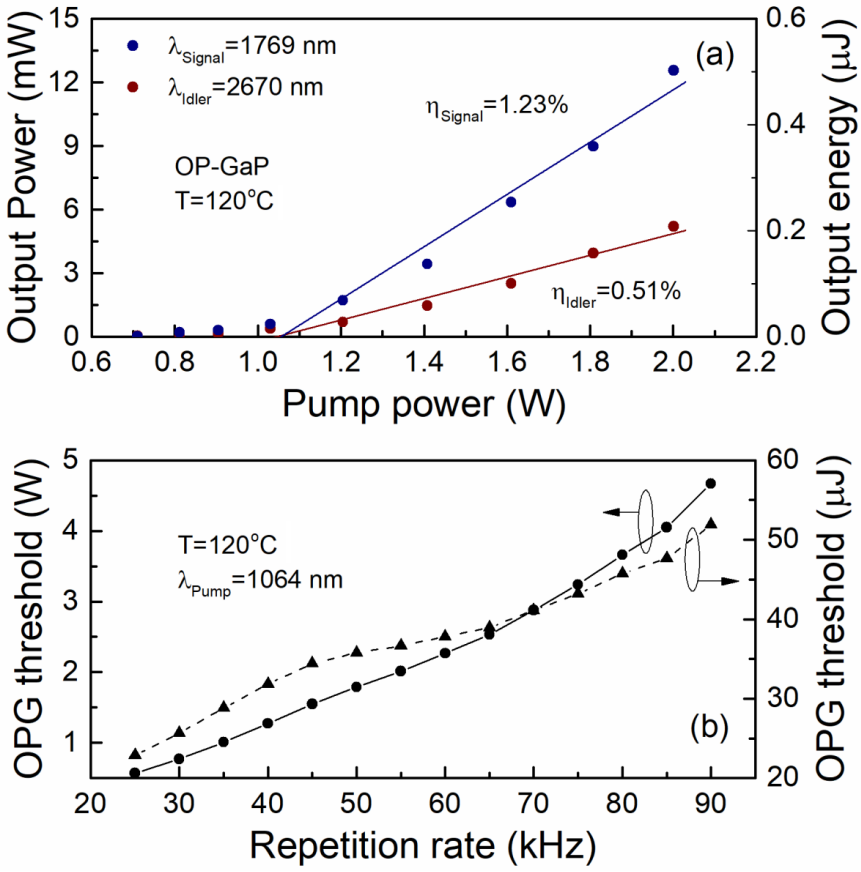

Figure 3.6. (a) Signal and idler power scaling as a function of the pump power. (b) Dependence of the OPG threshold on the pump laser repetition rate at a crystal temperature of 120°C.

3.3.4 Temporal pulse profile

We measured the pulse duration of the pump and the generated signal from the OPG using an InGaAs detector with a bandwidth of 5 GHz and a digital oscilloscope with a bandwidth of 3.5 GHz. As shown in Figure 3.7(a) and (b), the typical FWHM pulse durations are recorded to be 9 ns for the pump at 1064 nm and 5.9 ns for the signal at a wavelength of 1769 nm, at 25 kHz repetition rate. It is also to be noted that closer inspection of the two temporal profiles reveals the beat frequency between

different longitudinal modes in both pump and signal pulses.

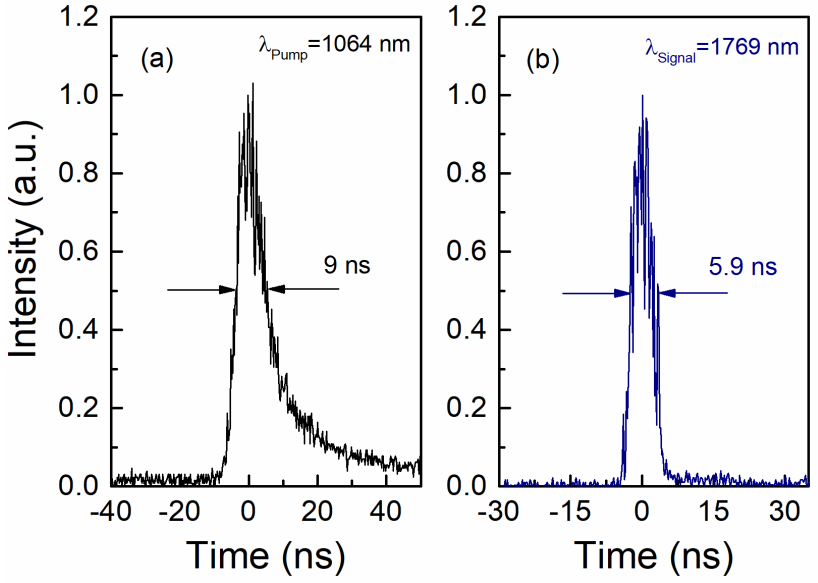

Figure 3.7. Measured pulse shapes of (a) pump, and (b) signal for the OP-GaP OPG at 25 kHz repetition rate.

3.3.5 Power stability

Further, we investigated the long-term stability of the output power from the OPG. The power stability measurement was performed at an OP-GaP crystal temperature of 120°C, corresponding to the signal and idler wavelengths of 1769 nm and 2670 nm, respectively. The results are shown in Figure 3.8(a)-(c). The total output power from OPG exhibits a passive stability of 0.87% rms with a mean value of 18.15 mW over 1 hour, and the pure idler power exhibits a similar passive stability of 0.89% rms with a mean value of 5.16 mW. As a comparison, we also measured the input pump power stability which was recorded to be 0.14% rms with a mean value of 2.07 W over the same period.

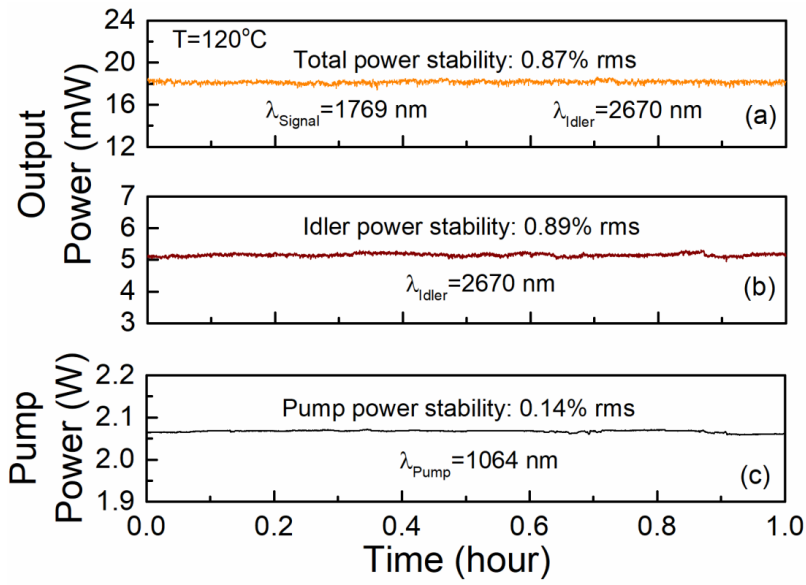

Figure 3.8. Long-term stability of (a) total output power, (b) idler power, and (c) pump power over a period of 1 hour.

3.4 Conclusions

In conclusion, we demonstrated what is, to our knowledge, the first OPG source based on OP-GaP. Using a nanosecond pulsed Nd:YAG laser at 25 kHz repetition rate as the pump source and a 40-mm-long OP-GaP crystal with a single grating period of Λ=15.5 μm, we have achieved tunable single-pass parametric generation across the near- and mid-IR wavelength range of 1721-1850 nm in the signal and 2504-2787 nm in the idler, in close agreement with the theoretical calculation. The OPG can provide a total average output power of up to ~18 mW (0.72 μJ), with ~5 mW (0.2 μJ) of idler power at 2670 nm, for a maximum pump power of 2W (80 μJ), with good passive power stability of 0.87% rms over 1 hour. The OPG output signal pulses have typical duration of 5.9 ns for input pump pulses of 9 ns. In addition, we have performed temperature-dependent transmission measurements for pump polarization

along the [100] direction, revealing decreasing transmission of the OP-GaP crystal with increasing temperature. With further progress in the growth of OP-GaP crystals of higher optical quality and reduced transmission loss, substantial improvements in OPG efficiency, output power, and potential for power scaling are expected, paving the way for the development of practical parametric sources throughout the mid- to deep-IR, using widely available solid-state and fiber laser pump sources near 1 μm.

Chapter 4

Singly-resonant pulsed optical parametric oscillator based on OP-GaP

4.1 Motivation

Optical parametric oscillators (OPOs) are now firmly established as viable sources of widely tunable coherent radiation from the ultraviolet to mid-infrared (mid-IR), operating in all time-scales from the continuous-wave to few-cycle ultrashort pulses [96-98]. They represent attractive sources for a variety of applications including supercontinuum generation, trace gas sensing, and study of structured beams [99-101]. Based on quasi-phase-matched (QPM) nonlinear crystals, in particular MgO-doped periodically-poled $LiNbO_3$ (MgO:PPLN) and stoichiometric $LiTaO_3$ (MgO:sPPLT), OPOs have been extensively developed and investigated in recent years in different device configurations and time-scales [102,103]. However, practical operation of OPOs at wavelengths beyond ~4 μm is precluded by multiphonon absorption in such oxide-based crystals. Hence, access to longer wavelengths requires non-oxide nonlinear materials with extended transparency in the mid-IR. Among these, $ZnGeP_2$, orientation-patterned GaAs, and more recently, $CdSiP_2$, have been successfully exploited for the development of mid-IR OPOs in different time-scales at wavelengths beyond ~4 μm [71,90]. Another most recently

introduced non-oxide alternative is the QPM semiconductor crystal, orientation-patterned gallium phosphide (OP-GaP). It is a promising candidate for mid-IR generation, owing to a large nonlinearity (d_{14}=70.6 pm/V) [71], flexible QPM design allowing convenient temperature and grating tuning, and very importantly, a wide infrared transparency extending from as low as ~1 μm up to ~12 μm [104], which enables direct OPO pumping using well-established, widely available, and cost-effective solid-state and fiber lasers at ~1.06 μm.

The first nanosecond frequency conversion source based on OP-GaP has been reported to be a pulsed OPO pumped by a Ho:YAG laser at 2090 nm, generating 350 mW of signal plus idler at 3540 nm and 5100 nm [92]. A pulsed OPO pumped by a Nd:YVO_4 laser at 1064 nm was also reported, providing tunable signal and idler across 1385-1361 nm and 4591-4876 nm, respectively, with 15 mW at 1382 nm and 4 mW at 4624 nm [91]. To achieve successful operation, both OPOs were configured as doubly-resonant oscillators (DROs), characterized by low pump power threshold. We also previously reported a pulsed nanosecond mid-IR source based on difference-frequency-generation (DFG) in OP-GaP, providing tunable output across 2548-2781 nm, with highest average power of 14 mW at 2719 nm and 80 kHz repetition rate [93]. We further demonstrated optical parametric generation (OPG) in OP-GaP pumped by a nanosecond Nd:YAG laser at 25 kHz, resulting in a highest total power of ~18 mW and a wavelength tuning range of 1721-1850 nm for signal and 2504-2787 nm for idler [105]. In this chapter, we describe what we believe to be the first nanosecond pulsed OPO in singly-resonant oscillator (SRO) configuration based on OP-GaP. Pumped by a pulsed Nd:YAG laser at 1064 nm and 50 kHz repetition rate, the OPO delivers signal and idler output across 1.6-1.7 μm and 2.8-3.1 μm, respectively, through temperature tuning, using a single grating period. Wavelength shifts of the signal and idler in temperature tuning curves are observed at

different pump power levels, revealing that the OP-GaP crystal suffers from thermal effect due to absorption. We achieve a maximum OPO idler output power of ~20 mW at 2966 nm at 50 kHz pulse repetition rate with good power stability.

4.2 Experimental setup

The schematic of the experimental setup for the OP-GaP OPO is shown in Figure 4.1. The pump laser is a linearly polarized, Q-switched Nd:YAG laser at 1064 nm, which has been described in chapter 3. Here, we use a repetition rate of 50 kHz resulting in a full-width at half-maximum (FWHM) pulse duration of ~13 ns, providing a modest peak power for parametric gain, while suppressing excess single-pass OPG in the oscillator. The pump beam propagates through a half-wave plate and a polarizing beam-splitter (PBS) for power attenuation, with a second half-wave plate providing polarization control for optimum nonlinear efficiency in the cubic OP-GaP crystal, according to our earlier polarization studies [106]. The OPO is formed by two plane mirrors, M_1 and M_2, with a minimum separation of 78 mm, resulting in a compact cavity limited in length by the physical dimension of the oven housing the OP-GaP crystal. The cavity length allows ~12 round-trips of the signal over the ~13 ns pump pulse duration. The mirrors are highly transmitting for the pump (T>90% at 1064 nm) and idler (T>80% over 2.2-4.0 μm), while highly reflecting for the signal (R>99% over 1.3-1.9 μm), thus ensuring SRO configuration for the signal wave. The OP-GaP sample is 40-mm-long, 6-mm-wide, 1.7-mm-thick, with a single grating period of Λ=16 μm. The end-faces of the crystal are AR-coated (R<5%) at 1064 nm and 1500-1900 nm, with high transmission (T>75%) over 2700-3100 nm. Using a lens of focal length, f=250 mm, the pump beam is focused to a waist radius of w_{0p}~104 μm inside the grating layer of the OP-GaP crystal, resulting

in a focusing parameter ξ_p~0.21. An infrared long-pass filter with a cut-on wavelength of 2.4 μm is used to extract the idler power for measurement. A photograph of the OP-GaP OPO is shown in Figure 4.2.

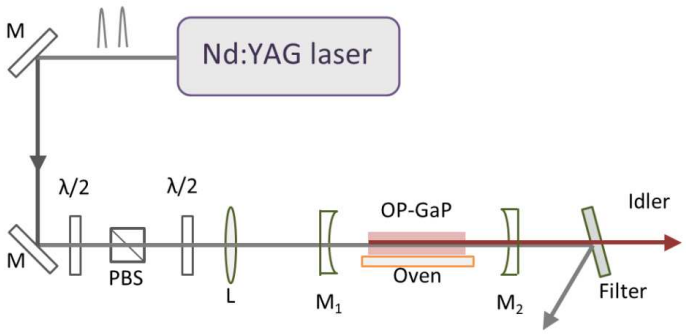

Figure 4.1. Schematic of experimental setup for the OP-GaP OPO. λ/2, half-wave plate; PBS, polarizing beam-splitter; L, lens.

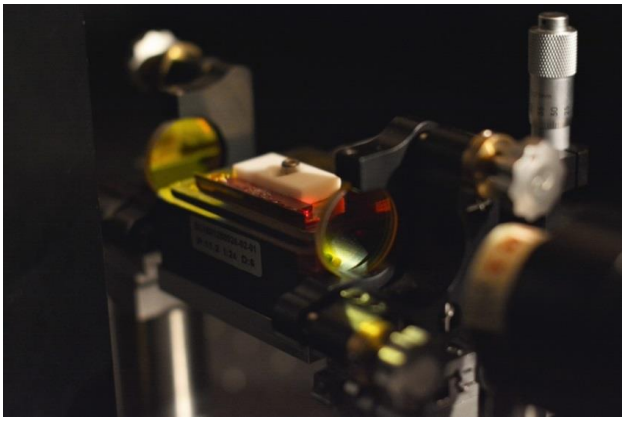

Figure 4.2. Photograph of the OP-GaP OPO with non-phase-matched SFG in the visible.

4.3 Results and discussion

4.3.1 Temperature tuning and thermal effects

Initially, we investigated the temperature tuning characteristics of the OP-GaP

OPO. By monitoring the non-phase-matched sum-frequency-generation (SFG) between the pump and signal using a sensitive visible spectrometer with a resolution of 0.5 nm (*Ocean Optics, HR4000*), we were able to estimate the signal and idler wavelengths. Using an average pump power of 4.2 W at 50 kHz repetition rate, by varying the temperature of the OP-GaP crystal from 50ºC to 180ºC in steps of 10ºC, we were able to tune the OPO across 1612-1700 nm in the signal and 2845-3130 nm in the idler, as shown in Figure 4.3. We then reduced the pump pulse repetition rate to 25 kHz, thus lowering the pump average power to 1.2 W to minimize any thermal effects in the OP-GaP crystal, and recorded the non-phase-matched SFG output wavelength at each temperature. Under this condition, the signal could be tuned across 1620-1712 nm, with the idler tunable over 2812-3101 nm, as also shown in Figure 4.3. As evident, there is significant difference in the tuning data at the two different pump powers and repetition rates. Both sets of measurements result in a wavelength tuning rate of about 0.7 nm/ºC for the signal and 2.2 nm/ºC for the idler. However, the signal wavelengths for the pump power of 4.2 W are 8-12 nm shorter than those for the pump power of 1.2 W at each temperature across the tuning range. Given the signal tuning rate of 0.7 nm/ºC, this means that the internal temperature of the OP-GaP crystal pumped at 4.2 W is about 11-17ºC higher than when pumped at 1.2 W, indicative of significant thermal effects in the OP-GaP crystal, which is attributed to strong pump absorption, as also observed in the OPG experiment described in Chapter 3.

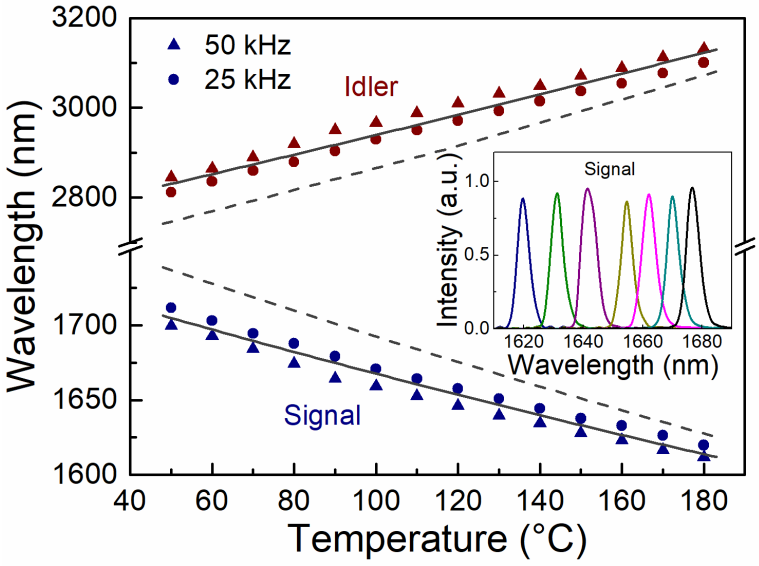

Figure 4.3. Wavelength tuning range of the OP-GaP OPO for a grating period of 16 μm. Triangles and circles correspond to 50 kHz and 25 kHz pump pulse repetition rate, respectively. Solid and dashed lines are theoretical calculation. Inset: Spectrum of the signal across the tuning range.

The dashed and solid lines close to the experimental data in Figure 4.3 represent theoretical simulations of temperature tuning curves based on the Sellmeier equations in [91] and [82]. Also shown in the inset of Figure 4.3 are the signal spectra across the temperature tuning range below 1.7 μm, measured using a near-IR spectrometer based on InGaAs linear array sensors (*Radiantis, SeaWave*) with a ~1 nm resolution, and using an output coupler (T~5% over 1100-1600 nm) in place of M_2 to extract a fraction of signal wave out of the OPO cavity. The signal spectra have FWHM bandwidths of 4.5-6 nm across the tuning range.

4.3.2 Power across tuning range

The idler average power and the corresponding pulse energy of the OP-GaP OPO for a pump power of 4.51 W (90.2 μJ) at 50 kHz across the tuning range are shown in

Figure 4.4. The idler power varies from 15.1 mW (0.3 μJ) at 2845 nm to 13 mW (0.26 μJ) at 3089 nm, as the temperature of the crystal is increased from 50ºC to 160ºC, with the highest power of 17.5 mW (0.35 μJ) recorded at 2919 nm. During the temperature scan of the OP-GaP crystal, we observed significant displacement of the transmitted pump beam in the vertical direction, consistent with the observation in the OPG experiment. This temperature-dependent beam shift in OP-GaP can lead to a deviation of the pump beam from the thin QPM layer. Thus, in order to maintain OPO resonance and ensure maximum idler power over the widest temperature range, we made small adjustments to the height of the OP-GaP crystal and the cavity alignment at each temperature.

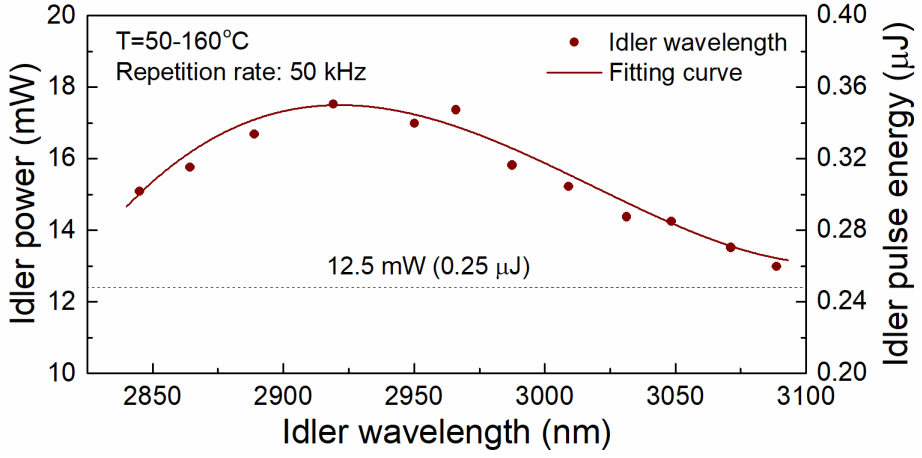

Figure 4.4. Idler average power and pulse energy of the OP-GaP OPO across the tuning range.

4.3.3 Power scaling and pump transmission

We also performed power/energy scaling of the OP-GaP OPO at 50 kHz pump pulse repetition rate and at a crystal temperature of 100ºC, corresponding to an idler wavelength of 2966 nm. The results are shown in Figure 4.5(a), where it can be seen that by increasing the average pump power up to 4.81 W (96.2 μJ), the OPO idler

power can be scaled up to 19.9 mW (0.4 μJ) with a slope efficiency of 1.27%. As a comparison, by removing the OPO output mirror, M_2, we could observe single-pass OPG from the OP-GaP crystal, providing an idler output power up to 2.5 mW (0.05 μJ) for a pump power of 4.76 W (95.2 μJ), at a slope efficiency of 0.15%, as also shown in Figure 4.5(a).

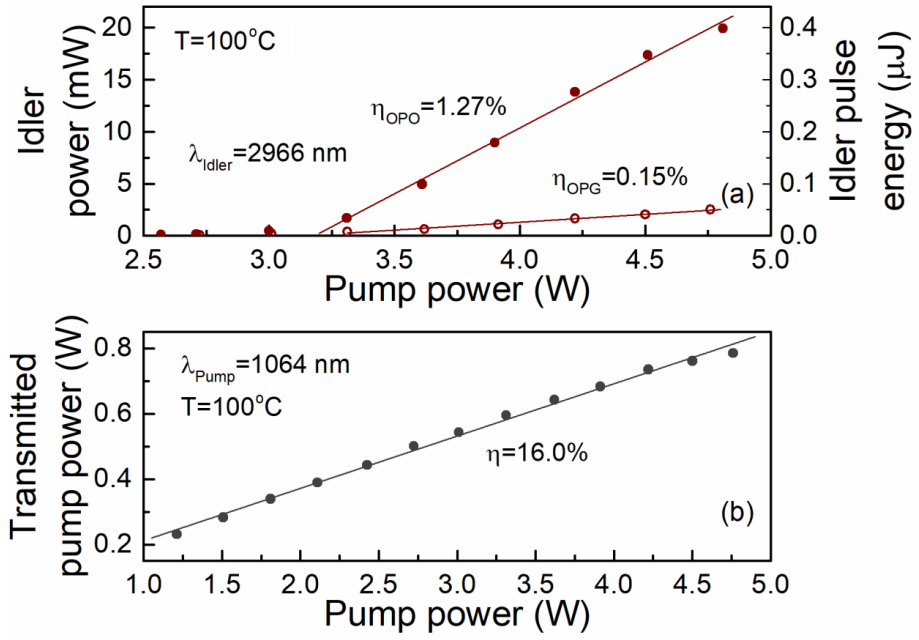

Figure 4.5. (a) Idler power and energy scaling as a function of the pump power in OP-GaP OPO and OPG. (b) Transmitted pump power through the OP-GaP crystal as a function of the input pump power.

We further performed transmission measurements of the OP-GaP sample for the pump at 1064 nm at the same crystal temperature and pulse repetition rate, with the result shown in Figure 4.5(b). When the input pump power is increased from 1.21 W to 4.76 W, the transmitted pump power through the OP-GaP crystal follows an almost linear increase from 0.23 W to 0.785 W at a slope efficiency of 16%, which can be approximated as the average transmission of the OP-GaP grating layer for the pump

laser at 100ºC and 50 kHz pulse repetition rate. Such a low crystal transmission for the pump is the major contribution to the relatively low conversion efficiency of the OPO.

4.3.4 Parasitic light generation and beam profile

With the OPO operating at 50 kHz repetition rate, we were able to observe parasitic red light generated from the OP-GaP crystal. In order to understand the origin of the non-phase-matched nonlinear processes, we measured the spectrum of the parasitic visible light using a sensitive spectrometer and a short-pass filter with a cut-off wavelength of 850 nm (*Thorlabs, FES0850*) at a crystal temperature of 100ºC. As shown in Figure 4.6, there are three spectral lines recorded around 648 nm, 780 nm and 833 nm, representing SFG between the pump and signal, SFG between the pump and idler, and second-harmonic-generation (SHG) of the signal, respectively. By removing the OPO output mirror, M_2, we observed a reduction in the intensity of the SFG spectra while still visible, whereas the SHG of the signal completely disappeared, implying the generation of the SHG of the signal is only due to the enhanced intracavity intensity in the OPO. We also recorded the far-field intensity distribution of the idler at 2966 nm and maximum output power using a pyroelectric camera, with the result shown in the inset of Figure 4.6, indicating a single-peak Gaussian distribution.

4.3.5 Pulse temporal characterization

By replacing the OPO output mirror, M_2, with a signal output coupler (T~5% over 1100-1600 nm), we were also able to extract a fraction of signal power for pulse measurements. Using a fast Si detector (*Thorlabs, DET025A/M*) and a fast InGaAs detector (*Alphalas, UPD-5N-IR2-P*), together with a digital oscilloscope with a

bandwidth of 3.5 GHz, we measured the typical pulse shapes of the transmitted pump and the generated signal simultaneously at 50 kHz repetition rate and at the highest pump power level of 4.8 W. Considering the low conversion efficiency, and hence low pump depletion, we can assume that the pump pulse shape does not change significantly after propagation through the OP-GaP crystal, as verified in Figure 4.7. The pump pulses at 1064 nm have a duration of 12.8 ns, while the generated signal pulses at 1659 nm have a duration of 5.7 ns, which is shorter than that of the pump, as expected. From the simultaneous measurement, we also clearly observed the characteristic delay between the pump pulse and the generated signal pulse, corresponding to a rise time of ~9.5 ns for the OP-GaP OPO. The periodic modulation in the pump pulse, also replicated in the signal pulse profile, is attributed to longitudinal mode beating in the pump laser.

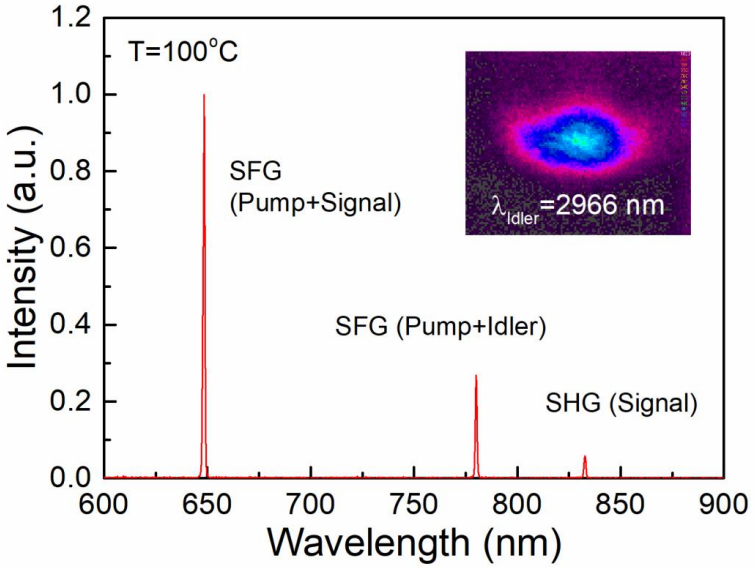

Figure 4.6. Parasitic light generated in the OP-GaP OPO at 100ºC. Inset: The idler output beam profile from the OPO.

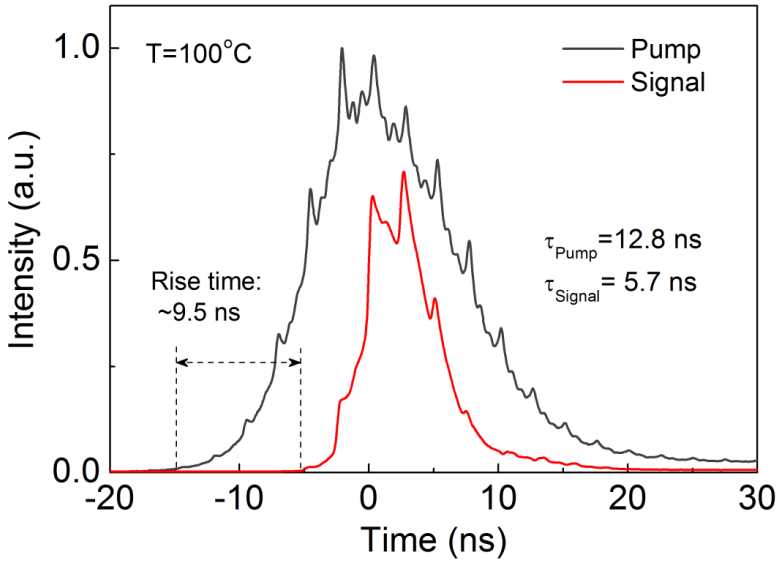

Figure 4.7. Simultaneously measured pulse shapes of the transmitted pump and generated signal for the OP-GaP OPO at 50 kHz repetition rate.

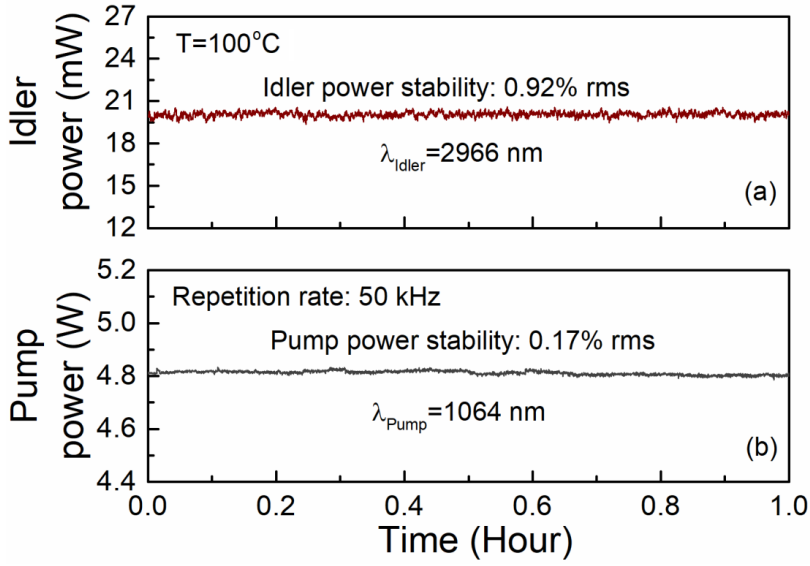

Figure 4.8. Power stability of the (a) idler power from the OP-GaP OPO, and (b) pump over a period of 1 hour.

4.3.6 Power stability

Further, we investigated the passive long-term power stability of the idler output from the OPO compared with that of the input pump laser, with the results shown in Figure 4.8(a) and (b). The measurements were performed at an OP-GaP crystal temperature of 100ºC and for a pump power of 4.81 W at 50 kHz repetition rate. The idler power from the OPO exhibits a passive stability of 0.92% rms with a mean value of 20.06 mW at 2966 nm over 1 hour, compared to a stability of 0.17% rms for the input pump over the same measurement period.

4.4 Conclusions

In conclusion, we have demonstrated what is to our knowledge the first nanosecond pulsed singly-resonant OPO based on OP-GaP crystal. Pumped by a Q-switched Nd:YAG laser at 1064 nm, the OPO generates signal and idler waves across 1.6-1.7 μm and 2.8-3.1 μm, respectively. From temperature-dependent wavelength tuning measurements at two different pump powers of 4.2 W and 1.2 W, a discrepancy of 11-17ºC in the internal crystal temperature across the tuning range is estimated, implying that the 40-mm-long OP-GaP sample suffers from increasing thermal effects at higher pump powers due to absorption. The OPO can provide idler power up to ~20 mW (0.4 μJ) at 2966 nm with a good power stability of 0.92% rms over 1 hour. The signal pulses at 1659 nm, extracted using a 5% output coupler, have typical duration of 5.7 ns, shorter than the 12.8 ns pump pulses, as expected. From simultaneous pulse measurements, the rise time of the OP-GaP OPO at the highest pump power level is ~9.5 ns. As a promising mid-IR nonlinear crystal, higher transmission, better uniformity and larger aperture size of the grating layers in

OP-GaP crystals are expected for further improving the performance of nanosecond OP-GaP OPOs, also providing the possibility of achieving efficient operation in other time-scales.

Chapter 5

Stable, high-average-power, degenerate optical parametric oscillator at 2.1 μm

5.1 Motivation

Pulsed coherent laser sources operating at ~2 μm are of great interest for various applications including LIDAR, biomedicine and study of new materials [107-109]. In addition, such sources can be used to drive nonlinear processes for mid-infrared or terahertz generation, in particular for pumping long-wave OPOs covering the 3-10 μm wavelength range. In such OPOs, non-oxide nonlinear crystals such as $ZnGeP_2$ (ZGP) and orientation-patterned GaAs (OP-GaAs), are required, which necessitate pumping beyond ~2 μm to avoid two-photon absorption. As such, high-power pulsed laser sources with linear polarization and high beam quality, operating at or slightly beyond ~2 μm, are of great demand for pumping such mid-IR OPOs. To date, laser sources at ~2 μm have been based predominantly on relatively specialist Tm- or Ho-doped solid-state and fiber laser technology. Near-degenerate OPOs pumped at ~1 μm represent a convenient, low-cost and efficient alternative to the development of high-power laser sources at ~2 μm. Similar to amplified spontaneous emission sources at ~2 μm, optical parametric down-conversion process exhibits a substantially broad emission spectrum near degeneracy. For the purpose of driving infrared

nonlinear crystals, dispersive elements such as diffraction gratings or prisms are necessary to be introduced into the OPO cavity for spectrally narrowing the output at ~2 μm, as well as providing rapidly tunable wavelengths for different applications. Volume Bragg gratings (VBGs) providing a narrow diffraction bandwidth at ~2 μm have also been demonstrated to be effective for this purpose [110,111]. However, the unavailability of broadband wavelength tuning in VBG-based OPOs makes it difficult to achieve the exact degeneracy and limits various wavelength-dependent applications. Our group has reported a high-quality, picosecond source at 2.1 μm providing up to ~7 W of average power based on a fiber-laser-pumped degenerate MgO:PPLN OPO [112]. A diffraction grating was used as a mirror in this ps OPO for narrowing the output linewidth down to ~2 nm at 2.127 μm. In this paper, we present a similar multi-watt degenerate MgO:PPLN OPO in nanosecond regime pumped by a widely available, low-cost Nd:YAG laser, providing variable repetition rates, high stability and a compact configuration. The spectrum of the degenerate wave is narrowed down to 3.9 nm using a grating-cavity configuration, compared to the inherent output bandwidth of 50 nm in the linear cavity. Moreover, wavelength tuning around degeneracy can be also achieved by simply rotating the diffraction grating.

5.2 Experimental setup

The experimental setup for the grating-cavity OPO is schematically shown in Figure 5.1. The pump laser is a linearly polarized, Q-switched Nd:YAG laser at 1.064 μm with variable repetition rate from 20 kHz to 100 kHz, with an average power up to ~30 W. The pump beam propagates through a half-wave-plate and a polarizing beam-splitter (PBS) for power attenuation. A second combination of a half-wave-plate and a PBS is used to attenuate the back-travelling pump beam, as the OPO is in a

double-pass-pump configuration. A third half-wave-plate corrects the polarization of the pump for achieving the type 0 ($e \rightarrow ee$) interaction in a MgO:PPLN crystal. The crystal is 50-mm-long, 2-mm-wide, and 1-mm-thick, with a single grating period of Λ=32.16 μm, and is mounted in an oven and temperature controlled at 72ºC for phase-matching at degeneracy. The crystal end-faces are antireflection (AR)-coated (R<0.5%) at 1064 nm and over 2050-2150 nm. The pump laser is focused to a beam waist radius of w_0~150 μm inside the crystal, corresponding to a loose focusing parameter of $\xi \sim 0.18$.

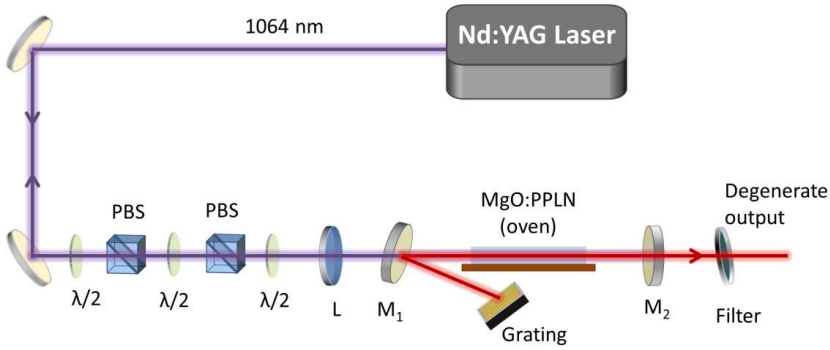

Figure 5.1. Schematic of the experimental setup for the grating-cavity OPO. λ/2, half-wave plate; PBS, polarizing beam-splitter; L, lens.

The OPO is configured in a V-shape, three-mirror cavity. Figure 5.2 shows a photograph of this OPO cavity in the laboratory. The input mirror, M_1, is highly transmitting (T>90%) for the pump at 1.064 μm and highly reflecting (R>99%) over 1.800-2.150 μm. The output coupler, M_2, is highly reflecting (R>90%) for the pump and partially transmitting (T~60%) at the degenerate wavelength, ensuring a double-pass-pump, doubly-resonant configuration for the OPO. A diffraction grating with a blazing wavelength of 2.16 μm and 600 grooves/mm (*Richardson Gratings*) is used in Littrow configuration as the third cavity mirror for spectrally narrowing the OPO output. The total optical length of the OPO cavity, including the crystal, is 126

mm providing 18 round trips of the resonant parametric waves over the 22 ns duration of the pump pulse at 80 kHz repetition rate. A long-pass filter (*Edmund Optics, 68652*) with a cut-on wavelength of 1.65 μm, outside of the cavity, is used to extract the degenerate OPO output from the residual transmitted pump. For the comparison of the output power and the spectral bandwidth, we also used linear OPO cavity configuration only composed of M_1 and M_2, with a total optical length of 78 mm, corresponding to 24 round trips of the resonant parametric waves over the pump pulse at 80 kHz repetition rate.

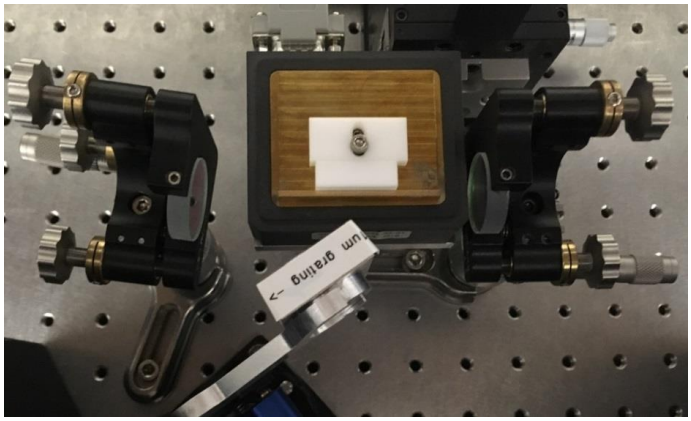

Figure 5.2. The photograph of the grating-cavity OPO in the lab.

5.3 Results and discussion

5.3.1 Power scaling and beam quality

In order to characterize the pulsed degenerate OPO, we first performed power scaling measurements at three different repetitions of 65 kHz, 80 kHz and 90 kHz, in both linear and grating-cavity configurations. In the linear cavity OPO, as shown in Figure 5.3, up to 4.1 W of the degenerate output at 2.1 μm was obtained for a pump

power of 10.2 W at 65 kHz repetition rate, corresponding to a slope efficiency as high as 44%. At 80 kHz and 90 kHz repetition rate, we obtained 4.3 W and 3.6 W of the degenerate output at 2.1 μm for pump powers of 12 W and 13 W, respectively. The corresponding slope efficiencies were 39.0% and 32.6%, respectively. As can be seen, a lower repetition rate, corresponding to a higher pump pulse energy, always results in higher conversion efficiency for the OPO. We also recorded the spatial profile of the degenerate output beam at 80 kHz repetition rate and the highest power using a pyroelectric camera. The result, shown in the inset of Figure 5.3, indicates a circular and uniform single-peak intensity distribution.

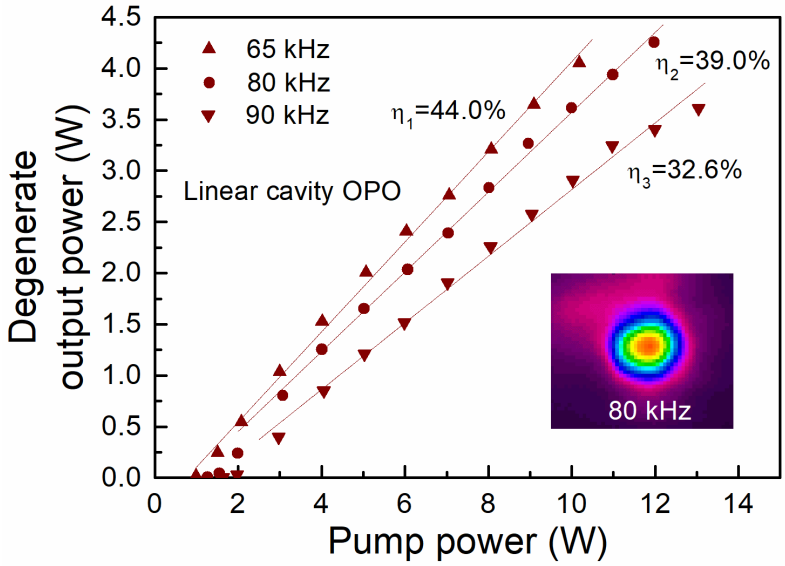

Figure 5.3. The degenerate output power of the linear cavity OPO as functions of the pump power at three repetition rates of 65 kHz, 80 kHz and 90 kHz. Inset: The corresponding beam profile of the degenerate output.

In the grating-cavity OPO, we performed similar measurements of power scaling and beam profile, as shown in Figure 5.4. The conversion efficiency here decreased compared to the linear cavity OPO due to the longer grating-cavity length and extra cavity loss introduced by the diffraction grating. The spectrally narrowed degenerate

output with highest powers of 2.3 W, 2.7 W and 1.8 W were obtained at 65 kHz, 80 kHz and 90 kHz repetition rate, for pump powers of 9.9 W, 13.7 W and 13.4 W, respectively, corresponding to slope efficiencies of 28.4%, 23.9% and 18.5%. The recorded spatial profile of the degenerate output beam at 80 kHz is shown in the inset of Figure 5.4. Compared to the circular profile in the linear cavity OPO, the output beam here shows a slightly prolate shape along horizontal direction. This can be attributed to the dispersive effect of the diffraction grating in the horizontal plane. We further characterized the beam quality of the spectrally narrowed output beam at 80 kHz and the highest power using a scanning-slit beam profiler. As shown in Figure 5.5, the M^2 of the degenerate beam at 2.1 μm was determined to be 3.7 in the horizontal plane and 2.7 in the vertical plane. Details of the method for measuring M^2 values have been described in [69].

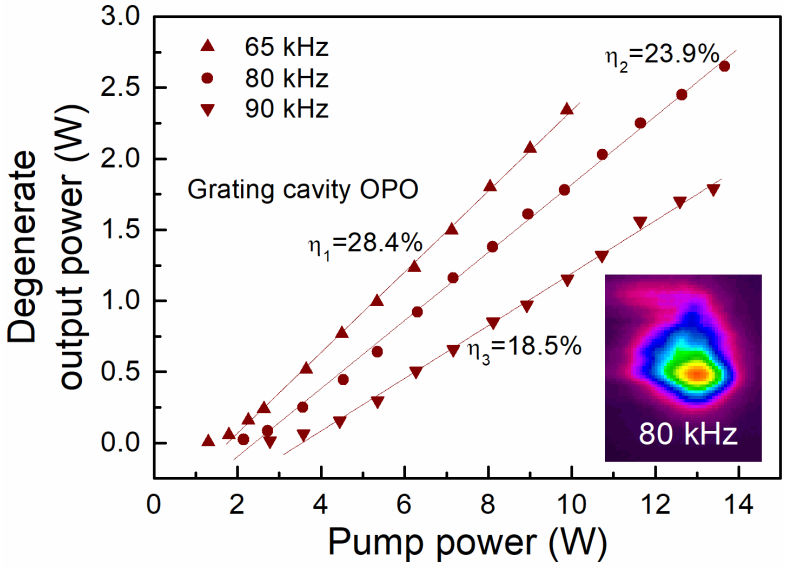

Figure 5.4. The degenerate output power of the grating-cavity OPO as functions of the pump power at three repetition rates of 65 kHz, 80 kHz and 90 kHz. Inset: The corresponding beam profile of the degenerate output.

In both two cavity configurations, the OPO always shows higher slope efficiency

with lower repetition rate, which is due to the relatively high pump peak power and pulse energy at lower repetition rates. Considering the double-pass-pump configuration, the average pump power was not increased beyond 14 W at the three repetition rates to avoid possible crystal damage.

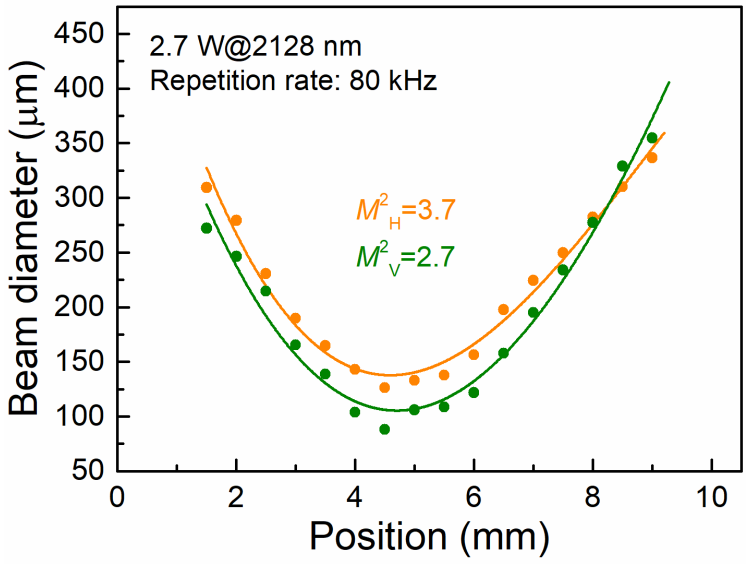

Figure 5.5. Variation of the focused beam diameter in horizontal and vertical plane along the propagation direction.

5.3.2 Power stability

The power stability of the degenerate output in both cavity configurations at 80 kHz repetition rate and the highest power were recorded, as shown in Figure 5.6(a) and (b). The linear cavity OPO provides an average output power of 4.25 W at degeneracy, exhibiting good power stability of 0.61% rms over 1 hour. In the grating-cavity OPO, the spectrally narrowed output exhibites a power stability of 1.05% rms at 2.7 W over 1 hour, which is only slightly degraded compared to the linear-cavity OPO. The power stability of the input pump at 80 kHz was also recorded for a comparison, which is 0.23% rms over 1 hour with a mean value of 12.0 W, as

shown in Figure 5.6(c). This measurement has confirmed the stable and high-average-power characteristics of our degenerate OPO in both cavity configurations.

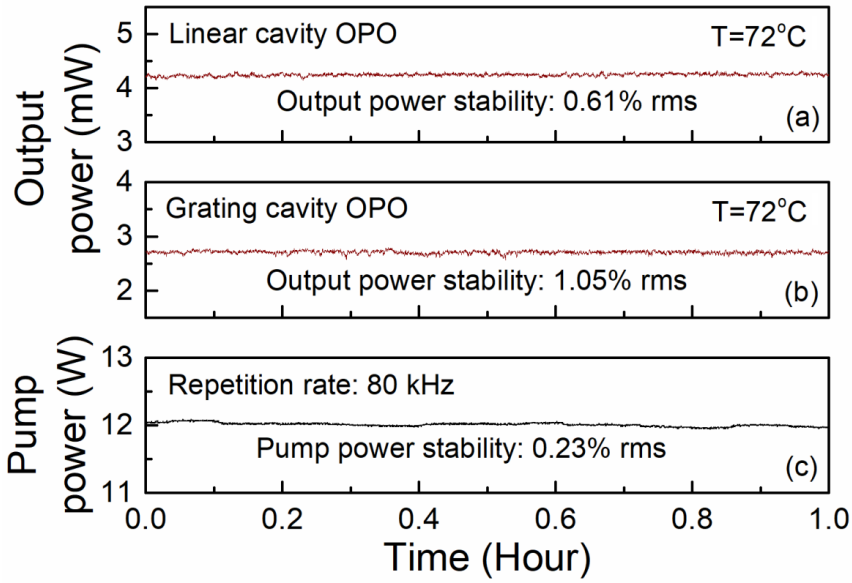

Figure 5.6. Power stability of (a) the linear cavity OPO output, (b) the grating-cavity OPO output, and (c) the pump over a period of 1 hour.

5.3.3 Pulse temporal characterization

In the grating-cavity OPO, we further investigated the temporal characteristics of the degenerate output at 2.1 μm, including the pulse duration, pulse-to-pulse stability, and exact repetition rate. Using a fast photodetector (*Alphalas, UPD-5N-IR2-P*) and a digital oscilloscope with a bandwidth of 3.5 GHz, we were able to record the pulse shape of the pump and the degenerate output, as shown in Figure 5.7(a) and (b). The pump pulses at 1064 nm have a pulse duration of 22.1 ns at 80 kHz and the degenerate output pulses at 2.1 μm have a duration of 20.5 ns. As can be seen, the degenerate output has close and comparable pulse duration to the input pump, which is because the double-pass-pump scheme and the compact cavity design greatly

reduces the build-up time in the OPO. By increasing the measurement duration to 100 ms on the oscilloscope, we also obtained a long pulse train of the degenerate output at 80 kHz, as shown in Figure 5.8(a). Further analysis indicates that the spectrally narrowed degenerate output has a good pulse-to-pulse stability of 3.18% rms over 100 ms, corresponding to ~8000 consecutive pulses. The Fourier transform of Figure 5.8(a) was also performed to reveal the fundamental beam frequency of 78.68 kHz with a signal-to-noise ratio (SNR) of 37 dB, confirming the exact repetition rate of the OPO, as shown in Figure 5.8(b).

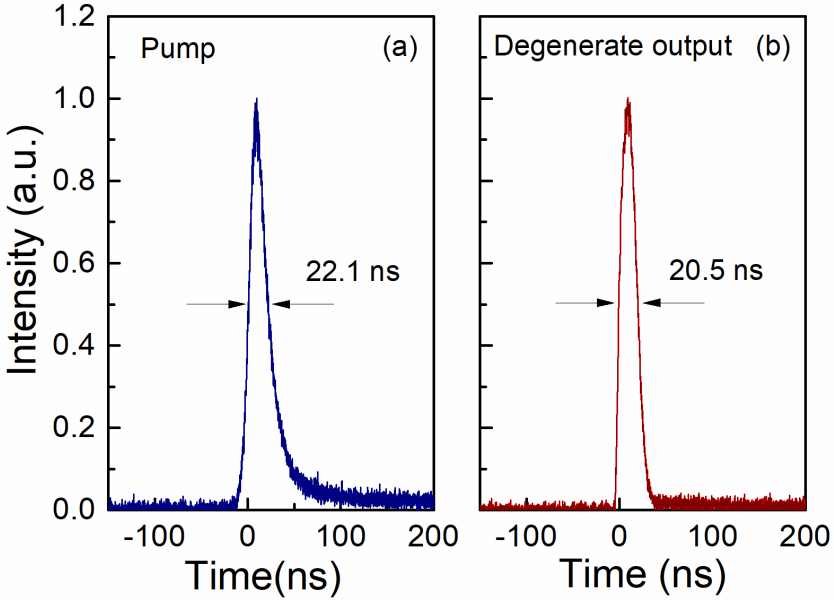

Figure 5.7. Pulse shapes of the (a) pump and (b) degenerate output of the grating-cavity OPO.

5.3.4 Spectral narrowing effect

Finally, we examined the spectral narrowing effect of the grating-cavity OPO compared to the linear cavity configuration. The results are shown in Figure 5.9(a) and (b). In the linear cavity OPO, using an infrared spectrometer (*StellarNet, RED-Wave-NIRX-SR*) based on an extended-range InGaAs photodiode array, we

measured the bandwidth of the degenerate output to be ~50 nm with a resolution of ~13 nm, confirming broadband emission at degeneracy. In the grating-cavity OPO, in order to determine the linewidth of the degenerate wave, we used a home-made spectrometer based on a diffraction grating of 420 grooves/mm and a 50-μm-silt for measurement. The spectrometer has a wavelength scanning resolution of ~0.7 nm, resulting in a measured linewidth of 3.9 nm at degeneracy. This dramatically narrowed OPO output spectrum confirms the effectiveness of the grating-cavity in Littrow configuration. The actual degenerate wavelength of 2126.5 nm was further confirmed by measuring the non-phase-matched sum-frequency-generation (SFG) spectrum between the pump and the degenerate wave, using a visible spectrometer with a resolution of 0.5 nm (*Ocean Optics, HR4000*).

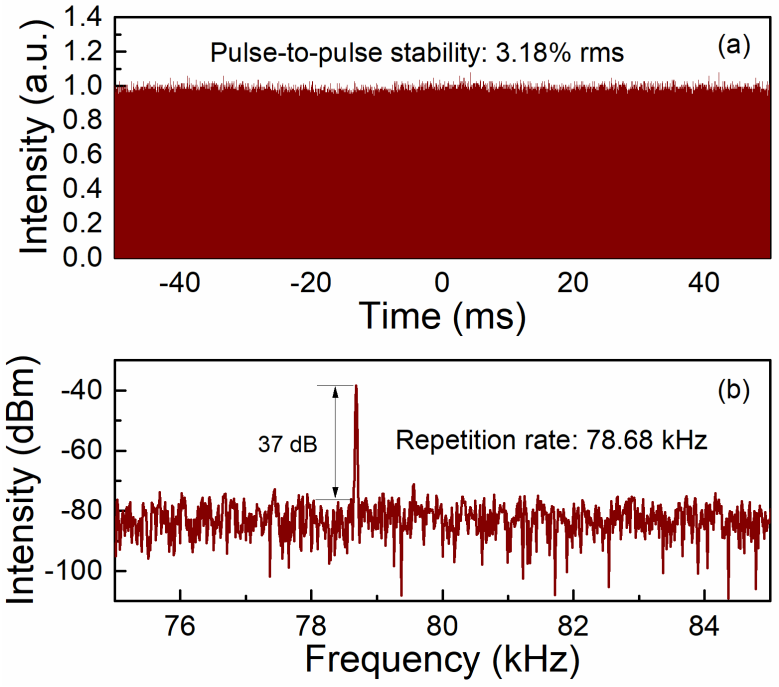

Figure 5.8. (a) The pulse train of the degenerate output from the grating-cavity OPO. (b) RF spectrum of the degenerate output from the grating-cavity OPO.

In order to further show the wavelength tuning capability of the grating-cavity

OPO near degeneracy, we later slightly rotated the diffraction grating to select different wavelengths as feedback for the OPO. As a result, the degenerate output spectrum started to show a double-peak profile and was gradually split into distinguishable signal and idler spectra around degeneracy. An example is shown in Figure 5.9(b) with the dashed line. By simply tuning the grating angle without changing the temperature of the MgO:PPLN crystal, we obtained signal and idler wavelengths of 2118 nm and 2136 nm with similar spectral bandwidths to the degenerate output, indicating a tuning range of ~18 nm around degeneracy.

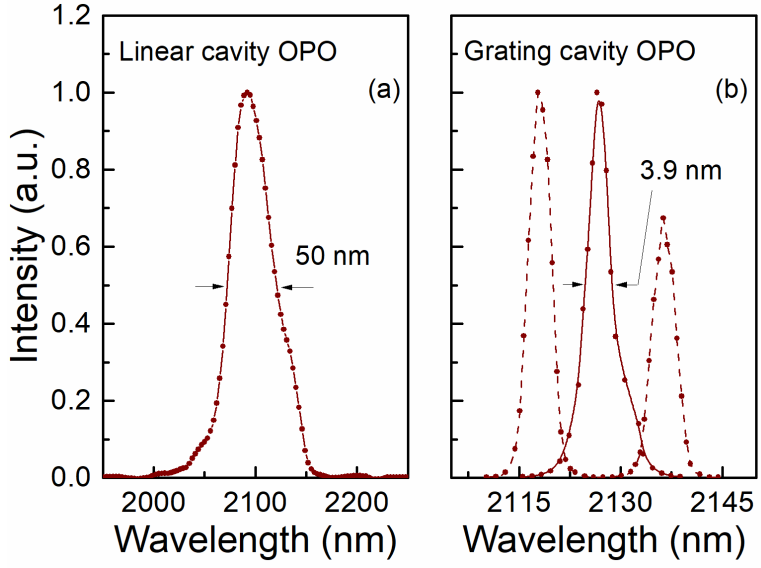

Figure 5.9. The output spectrum of the (a) linear cavity OPO and (b) grating-cavity OPO.

5.4 Conclusions

In conclusion, we have demonstrated a pulsed, spectrally-narrowed MgO:PPLN OPO at 2.1 μm pumped by a repetition-rate-variable Q-switched nanosecond Nd:YAG laser at 1064 nm. The OPO in linear cavity and grating-cavity configuration can

provide degenerate output with average power up to 4.3 W and 2.7 W, respectively, at 80 kHz repetition rate with good power stability over 1 hour. In the grating-cavity OPO, the beam quality of the spectrally narrowed degenerate output was measured to be 3.7 in the horizontal plane and 2.7 in the vertical plane at 80 kHz repetition rate and at the highest power level. The temporal characteristics of the grating-cavity OPO show a degenerate output pulse duration of 20.5 ns, similar to that of the pump, due to the short build-up time, and good pulse-to-pulse stability of 3.18% rms during 100 ms for the degenerate wave at 80 kHz repetition rate. Meanwhile, the radio frequency spectrum of the degenerate pulses was also obtained through Fourier transform, revealing an actual repetition rate of 78.68 kHz for the OPO. The grating-cavity in Littrow configuration squeezed the OPO output bandwidth down to 3.9 nm at degeneracy compared with ~50 nm in the linear cavity OPO. In addition, wavelength tuning around the degeneracy can be also achieved by simply rotating the diffraction grating. This stable, high-average-power laser source around 2.1 μm is a potential alternative to Tm- and Ho-based solid-state lasers for a variety of applications including pumping long-wave infrared OPOs and generating terahertz wave through DFG process.

Chapter 6

Pulsed single-frequency difference-frequency-generation for high-resolution spectroscopy

6.1 Motivation

The mid-IR spectral region of 3-5 μm covers strong absorption lines of a number of molecules with CH, NH and OH stretching vibrations. Detection and analysis of these molecules are of great interest in many real-world applications such as combustion diagnostics [113,114] and environmental monitoring [115,116]. Nanosecond pulsed optical parametric oscillators (OPOs) tunable in the mid-IR with multi-μJ-level pulse energy have been considered to be a versatile and high-sensitivity tool for above purposes. The achievable narrow linewidth close to Fourier transform limit makes them more attractive for resolving fine molecular absorption lines or distinguishing different species with high selectivity. However, the strong parametric gain of such OPOs usually excites relatively broad spectrum in the mid-IR idler pulse. Dispersive elements such as diffraction gratings or etalons need to be introduced into the OPO cavities to narrow the output spectrum, as discussed in chapter 5. A pulsed OPO with a proper design in grazing-incidence grating cavity configuration is capable to deliver single-longitudinal-mode (SLM) mid-IR idler pulses [117-119]. The

wavelength tunability can also be achieved by carefully rotating the end mirror of the cavity. However, continuous SLM tuning will involve precise control of the pivot point of the end mirror or complicated active control of the cavity length [117]. Injection-seeded OPOs based on highly stable single-frequency diode lasers have also been widely investigated in the last two decades [120-124]. The precise control of temperature and pump current for these diode lasers enables continuous single-frequency tuning in the OPO signal wavelength. When the wavelength of the SLM pulsed pump laser is also stabilized, the generated OPO idler wavelength can be finely tuned without mode-hops. However, the OPO cavity length has to be actively controlled to match the exact wavelength of the tunable seed laser by use of a complex electronic feedback system. Injection-seeded OPO configuration is preferable when using traditional phase-matching crystals, where the available nonlinear coefficient is relatively low and an oscillator is usually needed to enhance the conversion efficiency. Injection-seeded OPG sources have also been realized in recent years with the advent of QPM nonlinear crystals [125-130], especially PPLN. The simple difference-frequency interaction between the pulsed pump and the cw seed in PPLN allows efficient generation of mid-IR idler with narrow linewidth. Compared to injection-seeded OPOs, this single-pass configuration doesn't require a cavity or any electronic stabilization schemes. The mode-hop-free tuning of the idler can be easily achieved by only scanning the temperature or pump current of the seed laser. The linewidth of idler pulses in such differency-frequency-generation (DFG) sources is strongly dependent on the parameters of the pump and the seed. Micro-chip pulsed lasers have proven to be compact and efficient pump sources [125-127]. The sub-ns pulse duration of these lasers, however, sets a Fourier transform limit for the idler linewidth at GHz level, and the laser wavelength can also shift from pulse to pulse leading to wavelength instability in the idler. Q-switched, injection-seeded

solid-state lasers, on the other hand, can provide higher spectral performance for this type of pulsed DFG sources. Output linewidths below 200 MHz have been reported based on such pump lasers [130].

In this chapter, we demonstrate a SLM pulsed DFG source tunable around 3.31 μm. The pump laser is an injection-seeded SLM flash-pumped Nd:YAG laser at 1064.43 nm and 10 Hz repetition rate, and the seed laser is a cw single-frequency, fiber-coupled, discrete-mode diode laser tunable around 1568 nm. The difference-frequency mixing between the two lasers in a MgO:PPLN crystal can provide SLM idler energy up to ~10 μJ. We further utilized this DFG source for methane absorption spectroscopy. High-resolution spectra in the Q-branch of methane ν_3-band were obtained in low gas pressure environment.

6.2 Experimental setup

The experimental setup for the pulsed DFG source and methane absorption spectroscopy is shown in Figure 6.1. The DFG pump source is a flash-pumped, electro-optic Q-switched Nd:YAG laser (*Spectra-Physics, Quanta-Ray*) with a repetition rate of 10 Hz and a typical pulse duration of ~9 ns. A cw single-frequency seed laser at 1064.43 nm is integrated into the source to provide stable SLM injection. The injection-seeded laser pulses have a nominal linewidth less than 0.003 cm^{-1} with output energy up to ~500 mJ. A beam-splitter with ~2% transmission at 1064 nm is used to extract a small fraction of the pump beam for frequency conversion. A telescope system composed of a convex lens, L_1 (f=300 mm), and a concave lens, L_2 (f=-75 mm), is used to reduce the pump beam diameter to 2.5 mm. The pump energy is further precisely controlled using an attenuator comprising a half-wave-plate and a

Brewster plate. The seed laser is a fiber-coupled, cw discrete-mode laser diode tunable around 1568 nm, with no mode-hops at a linewidth of 2 MHz (*Eblana Photonics, EP1580-DM-B*). A tunable wave-plate is used as a half-wave-plate to rotate the seed laser polarization to horizontal, the same as the pump.

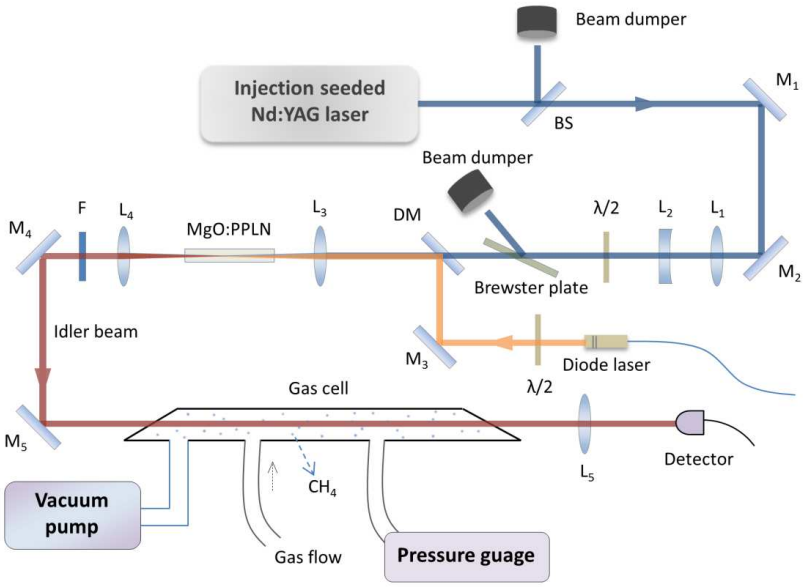

Figure 6.1. Schematic of the experimental setup for the pulsed DFG source and CH_4 absorption spectroscopy. BS, beam-splitter; M_1-M_5, mirrors; L_1-L_5, lenses; λ/2, half-wave-plate; DM, dichroic mirror; F, filter.

The two input beams are combined using a dichroic mirror and focused to a similar beam waist radius of w_0~70 μm using a lens, L_3, of focal length, f=150 mm. The MgO:PPLN crystal used for DFG is 50-mm-long, 2-mm-wide and 1.9-mm-thick with a single grating period of Λ=30.7 μm. It has antireflection (AR)-coated end-faces at 1064 nm (R<1%), 1450-1600 nm (R<5%), and 3200-3800 nm (R<1%). The crystal is temperature controlled at 53°C in an oven and has its z-axis parallel to the polarization of the input pump and seed laser to fulfill the QPM condition. A lens, L_4 (f=200 mm), is used in the optical path to collimate the pump, amplified signal and

generated idler. The mid-IR idler beam is later extracted using a long-pass filter with a cut-on wavelength of 2.4 μm (*Edmund optics, 68653*).

The gas cell used for methane absorption spectroscopy is 40-cm-long sealed off with two Brewster windows at both ends. The gas flowing into the cell is transferred from the combination of two gas tubes. One tube contains 1% CH_4 diluted in N_2 and the other contains pure N_2 for further diluting CH_4. The flow rates in the two tubes are precisely controlled by flow controllers, so that we are able to obtain an arbitrary concentration of CH_4 between 0 and 1%. A vacuum pump is connected to the gas cell to actively control the gas pressure and a pressure guage is used to monitor the real-time pressure in the cell. The generated mid-IR idler beam is directed by two mirrors, M_4 and M_5, to propagate through the gas cell and focused by a lens, L_5, onto an indium antimonide (InSb) detector (*Teledyne Judson technologies, J10D-M204-R0 4M-60*). The InSb detector is cooled down to 77 K using liquid N_2 to minimize the inherent thermal noise. The signal obtained by the detector is further amplified by an electronic amplifier with a bandwidth of up to 574 kHz. The entire experimental setup in the laboratory is shown in Figure 6.2.

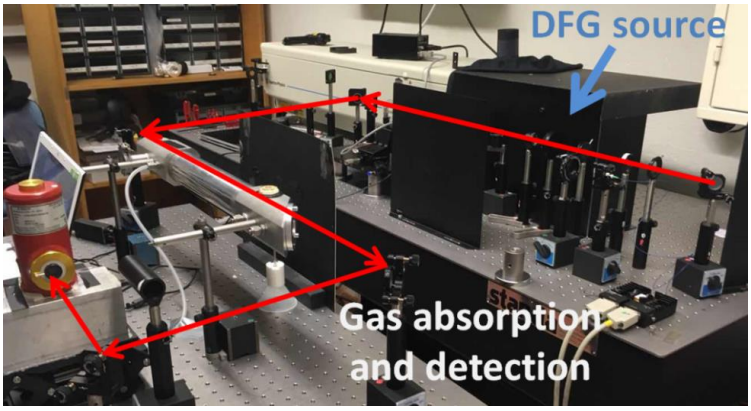

Figure 6.2. The photograph of the experimental setup for the DFG and CH_4 absorption spectroscopy in the lab.

6.3 Characterization of the DFG source

6.3.1 Wavelength tunability of the seed laser

The cw seed laser at signal wavelength of the DFG source is driven by a temperature and current controller. The wavelength of the seed laser varies with the pump current as well as the temperature of the laser diode. In this experiment, we fix the pump current at 100 mA to ensure a relatively high output power of 6.4 mW for effective seed injection, and then scan the laser diode temperature to achieve wavelength tuning. Using an infrared wavemeter to read the exact wavelength of the seed laser, we obtained the dependence of the seed wavelength on the diode temperature for a pump current of 100 mA, as shown in Figure 6.3.

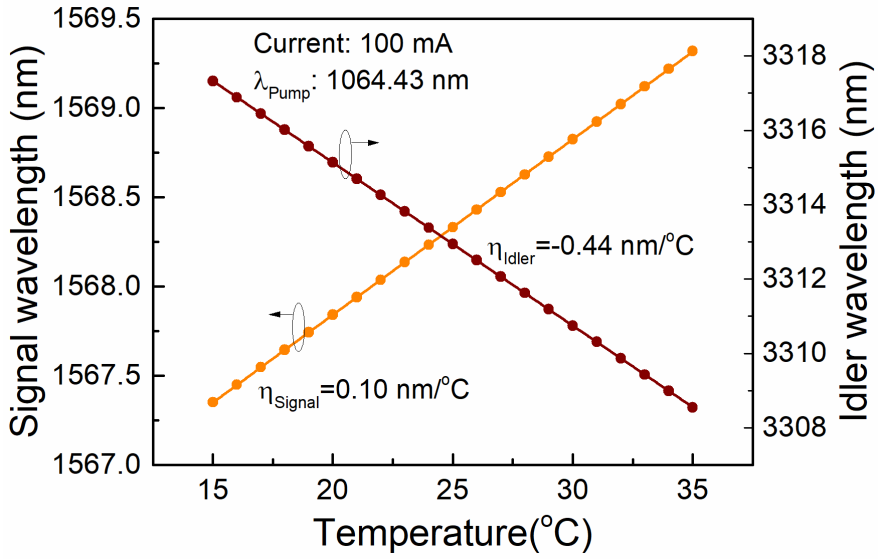

Figure 6.3. The dependence of the seed wavelength and DFG idler wavelength on the diode temperature for a pump current of 100 mA.

By scanning the diode temperature from 15°C to 35°C, a wavelength range of 1567.4-1569.3 nm can be swept for the seed laser with a slope efficiency of 0.1 nm/°C.

This linear wavelength increase versus diode temperature allows us to know the exact seed wavelength at any temperature between 15°C and 35°C. Using photon energy conservation, the linear correspondence between the diode temperature and the idler wavelength can be also calculated. The right *y*-axis of Figure 6.3 shows the corresponding idler has a tuning range of 3317.3-3308.5 nm with a slope efficiency of -0.44 nm/°C.

6.3.2 Idler energy across tuning range

In order to find the optimum crystal temperature to achieve phase-matching and obtain the highest parametric gain for the DFG source, we fixed the diode temperature of the seed laser at 25°C, corresponding to the wavelength in the middle of the tuning range, and scanned the temperature of the MgO:PPLN crystal. By monitoring the idler energy of the DFG when scanning the crystal temperature, we found that the optimized temperature corresponding the highest idler energy was 53°C. For a 50-mm-long MgO:PPLN crystal, the signal wave of the DFG is calculated to have a FWHM spectral acceptance bandwidth of ~2 nm around 1568 nm. Thus, the idler wavelength can be simply tuned by scanning the seed laser wavelength without simultaneously changing the crystal temperature. For a fixed pump pulse energy of 140 μJ at 1064 nm and a crystal temperature of 53°C, we performed the measurement of idler energy across the tuning range, as shown in Figure 6.4. When the idler wavelength is tuned from 3308.5 nm to 3317.3 nm, the corresponding output idler energy varies from 9.9 μJ to 10.4 μJ showing a relatively flat energy variation across the range. The slight power drop at both ends of the curve can be attributed to the limit of the spectral acceptance bandwidth of the crystal. The highest idler energy across the tuning range was recorded to be 11.8 μJ at 3314.7 nm, corresponding to a peak power of >1 kW. As a comparison, with the seed laser switched off, the idler

energy dropped down to the OPG level of 6.2 μJ.

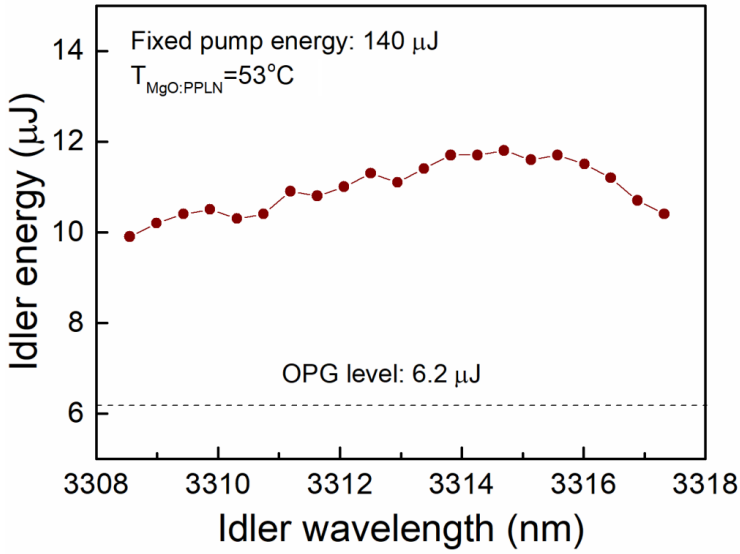

Figure 6.4. Variation of the idler energy across the tuning range.

6.3.3 Energy scaling

We further characterized the idler energy scaling for the DFG source at two different wavelengths. The results are shown in Figure 6.5(a) and (b). The temperature of MgO:PPLN crystal was still kept at 53°C. By shifting the diode temperature of the seed laser to 18°C in the DFG, we could directly obtain an idler wavelength of 3316.0 nm. When we gradually increased the pump energy up to 140 μJ, corresponding to a pump intensity of ~0.9 J/cm^2 in the MgO:PPLN crystal, the idler energy at this wavelength scaled up to 11.5 μJ with a slope efficiency of 14.1%, representing a photon conversion efficiency of 25.6%. For a diode temperature of 32°C in the seed laser of the DFG, the idler wavelength is switched to 3309.9 nm. The idler energy in this case reached a highest value of 10.6 μJ with a slope efficiency of 11.4% for the same pump energy of 140 μJ at 1064 nm. The corresponding photon conversion efficiency is calculated to be 23.5%. Considering that the long-pass filter used to

extract the idler power has ~95% transmission around 3.31 μm, the actual DFG conversion efficiency can be slightly higher than the values given here.

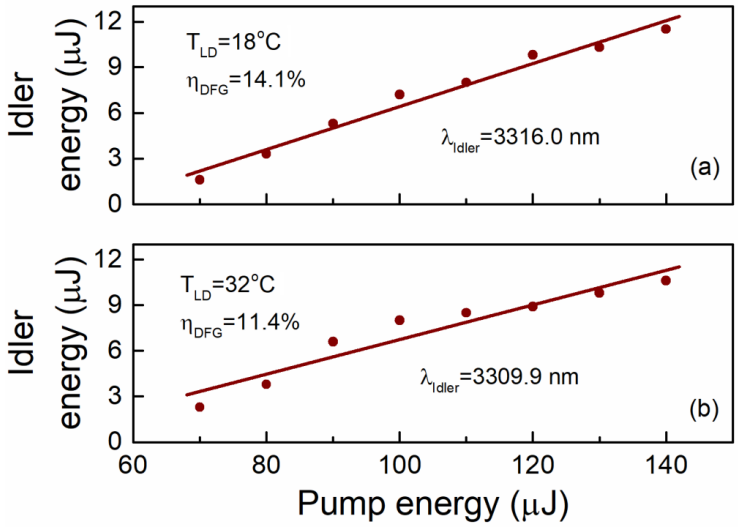

Figure 6.5. Extracted idler energy at (a) 3316.0 nm and (b) 3309.9 nm as functions of the input pump energy.

6.3.4 Pulse temporal characterization

Using a high-speed InGaAs photodetector (*Thorlabs, DET08C*) with 5 GHz bandwidth and a digital oscilloscope with 1 GHz bandwidth, we investigated the pulse temporal characteristics of the DFG source. The results are shown in Figure 6.6(a)-(d). For a pump energy of 140 μJ and a seed laser wavelength of 1568.3 nm, we measured the pump pulse depletion in the cases of OPG (without seeding) and DFG (with seeding) for comparison. The blue traces in Figure 6.6(a) and (b) show the input pump pulse shape with a typical duration of 9.3 ns. In the OPG process, the transmitted pump pulse is obviously depleted compared to the input pulse. From the residual pump pulse profile of OPG, we found that the pump pulse peak with highest instantaneous intensity didn't correspond to the strongest depletion of its intensity, but

a reduced value. This is because this high pump peak intensity led to a high conversion efficiency, resulting in adequate signal and idler photon generation, so that back-conversion took place. In the back-conversion process, these signal and idler photons could conversely combine and regenerate pump photons through sum-frequency process in the crystal, limiting the total conversion efficiency [131,132] and responsible for the reappearance of the central peak in the pump pulse. This phenomenon has been observed elsewhere [133]. In the DFG process, except for similar back-conversion phenomenon, we also noticed that the intensity depletion on the leading edge of the pump pulse took place earlier at a low intensity level, which means the injection seeding effectively reduced the threshold of parametric down-conversion.

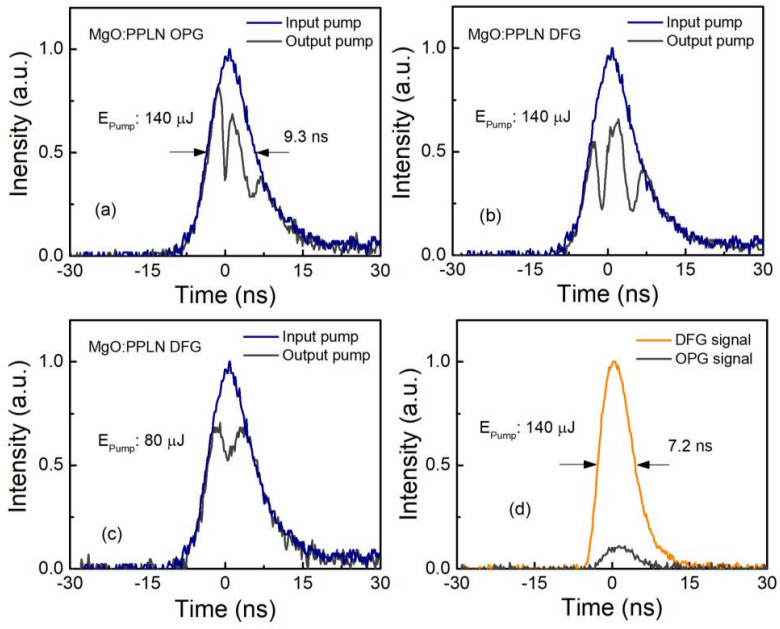

Figure 6.6. Pulse temporal characterization for the DFG. (a) Pump pulse depletion in OPG. (b) Pump pulse depletion in DFG. (c) Pump pulse depletion in DFG below OPG threshold. (d) Signal pulse comparison in OPG and DFG.

Later, we reduced the pump pulse energy to 80 μJ, where the DFG can still take

place while the OPG is halted. At this pump energy level, we repeated the pulse shape measurement for the residual pump of DFG. As can be seen in Figure 6.6(c), the pump intensity depletion is weaker compared to that with 140 μJ pump energy in Figure 6.6(b). Besides, the strongest intensity depletion corresponds to the pump pulse peak position, as predicted, and back-conversion is eliminated due to lower conversion efficiency. Figure 6.6(d) illustrates a comparison of signal pulses in OPG and DFG. For a pump energy of 140 μJ, we recorded a smooth signal pulse with a duration of 7.2 ns through DFG. By blocking the seed laser beam in the optical path, we observed a dramatic intensity drop in the generated signal pulse. This large difference of signal pulse intensity between the DFG and OPG can be partially attributed to the reduced conversion efficiency without seed injection. Moreover, the high-beam-quality seed laser can also improve the directionality of the generated signal pulses, so that more signal photons from the DFG can be directed to the detector for measurement compared to the OPG.

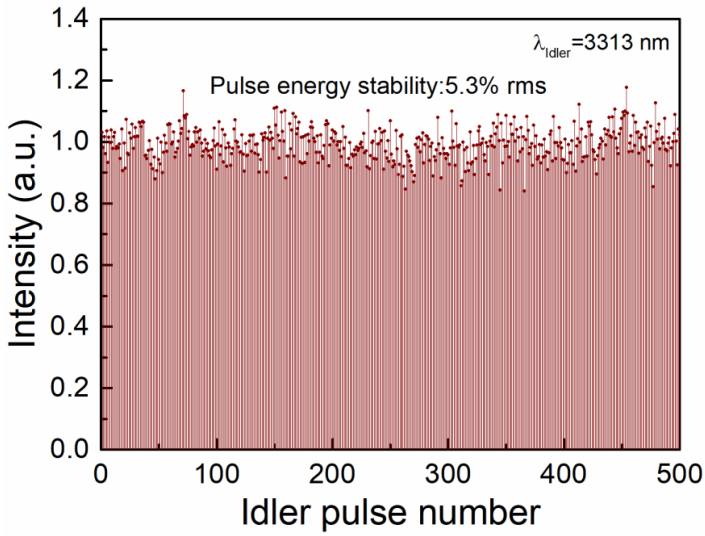

Figure 6.7. Idler pulse energy stability of the DFG.

In addition, we also performed the idler energy stability measurement for the

DFG. The pump energy and the seed laser wavelength were still kept at 140 μJ and 1568.3 nm, respectively. The generated idler wavelength was thus calculated to be 3313 nm. We used the InSb detector, described previously, to obtain idler pulse intensity. Figure 6.7 shows the energy stability of 500 consecutive idler pulses generated by DFG, corresponding to a measurement time of 50 s, given a repetition rate of 10 Hz. This measurement shows an idler energy pulse-to-pulse stability of 5.3% rms with a normalized mean value. This fairly stable idler output from the DFG enables us to obtain reliable results after averaging in methane absorption measurement.

6.4 CH_4 absorption spectroscopy

In order to demonstrate the potential of the DFG source for high-resolution absorption spectroscopy, we further implemented methane detection experiment. The wavelength tuning range of the DFG idler from 3308.5 nm to 3317.3 nm, corresponding to 3014.5 cm^{-1} to 3022.5 cm^{-1}, coincides with the Q-branch of methane vibrational v_3-band. Initially, we kept the gas cell at atmospheric pressure and controlled the concentration of methane at 0.1% in the flow-in gas for absorption measurement. At atmospheric pressure, collision broadening effect of methane molecules results in the overlap of fine spectral lines, resulting in an absorption band. Figure 6.8 shows the recorded absorption spectrum of 0.1% methane buffered in nitrogen between 3018 cm^{-1} and 3019.2 cm^{-1}, as well as a theoretical simulation based on HITRAN 2012 database for comparison. The spectral interference of water vapor and CO_2 in the air located in this range is negligible compared to 0.1% methane. This idler wavenumber tuning range is achieved by scanning the diode temperature of the seed laser from 23°C to 26°C in steps of 0.1°C, corresponding to an idler step of

~0.04 cm^{-1}. The experimental measurement using our SLM DFG source resolved the four absorption peaks in the simulated curve, showing a good agreement with the HITRAN simulation.

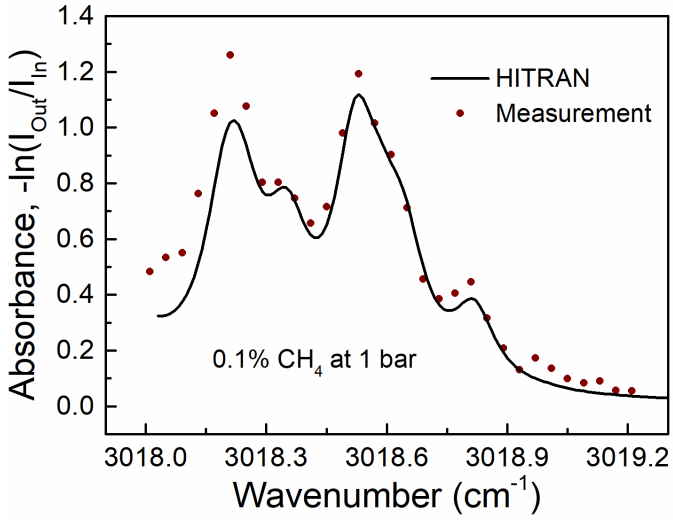

Figure 6.8. Measurement of the absorption spectrum of 0.1% CH_4 buffered in nitrogen at atmospheric pressure and room temperature.

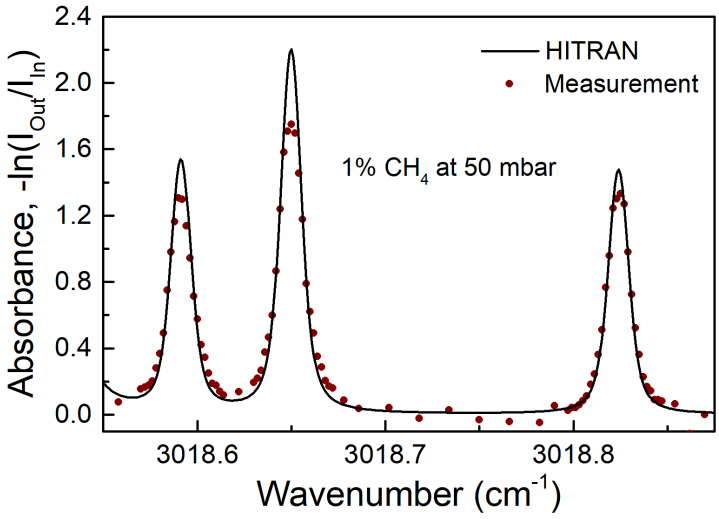

Figure 6.9. Measurement of the absorption spectrum of 1% CH_4 buffered in nitrogen at 50 mbar and room temperature.

A higher-resolution CH_4 spectroscopy exploiting the mode-hop-free tuning and

single-frequency characteristics of the DFG source was also demonstrated. In order to do so, we reduced the pressure in the gas cell down to 50 mbar using a vacuum pump. The flow-in gas here comprises 1% methane and nitrogen as buffer. A 20 times reduced gas pressure here can much alleviate the collision broadening effect. As a result, the absorption curve in the same spectral range as in Figure 6.8 becomes narrower and discrete with spectral peaks. As shown in Figure 6.9, we focused on a narrower mid-IR range of 3018.558 to 3018.870 cm^{-1} for resolving fine structures in the Q-branch of the methane v_3-band. The mode-hop-free tuning in the idler wavelength was achieved by scanning the diode temperature of the seed laser within 24.35-25.13°C with a smallest step down to 0.005°C, corresponding to an idler step of ~0.002 cm^{-1}. Three spectral peaks were successfully resolved in this region, with the measurement showing a good agreement with the HITRAN simulation, as compared in Figure 6.9. Furthermore, we detected the spectral line centered at 3018.65 cm^{-1} with a theoretical FWHM linewidth of 0.018 cm^{-1} for idler linewidth determination. The actual measurement for this spectral line gives a slightly broadened FWHM linewidth of 0.0196 cm^{-1}. The idler linewidth was thus determined to be ~0.007 cm^{-1}, corresponding to ~210 MHz, through a deconvolution calculation. This result shows that our tunable single-frequency pulsed DFG source is capable of resolving closely spaced and narrow spectral lines of methane in a low-pressure environment. The idler wavelength of such a DFG source can be further extended to vibrational bands of various molecules in the mid-IR by changing the seed laser wavelength and the crystal phase-matching condition.

6.5 Conclusions

In conclusion, we have demonstrated a nanosecond pulsed, single-frequency,

mode-hop-free tunable DFG source based on MgO:PPLN and pumped by an injection-seeded Q-switched Nd:YAG laser at 10 Hz. Seeded by a cw single-frequency, fiber-coupled, discrete-mode diode laser, the idler wavelength of the DFG can be tuned from 3308.5 nm to 3317.3 nm by scanning the seed laser wavelength within the spectral acceptance bandwidth of the MgO:PPLN crystal. For a pump pulse energy of 140 μJ, the DFG can provide 10-μJ-level idler energy across the full tuning range, corresponding to a photon conversion efficiency over 20%. From the pulse temporal studies, we observed back-conversion in both OPG and DFG at a high pump energy level of 140 μJ. The generated smooth DFG signal pulses at 1568.3 nm have a typical duration of 7.2 ns, shorter than that of the pump pulses. The DFG idler pulse energy stability at 3313 nm was recorded to be 5.3% rms for 500 consecutive pulses.

We further exploited this DFG source for methane absorption spectroscopy. A part of the Q-branch spectrum in methane v_3-band was detected and compared to the HITRAN simulation at atmospheric pressure. At a reduced pressure of 50 mbar, the DFG was also tested to be capable of resolving fine spectral lines with a linewith of ~0.007 cm^{-1} under mode-hop-free tuning operation. Our results show that this type of DFG source has the potential to serve as a versatile light source for various high-resolution spectroscopy applications in the mid-IR. With further power and energy scaling using another amplification stage, such a laser can also be used in LIDAR applications and nonlinear spectroscopy such as degenerate four-wave mixing and polarization spectroscopy.

Chapter 7

Summary and outlook

This thesis has focused on the demonstration and study of novel nanosecond pulsed optical parametric sources in the mid-infrared (mid-IR) region, as well as the application in high-resolution molecular spectroscopy. Towards the goal of developing compact and efficient optical parametric sources in the deeper mid-IR beyond ~4 μm, we have investigated a new semiconductor nonlinear crystal, orientation-patterned gallium phosphide (OP-GaP), and also developed a compact 2.1-μm source, which is promising for pumping traditional non-oxide nonlinear crystals. Moreover, by deploying injection seeding scheme, we have realized a pulsed single-frequency source with precisely controlled wavelength and further demonstrated its capability in resolving high-resolution molecular spectra. A more detailed description of the main outcomes in this thesis is given as below:

- We have achieved the first successful operation of an optical parametric generator (OPG) in OP-GaP. The single-pass OPG at 25 kHz repetition rate can provide total output power up to 18 mW with a good passive stability of 0.87% rms over 1 hour. The temperature tuning characterization shows OPG tuning range across 1721-1850 nm and 2504-2787 nm. The measurement of temperature-dependent pump transmission at 1064 nm along the [100] axis has also been performed, for the first time, indicating a drop in transmission

from 28.8% at 50ºC to 19.4% at 160ºC.

- Following the successful demonstration of OP-GaP OPG, we further constructed the first nanosecond singly-resonant optical parametric oscillator (OPO) based on OP-GaP. The OPO at 50 kHz repetition rate can deliver 20 mW of idler power with a good passive stability of 0.92% rms over 1 hour. By optimizing the crystal position and cavity alignment to compensate for the beam pointing deviation in OP-GaP at each temperature, we obtained a relatively smooth idler power across a tuning range of 2.85-3.1 μm. From temperature-dependent wavelength tuning measurements at two different pump powers of 4.2 W and 1.2 W, a discrepancy of 11-17°C in the internal crystal temperature is estimated, implying that the OP-GaP sample suffers from increasing thermal effects at higher pump powers due to absorption.

- A pulsed, spectrally-narrowed, degenerate MgO:PPLN OPO at 2.1 μm in the Littrow grating-cavity configuration has also been demonstrated as a potential alternative to Tm- and Ho-based solid-state lasers for pumping long-wave mid-IR OPOs and for generating terahertz radiation through DFG process. At a repetition rate of 80 kHz, the OPO can provide as much as 2.7 W of the degenerate output power. The M^2 factor of the corresponding output was measured to be 3.83 in the horizontal plane and 2.48 in the vertical plane. The OPO stability characterization shows a good long-term power stability of 1.05% rms over 1 hour, and a pulse-to-pulse stability of 3.18% rms during 100 ms for the degenerate output at maximum power. The degenerate spectral width of the grating-cavity OPO was narrowed down to 3.9 nm compared to 50 nm in the linear cavity OPO.

- Furthermore, a pulsed, mode-hop-free tunable, single-frequency

difference-frequency-generation (DFG) source aiming at resolving fine spectral structures of methane has been demonstrated. The DFG source can provide 10-μJ-level idler energy at 10 Hz repetition rate across the tuning range of 3308.5-3317.3 nm. An idler pulse energy stability of 5.3% rms for 500 consecutive pulses was obtained as a proof of the reliable absorption measurement after averaging. At a reduced pressure of 50 mbar, fine spectral lines in the Q-branch of methane v_3-band were resolved under an estimated linewith of ~0.007 $cm^{-1}$and further compared to the HITRAN simulation.

In the future, the work presented in this thesis can be further developed towards the following directions:

- The performance optical parametric sources, especially OPOs based on OP-GaP, is still to be further improved and optimized. For 1-μm nanosecond pump lasers, OP-GaP crystals have been tested and shown to have strong absorption, so reducing the crystal length to an optimum level where we can balance the parametric gain and absorption loss would be beneficial for output power scaling and alleviating crystal thermal effects. The idler wavelengths of OP-GaP parametric sources can also be extended into deeper mid-IR region with longer grating periods. In femtosecond regime, where only 1-mm or 2-mm crystal lengths are typically required, the crystal absorption for the pump laser at ~1 μm will be almost negligible, thus femtosecond OP-GaP parametric sources will be promising to achieve good performance in the deeper mid-IR compared to the conventional femtosecond MgO:PPLN sources up to ~4 μm. Moreover, the degenerate MgO:PPLN OPO at 2.1 μm demonstrated in chapter 5 also makes it possible to develop 2-μm-pumped, deep mid-IR OP-GaP parametric sources. The

OP-GaP crystals in this case can provide much broader spectral acceptance bandwidth for the pump laser, and the pump wavelength is also shifted away from the short-wavelength transparency edge of OP-GaP, which can significantly reduce absorption loss and thus improve the down-conversion efficiency and output performance.

- With respect to the single-frequency pulsed DFG source demonstrated in chapter 6 and its application for high-resolution molecular spectroscopy, future work can be focused on output energy scaling using a parametric amplification stage. With achievable amplified energy at hundreds-of-μJ level in the mid-IR, it would be feasible to realize nonlinear spectroscopy based on degenerate four-wave mixing or polarization spectroscopy in combustion environment, so that not only high spectral resolution, but also high spatial resolution can be achieved for improved understanding of chemical reactions. As a general concept demonstration, this type of sources can be further extended to other wavelength regions in the mid-IR by simply changing the seed laser wavelength, providing a versatile tool for studying various molecules.

Bibliography

[1] T. H. Maiman, "Stimulated optical emission in ruby," *Nature*, 187, 493-494 (1960).

[2] O. Svelto, "Principles of lasers," 5th ed., New York: Springer Science+Business Media (2010).

[3] P. A. Franken, A. E. Hill, C. W. Peters, and G. Weinreich, "Generation of optical harmonics," *Phys. Rev. Lett.*, 7, 118-119 (1961).

[4] M. Bass, P. A. Franken, A. E. Hill, C. W. Peters, and G. Weinreich, "Optical mixing," *Phys. Rev. Lett.*, 8, 18 (1962).

[5] J. A. Armstrong, N. Bloembergen, J. Ducuing, and P. S. Pershan, "Interaction between light waves in a nonlinear dielectric," *Phys. Rev.*, 127, 1918-1939 (1962).

[6] A. W. Smith, and N. Braslau, "Observation of an optical difference frequency," *J. Appl. Phys.*, 34, 2105-2106 (1963).

[7] R. H. Kingston, "Parametric amplification and oscillation at optical frequencies," *Proc. IRE*, 50, 472–473 (1962).

[8] N. M. Kroll, "Parametric amplification in spatially extended media and application to the design of tunable oscillators at optical frequencies," *Phys. Rev.*, 127, 1207–1211 (1962).

[9] J. A. Giordmaine, and R. C. Miller, "Tunable coherent parametric oscillation in $LiNbO_3$ at optical frequencies," *Phys. Rev. Lett.*, 14, 973-976 (1965).

[10] F.C. Zumsteg, J.D. Bierlein, and T.E. Gier, "$KxRb_1{-}xTiOPO_4$: a new nonlinear optical material," *J. Appl. Phys.*, 47, 4980-4985 (1976).

[11] J. Wang, J. Wei, Y. Liu, X. Yin, X. Hu, Z. Shao, and M. Jiang, "A survey of research on KTP and its analogue crystals," *Prog. Cryst. Growth Charact. Mater.*, 13, 3-15 (2000).

[12] C. Chen, B. Wu, A. Jiang, and G. You, "A new-type ultraviolet SHG crystal β-BaB_2O_4," *Sci. Sin. Ser. B*, 28, 235 (1985).

[13] C. Chen, A. Wu, A. Jiang, B. Wu, and G. You, "New nonlinear-optical crystal: LiB_3O_5," *J. Opt. Am. B*, 6, 616-621 (1989).

[14] S. Matsumoto, E. J. Lim, H. M. Hertz, and M. M. Fejer, "Quasi-phase-matched second harmonic generation of blue light in electrically periodically-poled lithium tantalate waveguides," *Electron. Lett.*, 27, 2040-2042 (1991).

[15] L. E. Myers, R. C. Eckardt, M. M. Fejer, R. L. Byer, W. R. Bosenberg, and J. W. Pierce, "Quasi-phase-matched optical parametric oscillators in bulk periodically poled $LiNbO_3$," *J. Opt. Soc. Am. B*, 12, 2102-2116 (1995).

[16] M. Yamada, N. Nada, M. Saitoh, and K. Watanabe, "First-order quasi-phase matched $LiNbO_3$ waveguide periodically poled by applying an external field for efficient blue second-harmonic generation," *Appl. Phys. Lett.*, 62, 435-436 (1993).

[17] G. Miller, "Periodically poled lithium niobate: modeling, fabrication, and nonlinear-optical performance," Stanford University: PhD thesis dissertation (1998).

[18] A. Godard, "Infrared (2-12 μm) solid-state laser sources: a review," *C. R. Phys.*, 8, 1100-1128 (2007).

[19] M. Ebrahim-Zadeh, S. C. Kumar, A. Esteban-Martin, and G. K. Samanta, "Breakthroughs in photonics 2012: Breakthroughs in optical parametric oscillators," *IEEE Photon. J.*, 5, 0700105 (2013).

[20] M. Vainio, and L. Halonen, "Mid-infrared optical parametric oscillators and frequency combs for molecular spectroscopy," *Phys. Chem. Chem. Phys.*, 18, 4266-4294 (2016).

[21] F. K. Tittel, R. F. Curl, L. Dong, J. H. Doty, A. A. Kosterev, R. Lewicki, D. Thomazy, and G. Wysocki, "Recent advances in infrared semiconductor laser based chemical sensing technologies," in *Terahertz and Mid Infrared Radiation* (Springer, 2011), 165-173.

[22] Z. W. Sun, M. Försth, Z. S. Li, B. Li, and M. Aldén, "Mid-infrared polarization spectroscopy: A tool for in situ measurements of toxic gases in smoke-laden environments," *Fire Mater.*, 35, 527-537 (2011).

[23] Z. W. Sun, Z. S. Li, B. Li, M. Aldén, P. Ewart, "Detection of C_2H_2 and HCl using mid-infrared degenerate four-wave mixing with stable beam alignment: towards practical in situ sensing of trace molecular species," *Appl. Phys. B*, 98, 593-600 (2010).

[24] M. S. Webb, P. F. Moulton, J. J. Kasinski, R. L. Burnham, G. Loiacono, and R. Stolzenberger, "High-average-power $KTiOAsO_4$ optical parametric oscillator," *Opt. Lett.*, 23, 1161-1163 (1998).

[25] Y. Peng, W. Wang, X Wei, and D. Li, "High-efficiency mid-infrared optical parametric oscillator based on PPMgO:CLN," *Opt. Lett.*, 34, 2897-2899 (2009).

[26] B. Wu, J. Kong, and Y. Shen, "High-efficiency semi-external-cavity-structured periodically poled MgLN-based optical parametric oscillator with output power exceeding 9.2 W at 3.82 μm," *Opt. Lett.*, 35, 1118-1120 (2010).

[27] D. Lin, S. Alam, Y. Shen, T. Chen, B. Wu, and D. J. Richardson, "Large aperture PPMgLN based high-power optical parametric oscillator at 3.8 μm

pumped by a nanosecond linearly polarized fiber MOPA," *Opt. Express*, 20, 15008-15014 (2012).

[28] P. A. Budni, L. A. Pomeranz, M. L. Lemons, P. G. Schunemann, T. M. Pollak, and E. P. Chicklis, "10W Mid-IR Holmium Pumped $ZnGeP_2$ OPO," in *Advanced Solid State Lasers* (Optical Society of America, 1998), paper FC1.

[29] E. Lippert, H. Fonnum, G. Arisholm, and K. Stenersen, "A 22-watt mid-infrared optical parametric oscillator with V-shaped 3-mirror ring resonator," *Opt. Express*, 18, 26475-26483 (2010).

[30] G. Zhu, Y. Ju, T. Wang, and Y. Wang, "A mid-IR 14.1 W $ZnGeP_2$ optical parametric oscillator pumped by a Tm,Ho:$GdVO_4$ laser," *Chin. Phys. Lett.*, 26, 034208 (2009).

[31] Y. Peng, X. Wei, X. Luo, Z. Nie, J. Peng, Y. Wang, and D. Shen, "High-power and widely tunable mid-infrared optical parametric amplification based on PPMgLN," *Opt. Lett.*, 41, 49-51 (2016).

[32] B.Yao, Y. Shen, X. Duan, T. Dai, Y. Ju, and Y. Wang, "A 41-W $ZnGeP_2$ optical parametric oscillator pumped by a Q-switched Ho:YAG laser," *Opt. Lett.*, 39, 6589-6592 (2014).

[33] J. T. Lin, and J. L. Montgomery, "Generation of tunable mid-IR (1.8–2.4 μm) laser from optical parametric oscillation in KTP," *Opt. Commun.*, 75, 315-320 (1990).

[34] M. Raybaut, T. Schmid, A. Godard, A. K. Mohamed, M. Lefebvre, F. Marnas, P. Flamant, A. Bohman, P. Geiser, and P. Kaspersen, "High-energy single-longitudinal mode nearly diffraction-limited optical parametric source with 3 MHz frequency stability for CO_2 DIAL," *Opt. Lett.*, 34, 2069-2071 (2009).

[35] G. Arisholm, Ø. Nordseth, and G. Rustad, "Optical parametric master oscillator and power amplifier for efficient conversion of high-energy pulses with high beam quality," *Opt. Express*, 12, 4189-4197 (2004).

[36] A. Dergachev, D. Armstrong, A. Smith, T. Drake, and M. Dubois, "3.4-μm ZGP RISTRA nanosecond optical parametric oscillator pumped by a 2.05-μm Ho:YLF MOPA system," *Opt. Express*, 15, 14404-14413 (2007).

[37] H. Ishizuki, and T. Taira, "High-energy quasi-phase-matched optical parametric oscillation in a periodically poled MgO:$LiNbO_3$ device with a 5 mm×5 mm aperture," *Opt. Lett.*, 30, 2918-2920 (2005).

[38] A. Zukauskas, N. Thilmann, V. Pasiskevicius, F. Laurell, and C. Canalias, "5 mm thick periodically poled Rb-doped KTP for high energy optical parametric frequency conversion," *Opt. Mater. Express*, 1, 201-206 (2011).

[39] Q. Liu, J. Liu, Z. Zhang, and M. Gong, "A high energy 3.75 μm KTA optical parametric oscillator at a critical angle," *Laser Phys. Lett.*, 10, 075407 (2013).

[40] R. Foltynowicz, "A 243mJ, Eye-Safe, Injection-Seeded, KTA Ring-Cavity Optical Parametric Oscillator," in *Nonlinear Optics: Materials, Fundamentals and Applications* (Optical Society of America, 2011), NME8.

[41] M. W. Haakestad, H. Fonnum, and E. Lippert, "Mid-infrared source with 0.2 J pulse energy based on nonlinear conversion of Q-switched pulses in $ZnGeP_2$," *Opt. Express*, 22, 8556-8564 (2014).

[42] M. W. Haakestad, G. Arisholm, E. Lippert, S. Nicolas, G. Rustad, and K. Stenersen, "High-pulse-energy mid-infrared laser source based on optical parametric amplification in $ZnGeP_2$," *Opt. Express*, 16, 14263-14273 (2008).

[43] K. L. Vodopyanov, and P. G. Schunemann, "Efficient difference-frequency generation of 7–20-μm radiation in $CdGeAs_2$," *Opt. Lett.*, 23, 1096-1098 (1998).

[44] C. Chen, Y. Hsu, J. Y. Huang, C. Chang, J. Zhang, and C. Pan, "Generation properties of coherent infrared radiation in the optical absorption region of GaSe crystal," *Opt. Express*, 14, 10636-10644 (2006).

[45] A. Dhirani, and P. Guyot-Sionnest, "Efficient generation of infrared picosecond pulses from 10 to 20 μm", *Opt. Lett.*, 20, 1104-1106 (1995).

[46] K. L. Vodopyanov, I. Makasyuk, and P. G. Schunemann, "Grating tunable 4 - 14 μm GaAs optical parametric oscillator pumped at 3 μm," *Opt. Express*, 22, 4131-4136 (2014).

[47] R. L. Sutherland, "Handbook of nonlinear optics," New York: Marcel Dekker (1996).

[48] R. W. Boyd, "Nonlinear optics," San Diego, USA: Academic Press (2007).

[49] M. Ebrahim-Zadeh, and M. H. Dunn, "Optical parametric oscillators," in Handbook of optics, New York, USA: McGraw-Hill (2000).

[50] D. A. Kleinman, "Nonlinear dielectric polarization in optical media," *Phys. Rev.*, 126, 1977-1979 (1962).

[51] R. W. Munn and C. N. Ironside, "Principles and applications of nonlinear optical materials," Glasgow, UK: Blackie Academic & Professional (1993).

[52] K. Devi, S. C. Kumar, and M. Ebrahim-Zadeh, "Fiber-laser-based, high-repetition-rate, picosecond ultraviolet source tunable across 329–348 nm," *Opt. Lett.*, 41, 4799-4802 (2016).

[53] K. Devi, S. C. Kumar, and M. Ebrahim-Zadeh, "Tunable, continuous-wave, ultraviolet source based on intracavity sum-frequency-generation in an

optical parametric oscillator using BiB_3O_6," *Opt. Express*, 21, 24829-24836 (2013).

[54] E. Mimoun, L. De Sarlo, J. Zondy, J. Dalibard, and F. Gerbier, "Sum-frequency generation of 589 nm light with near-unit efficiency," *Opt. Express*, 16, 18684-18691 (2008).

[55] T. Nishikawa, A. Ozawa, Y. Nishida, M. Asobe, F. Hong, and T. W. Hänsch, "Efficient 494 mW sum-frequency generation of sodium resonance radiation at 589 nm by using a periodically poled Zn:$LiNbO_3$ ridge waveguide," *Opt. Express*, 17, 17792-17800 (2009).

[56] M. T. Andersen, P. J. Schlosser, J. E. Hastie, P. Tidemand-Lichtenberg, M. D. Dawson, and C. Pedersen, "Singly-resonant sum frequency generation of visible light in a semiconductor disk laser," *Opt. Express*, 17, 6010-6017 (2009).

[57] S. Fan, F. Qi, T. Notake, K. Nawata, Y. Takida, T. Matsukawa, and H. Minamide, "Diffraction-limited real-time terahertz imaging by optical frequency up-conversion in a DAST crystal," *Opt. Express*, 23, 7611-7618 (2015).

[58] L. Meng, L. Høgstedt, P. Tidemand-Lichtenberg, C. Pedersen, and P. J. Rodrigo, "GHz-bandwidth upconversion detector using a unidirectional ring cavity to reduce multilongitudinal mode pump effects," *Opt. Express*, 25, 14783-14794 (2017).

[59] R. Demur, A. Grisard, L. Morvan, E. Lallier, N. Treps, and C. Fabre, "High sensitivity narrowband wavelength mid-infrared detection at room temperature," *Opt. Lett.*, 42, 2006-2009 (2017).

[60] A. Barh, C. Pedersen, and P. Tidemand-Lichtenberg, "Ultra-broadband mid-wave-IR upconversion detection," *Opt. Lett.*, 42, 1504-1507 (2017).

[61] A. Barh, P. Tidemand-Lichtenberg, and C. Pedersen, "Thermal noise in mid-infrared broadband upconversion detectors," *Opt. Express*, 26, 3249-3259 (2018).

[62] Q. Hu, J. S. Dam, C. Pedersen, and P. Tidemand-Lichtenberg, "High-resolution mid-IR spectrometer based on frequency upconversion," *Opt. Lett.*, 37, 5232-5234 (2012).

[63] G. K. Samanta, S. C. Kumar, K. Devi, and M. Ebrahim-Zadeh, "Multicrystal, continuous-wave, single-pass second-harmonic generation with 56% efficiency," *Opt. Lett.*, 35, 3513-3515 (2010).

[64] K. Devi, S. Parsa, and M. Ebrahim-Zadeh, "Continuous-wave, single-pass, single-frequency second-harmonic-generation at 266 nm based on birefringent-multicrystal scheme," *Opt. Express*, 24, 8763-8775 (2016).

[65] S. C. Kumar, G. K. Samanta, and M. Ebrahim-Zadeh, "High-power, single-frequency, continuous-wave second-harmonic-generation of ytterbium fiber laser in PPKTP and MgO:sPPLT," *Opt. Express*, 17, 13711-13726 (2009).

[66] D. A. Kleinman, "Theory of optical parametric noise," *Phys. Rev.*, 174, 1207 (1968).

[67] G. D. Boyd and D. A. Kleinman, "Parametric interaction of focused Gaussian light beams," *J. Appl. Phys.*, 39, 3597 (1968).

[68] J. T. Verdeyen, "Laser electronics," 2nd ed., New Jersey: Prentice-Hall (1989).

[69] G. K. Samanta, "High-power, continuous-wave optical parametric oscillators from visible to near-infrared," ICFO-The Institute of Photonic Sciences: PhD thesis dissertation (2009).

[70] S. C. Kumar, "High-power, fiber-laser-pumped optical parametric oscillators from the visible to mid-infrared," ICFO-The Institute of Photonic Sciences: PhD thesis dissertation (2011).

[71] P. G. Schunemann, K. T. Zawilski, L. A. Pomeranz, D. J. Creeden, and P. A. Budni, "Advances in nonlinear optical crystals for mid-infrared coherent sources," *J. Opt. Soc. Am. B*, 33, D36-D43 (2016).

[72] J. Wueppen, S. Nyga, B. Jungbluth, and D. Hoffmann, "1.95 μm-pumped OP-GaAs optical parametric oscillator with 10.6 μm idler wavelength," *Opt. Lett.*, 41, 4225-4228 (2016).

[73] K. Devi, P. G. Schunemann, and M. Ebrahim-Zadeh, "Continuous-wave, multimilliwatt, mid-infrared source tunable across 6.4–7.5 μm based on orientation-patterned GaAs," *Opt. Lett.*, 39, 6751-6754 (2014).

[74] Q. Clément, J.-M. Melkonian, J.-B. Dherbecourt, M. Raybaut, A. Grisard, E. Lallier, B. Gérard, B. Faure, G. Souhaité, and A. Godard, "Longwave infrared, single-frequency, tunable, pulsed optical parametric oscillator based on orientation-patterned GaAs for gas sensing," *Opt. Lett.*, 40, 2676-2679 (2015).

[75] R. K. Feaver, R. D. Peterson, and P. E. Powers, "Longwave-IR optical parametric oscillator in orientation-patterned GaAs pumped by a 2 μm Tm,Ho:YLF laser," *Opt. Express*, 21, 16104-16110 (2013).

[76] O. H. Heckl, B. J. Bjork, G. Winkler, P. B. Changala, B. Spaun, G. Porat, T. Q. Bui, K. F. Lee, J. Jiang, M. E. Fermann, P. G. Schunemann, and J. Ye, "Three-photon absorption in optical parametric oscillators based on OP-GaAs," *Opt. Lett.*, 41, 5405-5408 (2016).

[77] K. L. Vodopyanov, E. Sorokin, I. T. Sorokina, and P. G. Schunemann, "Mid-IR frequency comb source spanning 4.4–5.4 μm based on

subharmonic GaAs optical parametric oscillator," *Opt. Lett.*, 36, 2275-2277 (2011).

[78] A. C. Lin, M. M. Fejer, J. S. Harris, *J. Crystal Growth*, 363, 258-263 (2013).

[79] V. Tassev, M. Snure, R. Peterson, R. Bedford, D. Bliss, G. Bryant, M. Mann, W. Goodhue, S. Vangala, K. Termkoa, A. Lin, J. S. Harris, M. M. Fejer, C. Yapp, and S. Tetlak, "Epitaxial growth of quasi-phase matched GaP for nonlinear applications: Systematic process improvements," *J. Cryst. Growth*, 352, 72-77 (2012).

[80] "https://www.azom.com/article.aspx?ArticleID=8347," [Online].

[81] "https://www.baesystems.com/en/product/nonlinear-crystal-technologies," [Online].

[82] J. Wei, J. M. Murray, J. O. Barnes, D. M. Krein, P. G. Schunemann, and S. Guha, "Temperature dependent Sellmeier equation for the refractive index of GaP," *Opt. Mater. Express*, 8, 485-490 (2018).

[83] T. Tomberg, M. Vainio, T. Hieta, and L. Halonen, "Sub-parts-per-trillion level sensitivity in trace gas detection by cantilever-enhanced photo-acoustic spectroscopy," *Sci. Rep.*, 8, 1848 (2017).

[84] S. Junaid, J. Tomko, M. P. Semtsiv, J. Kischkat, W. Ted Masselink, C. Pedersen, and P. Tidemand-Lichtenberg, "Mid-infrared upconversion based hyperspectral imaging," *Opt. Express*, 26, 2203-2211 (2018).

[85] A. Sabella, J. A. Piper, and R. P. Mildren, "Diamond Raman laser with continuously tunable output from 3.38 to 3.80 μm," *Opt. Lett.*, 39, 4037-4040 (2014).

[86] S. C. Kumar and M. Ebrahim-Zadeh, "Fiber-laser-based green-pumped picosecond MgO:sPPLT optical parametric oscillator," *Opt. Lett.*, 38, 5349-5352 (2013).

[87] S. C. Kumar, J. Wei, J. Debray, V. Kemlin, B. Boulanger, H. Ishizuki, T. Taira, and M. Ebrahim-Zadeh, "High-power, widely tunable, room-temperature picosecond optical parametric oscillator based on cylindrical 5%MgO:PPLN," *Opt. Lett.*, 40, 3897-3900 (2014).

[88] S. C. Kumar, R. Das, G. K. Samanta, and M. Ebrahim-Zadeh, "Optimally-output-coupled, 17.5 W, fiber-laser-pumped continuous-wave optical parametric oscillator," *Appl. Phys. B*, 102, 31-35 (2011).

[89] S. C. Kumar, A. Esteban-Martin, T. Ideguchi, M. Yan, S. Holzner, T. W. Hänsch, N. Picqué, and M. Ebrahim-Zadeh, "Few-cycle, broadband, mid-infrared optical parametric oscillator pumped by a 20-fs Ti:sapphire laser," *Laser & Photon. Rev.*, 8, L86-L91 (2014).

[90] S. C. Kumar, P. G. Schunemann, K. T. Zawilski, and M. Ebrahim-Zadeh, "Advances in ultrafast optical parametric sources for the mid-infrared based on $CdSiP_2$," *J. Opt. Soc. Am. B*, 33, D44-D56 (2016).

[91] L. A. Pomeranz, P. G. Schunemann, D. J. Magarrell, J. C. McCarthy, K. T. Zawilski, and D. E. Zelmon, "1064-nm-pumped mid-infrared optical parametric oscillator based on orientation-patterned gallium phosphide (OP-GaP)," in *CLEO* (Optical Society of America, 2015), paper SW3O.4.

[92] P. G. Schunemann, L. A. Pomeranz, and D. J. Magarrell, "First OPO based on orientation-patterned gallium phosphide (OP-GaP)," in *CLEO* (Optical Society of America, 2015), paper SW3O.1.

[93] J. Wei, S. C. Kumar, H. Ye, K. Devi, P. G. Schunemann, and M. Ebrahim-Zadeh, "Nanosecond difference-frequency generation in orientation-patterned gallium phosphide," *Opt. Lett.*, 42, 2193-2196 (2017).

[94] S. Guha, J. O. Barnes, P. G. Schunemann, "Mid-wave infrared generation by difference frequency mixing of continuous wave lasers in

orientation-patterned Gallium Phosphide," *Opt. Mater. Express*, 5, 2911-2923 (2015).

[95] G. Insero, C. Clivati, D. D'Ambrosio, P. D. Natale, G. Santambrogio, P. G. Schunemann, J. J. Zondy, and S. Borri, "Difference frequency generation in the mid-infrared with orientation-patterned gallium phosphide crystals," *Opt. Lett.*, 41, 5114-5117 (2016).

[96] S. C. Kumar and M. Ebrahim-Zadeh, "High-power, continuous-wave, mid-infrared optical parametric oscillator based on MgO:sPPLT," *Opt. Lett.*, 36, 2578-2580 (2011).

[97] Ø. Farsund and G. Rustad, "High-pulse-energy, linear optical parametric oscillator with narrow and symmetrical far field," *Opt. Express*, 21, 20171-20178 (2013).

[98] S. C. Kumar, J. Krauth, A. Steinmann, K. T. Zawilski, P. G. Schunemann, H. Giessen, and M. Ebrahim-Zadeh, "High-power femtosecond mid-infrared optical parametric oscillator at 7 μm based on $CdSiP_2$," *Opt. Lett.*, 40, 1398-1401 (2015).

[99] T. Cheng, Y. Kanou, X. Xue, D. Deng, M. Matsumoto, T. Misumi, T. Suzuki, and Y. Ohishi, "Mid-infrared supercontinuum generation in a novel $AsSe_2$-As_2S_5 hybrid microstructured optical fiber," *Opt. Express*, 22, 23019-23025 (2014).

[100] I. Silander, T. Hausmaninger, W. Ma, F. J. M. Harren, and O. Axner, "Doppler-broadened mid-infrared noise-immune cavity-enhanced optical heterodyne molecular spectrometry based on an optical parametric oscillator for trace gas detection," *Opt. Lett.*, 40, 439-442 (2015).

[101] A. Aadhi, G. K. Samanta, S. C. Kumar, and M. Ebrahim-Zadeh, "Controlled switching of orbital angular momentum in an optical parametric oscillator," *Optica*, 4, 349-355 (2017).

[102] M. Ebrahim-Zadeh and S. C. Kumar, "Yb-fiber-laser-pumped ultrafast frequency conversion sources from the mid-infrared to the ultraviolet," *IEEE J. Sel. Topics Quantum Electron.*, 20, 7600519 (2014).

[103] M. Ebrahim-Zadeh and S. C. Kumar, "Yb-fiber-laser-pumped continuous-wave frequency conversion sources from the mid-infrared to the ultraviolet," *IEEE J. Sel. Topics Quantum Electron.*, 20, 0902823 (2014).

[104] L. Maidment, P. G. Schunemann, and D. T. Reid, "Molecular fingerprint-region spectroscopy from 5 to 12 μm using an orientation-patterned gallium phosphide optical parametric oscillator," *Opt. Lett.*, 41, 4261-4264 (2016).

[105] H. Ye, S. C. Kumar, J. Wei, P. G. Schunemann, and M. Ebrahim-Zadeh, "Optical parametric generation in orientation-patterned gallium phosphide," *Opt. Lett.*, 42, 3694-3697 (2017).

[106] J. Wei, S. Chaitanya Kumar, H. Ye, P. G. Schunemann, and M. Ebrahim-Zadeh, "Performance characterization of mid-infrared difference-frequency-generation in orientation-patterned gallium phosphide," *Opt. Mater. Express*, 8, 555-567 (2018).

[107] J. P. Cariou, B. Augere, and M. Valla, "Laser source requirements for coherent lidars based on fiber technology," *C. R. Phys.*, 7, 213-223 (2006).

[108] C. R. Wilson, L. A. Hardy, P. B. Irby, and N. M. Fried, "Collateral damage to the ureter and Nitinol stone baskets during thulium fiber laser lithotripsy," *Lasers Surg. Med.,* 47, 403-410 (2015).

[109] N. Huo, S. Gupta, and G. Konstantatos, "MoS_2–HgTe Quantum Dot Hybrid Photodetectors beyond 2 μm," *Adv. Mater.*, 29, 1606576 (2017).

[110] J. Saikawa, M. Fujii, H. Ishizuki, and T. Taira, "High-energy, narrow-bandwidth periodically poled Mg-doped $LiNbO_3$ optical parametric oscillator with a volume Bragg grating," *Opt. Lett.*, 32, 2996-2998 (2007).

[111] M. Henriksson, M. Tiihonen, V. Pasiskevicius, and F. Laurell, "Mid-infrared ZGP OPO pumped by near-degenerate narrowband type-I PPKTP parametric oscillator," *Appl. Phys. B*, 88, 37-41 (2007).

[112] S. C. Kumar, and M. Ebrahim-Zadeh, "Yb-fiber-based, high-average-power, high-repetition-rate, picosecond source at 2.1 μm," *Laser Photonics Rev.*, 10, 970–977 (2016).

[113] A. Sahlberg, D. Hot, J. Kiefer, M. Aldén, and Z. Li, "Mid-infrared laser-induced thermal grating spectroscopy in flames," *Proc. Combust. Inst.*, 36, 4515-4523 (2017).

[114] J. Vanderover, and M. A. Oehlschlaeger, "A mid-infrared scanned-wavelength laser absorption sensor for carbon monoxide and temperature measurements from 900 to 4000 K," *Appl. Phys. B*, 99, 353-362 (2010).

[115] S. Veerabuthiran, A. K. Razdan, M. K. Jindal, R. K. Sharma, and V. Sagar, "Development of 3.0–3.45 μm OPO laser based range resolved and hard-target differential absorption lidar for sensing of atmospheric methane," *Opt. Laser Technol.*, 73, 1-5 (2015).

[116] J. B. Barria, S. Roux, J. Dherbecourt, M. Raybaut, J. Melkonian, A. Godard, and M. Lefebvre, "Microsecond fiber laser pumped, single-frequency optical parametric oscillator for trace gas detection," *Opt. Lett.*, 38, 2165-2167 (2013).

[117] G. W. Baxter, P. Schlup, I. T. McKinnie, J. Hellström, and F. Laurell, "Single-mode near-infrared optical parametric oscillator amplifier based on periodically poled $KTiOPO_4$," *Appl. Opt.*, 40, 6659-6662 (2001).

[118] L. A. W. Gloster, I. T. McKinnie, Z. X. Jiang, T. A. King, J. M. Boon-Engering, W. E. van der Veer, and W. Hogervorst, "Narrow-band

β-BaB_2O_4 optical parametric oscillator in a grazing-incidence configuration," *J. Opt. Soc. Am. B*, 12, 2117-2121 (1995).

[119] P. Schlup, G. W. Baxter, and I. T. McKinnie, "Single-mode near- and mid-infrared periodically poled lithium niobate optical parametric oscillator, " *Opt. Commun.*, 176, 267-271 (2000).

[120] R. T. White, Y. He, B. J. Orr, M. Kono, and K. G. H. Baldwin, "Pulsed injection-seeded optical parametric oscillator with low frequency chirp for high-resolution spectroscopy," *Opt. Lett.*, 28, 1248-1250 (2003).

[121] R. T. White, Y. He, B. J. Orr, M. Kono, and K. G. H. Baldwin, "Control of frequency chirp in nanosecond-pulsed laser spectroscopy. 2. A long-pulse optical parametric oscillator for narrow optical bandwidth," *J. Opt. Soc. Am. B*, 21, 1586-1594 (2004).

[122] F. Huisken, A. Kulcke, and D. Voelkel, "New infrared injection seeded optical parametric oscillator with high energy and narrow bandwidth output," *Appl. Phys. Lett.*, 62, 805-807 (1993).

[123] J. H. Marquardt, R. W. Mackes, and D. D. Smith, "Single-mode, tunable output from a midwave-infrared-seeded optical parametric oscillator system," *Appl. Opt.*, 41, 1163-1168 (2002).

[124] A. Fix and R. Wallenstein, "Spectral properties of pulsed nanosecond optical parametric oscillators: experimental investigation and numerical analysis," *J. Opt. Soc. Am. B*, 13, 2484-2497 (1996).

[125] K. W. Aniolek, R. L. Schmitt, T. J. Kulp, B. A. Richman, S. E. Bisson, and P. E. Powers, "Microlaser-pumped periodically poled lithium niobate optical parametric generator–optical parametric amplifier," *Opt. Lett.*, 25, 557-559 (2000).

[126] T.A. Reichardt, R. P. Bambha, T. J. Kulp, and R. L. Schmitt, "Frequency-locked, injection-seeded, pulsed narrowband optical parametric generator," *Appl. Opt.*, 42, 3564-3569 (2003).

[127] A. V. Kir'yanov, S. M. Klimentov, P. E. Powers, I. V. Mel'nikov, and Y. N. Korkishko, "IR tunable narrow-band nanosecond converter with a microchip pump source and periodically-poled lithium niobate," *Laser Phys. Lett.*, 5, 281-285 (2008).

[128] U. Bäder, T. Mattern, T. Bauer, J. Bartschke, M. Rahm, A. Borsutzky, and R. Wallenstein, "Pulsed nanosecond optical parametric generator based on periodically poled lithium niobate," *Opt. Commun.*, 217, 375-380 (2003).

[129] L. Xu, H. Chan, S. Alam, D. J. Richardson, and D. P. Shepherd, "High-energy, near- and mid-IR picosecond pulses generated by a fiber-MOPA-pumped optical parametric generator and amplifier," *Opt. Express*, 23, 12613-12618 (2015).

[130] C. Fischer, and M. W. Sigrist, "Trace-gas sensing in the 3.3-μm region using a diode-based difference-frequency laser photoacoustic system," *Appl. Phys. B*, 75, 305-310 (2002).

[131] G. Aoust, A. Godard, M. Raybaut, J-B. Dherbecourt, G. Canat, and M. Lefebvre, "Pump duration optimization for optical parametric oscillators," *J. Opt. Soc. Am. B*, 31, 3113-3122 (2014).

[132] G. Aoust, A. Godard, M. Raybaut, O. Wang, J-M. Melkonian, and M. Lefebvre, "Optimal pump pulse shapes for optical parametric oscillators," *J. Opt. Soc. Am. B*, 33, 842-849 (2016).

[133] R. T. Murray, T. H. Runcorn, E. J. R. Kelleher, and J. R. Taylor, "Highly efficient mid-infrared difference-frequency generation using synchronously pulsed fiber lasers," *Opt. Lett*., 41, 2446-2449 (2016).